MAGNETOHYDRODYNAMIC INSTABILITIES IN A RAPIDLY ROTATING SYSTEM

by

DOUGLAS R. McLEAN

A thesis submitted to the Faculty of Science, University of Glasgow, for the degree of Doctor of Philosophy

Department of Mathematics,
University of Glasgow
September 1997

For my Mum and Dad.

Contents

Preface

This thesis is submitted to the University of Glasgow in accordance with the requiremnets for the degree of Doctor of Philosophy.

I would like to take this opportunity to express my most sincere gratitude to my supervisor, Professor David R. Fearn for his advice, encouragement and guidance throughout the period of my research. I would also like to thank Drs Kenneth A. Hutcheson and Rainer Hollerbach for many helpful discussions.

Thanks are also due to the Engineering and Physical Sciences Research Council who funded this work through a research studentship, award reference number 957007114.

Summary

Magnetohydrodynamics and its use in understanding the Earth's magnetic field has enjoyed much attention in the last fifty years. This has much to do with the recent explosion in computer technology which has allowed the formulation and numerical solution of model problems which are not immediately analytically tractable. In this thesis, we approach the hydromagnetic dynamo problem from a stability point of view. We do not concern ourselves with the generation of the main (or basic) field, but consider its stability to small perturbations. Any instabilities found are important since they give constraints on the unknown field and sustaining motions in the core.

After the introduction in Chapter 1, Chapter 2 formulates a linearised hydromagnetic stability problem as an eigenvalue problem. For a hydromagnetic system in the geometry of an infinite cylindrical annulus, we have revealed the presence of double eigenvalues at various locations in the parameter space. We show that tracking a particular eigenvalue around a closed path in parameter space need not necessarily return the original eigenvalue. This phenomena was first examined by Jones (1987), in the context of Poiseuille flow. In the hydromagnetic problem, we find that the most unstable mode (i.e. the mode we are most interested in) often behaves in this manner. We show that classifying magnetic instabilities as being either of the resistive or ideal class is not possible at geophysically relevant field strengths.

In a nonlinear eigenvalue analysis, Fearn, Lamb, McLean & Ogden (1997) demonstrated qualitative differences between the viscid and the inviscid (magnetostrophic) approaches indicating that finite viscosity models cannot yet reach a parameter regime characteristic of the Earth's core.

In Chapters 3 and 4 we present a nonlinear hydromagnetic stability analysis in a

bounded annular model of the Earth's core. We adopt the magnetostrophic approximation in the fluid main body but incorporate viscous effects from the boundary layers in the form of the geostrophic flow. The nonlinear problem is then solved numerically using a time-stepping method.

Chapter 3 corroborates and extends the work of Fearn *et al* (1997) and Chapter 4 considers the stability and nonlinear development of more geophysically relevant basic fields that depend not only on the radial coordinate, but also on the axial coordinate. This work is then compared with the viscous analyses of Hutcheson & Fearn (1995a,b, 1996, 1997).

Chapter 1

Introduction

Recently, there has been considerable interest in the subject of magnetohydrodynamics as it applies to the Earth's core. The first scientific treatise on the subject was by W. Gilbert in the monograph "De Magnete" in 1600. Gilbert performed a series of experiments measuring the direction of the field on the surface of a spherical magnet. Upon comparing the results with observations on the Earth, Gilbert concluded that the Earth behaved like a giant magnet. It was not until the beginning of this century that remanent magnetism was challenged as a possible explanation for the geomagnetic field. The Curie temperature, beyond which permanent magnetism vanishes, is reached at a depth of 30km below the Earth's surface. Also, paleomagnetic records in ancient lava flows and in sediment layed down on the sea floor indicate the existence of a geomagnetic field which has maintained its strength over a very large number of diffusion timescales. A diffusion timescale

$$\tau_\eta = \mathcal{L}^2/\eta, \tag{1.1}$$

is a typical length of time a magnetic field may exist given no mechanism for field regeneration. Here we use the core radius $\mathcal{L}$ as a lengthscale ($\mathcal{L} = 3.486 \times 10^6 \mathrm{m}$) and take $\eta = 1/\mu\sigma = 1\mathrm{m}^2\mathrm{s}^{-1}$ [corresponding to $\mu = 4\pi \times 10^{-7}\mathrm{Hm}^{-1}$ and $\sigma = 8 \times 10^5 \mathrm{Sm}^{-1}$ (Secco & Schloessin, 1989) where μ is the permeability of free space and σ is the electrical conductivity]. This gives $\tau_\eta = 3.9 \times 10^5$ years. Thus, the existence of the geomagnetic field cannot be explained by permanent magnetism nor by an ancient fossil field.

Seismic measurements of the Earth's interior show the existence of a solid iron

inner core extending to a radius of 1221 km, a liquid outer core comprised of iron and some lighter admixture extending to 3480 km all encased in a rocky mantle and thin crust at 6371 km. Larmor (1919) conjectured that the observed geomagnetic field could be produced by the motion of a homogeneous electrically conducting fluid. To this day it is believed that the flow of molten iron in the Earth's outer core and the associated feedback of the magnetic field on the flow constitutes the geodynamo; a nonlinear mechanism that converts mechanical energy into magnetic energy.

The geodynamo must be fuelled by an energy source (or sources) if the magnetic and flow fields are to overcome losses incurred through ohmic and viscous diffusion. Many energy sources have been postulated. For example, internal heating in the core due to the decay of radioactive isotopes may provide enough energy to maintain dynamo action. Alternatively, a geodynamo driven by convective motions associated with the freezing of a solid inner core and the subsequent release of latent heat has been proposed by Verhoogen (1961). Braginsky (1963) later introduced the idea of buoyant material liberated at the inner-core-boundary (ICB) giving rise to compositional convection. Another source may result from the gravitational influence of the Sun and Moon on the Earth. This results in the precession of the Earth's rotation axis. Kerswell (1994, 1996) has shown that precessional energy may provide enough energy to maintain dynamo action. In short, there are many viable energy sources for the geodynamo and the precise details of which sources are dominant is far from certain. Detailed discussions are given by Lister & Buffett (1995) and Fearn (1997).

Recently, considerable effort has been expended in trying to understand the geodynamo and the fluid motions that perpetuate it, see for example, Soward (1991), Roberts & Soward (1992). Various assaults on modelling the full nonlinear geodynamo problem are underway. Depending on the complexity of the model, this typically involves solving a nonlinear system of coupled partial differential equations in a frame co-rotating with the Earth's mantle, $\boldsymbol{\Omega}_0 = \Omega_0 \mathbf{1}_z$. Here we use $(\mathbf{1}_s, \mathbf{1}_\phi, \mathbf{1}_z)$ to represent the cylindrical polar base vectors and $(\mathbf{1}_r, \mathbf{1}_\theta, \mathbf{1}_\phi)$ to represent the spherical polar base vectors. Suppose time is nondimensionalised on the magnetic diffusion timescale τ_η defined in (1.1), length on the core radius $\mathcal{L}$, speed on $\mathcal{L}/\tau_\eta$, the magnetic field on $(2\Omega_0\mu\rho_0\eta)^{1/2}$ and the temperature on $\beta\mathcal{L}$ (where β is the maximum of the temperature gradient). Then a typical set of governing

equations includes the momentum equation

$$Ro\left(\frac{\partial \mathbf{V}}{\partial t}+\mathbf{V}\cdot\nabla\mathbf{V}\right)+1_z\times\mathbf{V}= \\ -\nabla\Pi-q\,Ra\,T\,\mathrm{g}+E\nabla^2\mathbf{V}+(\nabla\times\mathbf{B})\times\mathbf{B}\,, \tag{1.2}$$

where we have adopted the simple linear relationship between density ρ and temperature T, $\rho=\rho_0[1-\alpha(T-T_0)]$. Here, α is the volume coefficient of thermal expansion and T_0 is a reference temperature at which $\rho=\rho_0$. A further simplification has been made by using the Boussinesq approximation where the density is seen to vary only where it multiplies the thermal buoyancy term. The magnetic induction equation governs the evolution of the magnetic field $\mathbf{B}$,

$$\frac{\partial \mathbf{B}}{\partial t}=\nabla\times(\mathbf{V}\times\mathbf{B})+\nabla^2\mathbf{B}\,, \tag{1.3}$$

and the thermal equation governs the temperature T,

$$\frac{\partial T}{\partial t}+\mathbf{V}\cdot\nabla T=q\nabla^2T+\epsilon\,. \tag{1.4}$$

where ϵ is a heat source term. Finally, many models simplify the mass continuity equation by assuming that the core fluid is incompressible. This leads to

$$\nabla\cdot\mathbf{V}=0\,. \tag{1.5}$$

The above system is then closed on application of appropriate boundary conditions on the field $\mathbf{B}$ and flow $\mathbf{V}$ at the core-mantle-boundary (CMB) and at the ICB [although it is now common for models to solve for the magnetic field in the inner core, see for example Hollerbach & Jones (1993a,b,1995)]. Examples of boundary conditions for the magnetic field might be that $\mathbf{B}$ must match to an external potential field. For the flow, the correct boundary conditions to apply are the no-fluid-slip conditions where $\mathbf{V}\equiv\mathbf{0}$ although some authors have used stress free boundary conditions for numerical convenience. Here the tangential stress along with the normal component of the flow must vanish on the CMB and at the ICB [see, for example, Kuang & Bloxham (1997), submitted].

In (1.2), (1.4) the following dimensionless numbers appear: the Rossby number

$$Ro=\frac{\eta}{2\Omega_0\mathcal{L}^2}, \tag{1.6}$$

the Roberts number

$$q = \frac{\kappa}{\eta}, \tag{1.7}$$

the modified Rayleigh number

$$Ra = \frac{g_0 \alpha \beta \mathcal{L}^2}{2\Omega_0 \kappa}, \tag{1.8}$$

and the Ekman number

$$E = \frac{\nu}{2\Omega_0 \mathcal{L}^2}. \tag{1.9}$$

The gravitational term $\mathbf{g}$ from (1.2) has been written as $-g_0 r \mathbf{1}_r$. The Rayleigh number Ra, prescribed in dynamo calculations, is used to control the strength of the thermal forcing when the dynamo energy source is due to thermal buoyancy. If compositional buoyancy were to be modelled, then another time-evolution equation, identical to (1.4), for the mass fraction C of the light constituent would be needed. An analogous "compositional Rayleigh number" would then multiply the additional term due to compositional buoyancy in (1.2).

The Rossby number, Ro, is the ratio of the magnetic diffusion timescale to the inertial timescale (Ω_0^{-1}). Consequently, it is very small and is of $O(10^{-8})$. On these grounds, the inertial term $[Ro\, D\mathbf{V}/Dt]$ is usually neglected in calculations. The Roberts number, q, measures the ratio of thermal to magnetic diffusivities. It is believed that $q = O(10^{-5})$. Dynamo calculations have not yet approached such small values and q has usually been taken between 0.1 and 10. The Ekman number is the nondimensional measure of viscosity in the core and is very small. Its value may lie between 10^{-15}, if molecular diffusivities are used, and 10^{-8}, if turbulent values are used. The computational problems associated with trying to resolve the consequent narrow viscous boundary layers leads us to consider the case where $E \equiv 0$. This, along with setting Ro identically equal to zero, is called the magnetostrophic approximation.

By the numerically intensive nature of dynamo calculations, today's parallel computers are stretched to their absolute limit. Glatzmaier & Roberts (1995a,b,1996a,b) have been particularly successful in integrating the governing equations in their geodynamo model through a number magnetic diffusion timescales and have obtained a field reversal. In their time evolution calculations they observed that the inner core was rotating, on average, 3° per year faster than the mantle. Together with the

recently established anisotrophy of the inner core, Song & Richards (1996), and later Su & Dziewonski (1996), examined seismic records extending over the last 28 years. Song & Richards were able to infer that the inner core is rotating at a rate of 1.1° per year faster than the mantle. This finding was corroborated by Su & Dziewonski who found the slightly faster rate of 3° per year. This has certain implications for core dynamics as suggested by Whaler & Holme (1996). If changes in core angular momentum have zero average over long periods of time, then the observed secular variation or westward drift of the magnetic field at the CMB [consistent with westward travelling fluid beneath the mantle] could be explained by eastward travelling flow at the ICB.

The main problem experienced by Glatzmaier & Roberts (1995a,b,1996a,b) and, indeed, by anyone writing and running computer models of the geodynamo is that the geophysically relevant parameter regime is computationally difficult to reach. Even the most modest of calculations will take several months to complete a very few diffusion timescales so it is obvious that we have little opportunity to explore the parameter space. Most physical insight into such problems is usually obtained by a thorough examination of the parameter space and if this is not practical, then the results from full dynamo calculations need to be complemented by simpler model problems that are much less numerically intensive and focus on one aspect of the physics.

There are several paths that one may take to simplify the problem in order to make it manageable yet retaining essential physics. The evolution of magnetic instability is one such path. The Elsasser number

$$\Lambda = B_M^2/2\Omega_0\mu\rho_0\eta \tag{1.10}$$

is a nondimensional measure of the magnetic field strength B_M (where B_M is the maximum amplitude of the magnetic field $\mathbf{B}$) and an inverse measure of the magnetic diffusivity η. In a cylindrical geometry, Fearn (1983b,1984,1985 and 1988) examined the linear stability of various s-dependent basic state magnetic fields. This, together with later work in a spherical geometry and in spherical shells (Zhang & Fearn, 1994, 1995) has shown that the field strength at the onset of instability corresponds to $\Lambda = O(1)$. This value is not inconsistent with a dynamo of the strong field type. Although the observed field at the Earth's surface is weak, strong field theory

predicts the field is comprised of a strong toroidal component [$\Lambda = O(1)$], vanishing at the CMB, and by a weaker poloidal part [$\Lambda < O(1)$] which can be measured at the Earth's surface. Thus, magnetic instabilities play an important role in constraining (by extracting energy from) the mean magnetic field.

Magnetic instabilities in a rapidly rotating system, such as the Earth's outer core, generally fall into one of two categories: the ideal or 'field gradient' instability and the resistive instability. Early analytical work, in the absence of diffusion, by Acheson (1972) [see also Acheson (1973),(1983)], led to the discovery of ideal instabilities that result from gradients in the magnetic field. Later numerical work, in particular by Fearn (1983b), not only confirmed the existence of such an instability but also uncovered a class of instability, hitherto unseen in a rapidly rotating system, dependent on diffusion for its very existence. The term 'resistive instability', as used in non-rotating systems, was used for this class.

In the perfectly conducting limit, magnetic field lines become 'frozen' into the fluid. Here, in the absence of diffusion, under favourable conditions, ideal instabilities may form. Such an instability cannot, therefore, violate the frozen flux criterion and so is constrained by it. Acheson (1983) has found that a curved magnetic field is required for the ideal instability and furthermore, that the magnetic field strength should increase sufficiently quickly with the radial coordinate s – hence the term 'field gradient instability'.

Any instability requires the movement of field lines and if those lines are constrained to be frozen into the fluid then any such movement must be accompanied by a fluid motion. However, the introduction of magnetic diffusion, η, allows for the movement of field lines relative to the fluid and the reconnection of field lines. This gives the system a greater freedom and so facilitates extraction of energy from the basic field. The resistive instability requires the presence of diffusion before it can draw any energy.

A criterion that is often used to distinguish between the two types of instability is the trend exhibited by an instability's growth rate and frequency as the Elsasser number $\Lambda \to \infty$. In the case of the ideal instability, the growth rate is directly related to the magnitude of the magnetic field. When Λ is high, diffusive effects are negligible and much energy contained in the field is available for the instability. Therefore,

in the perfectly conducting limit, $\Lambda \to \infty$, both growth rate p and magnitude of frequency $|s|$ tend to constant, positive, nonzero, values. For $\Lambda < \infty$ diffusion is introduced into the system and consequently, some of the energy that was available to the instability is now diffused away. Also, low values of Λ correspond to weak fields and little energy is available to instabilities. As Λ is reduced from ∞, the growth rate of will fall until eventually the instability becomes marginally stable ($p = 0$), at some critical value Λ_c of Λ. For $\Lambda < \Lambda_c$ the mode is stable ($p < 0$). An example of this behaviour is shown in Figure 2.3(a).

Diffusion is the catalyst by which the resistive instability extracts energy from the magnetic field. Since Λ is an inverse measure of the diffusivity, then at high values of Λ there is little diffusion present in the system and it is difficult for the resistive instability to extract energy from the field. Consequently, the growth rate and frequency of such an instability is very small and approachs zero as $\Lambda \to \infty$. As Λ decreases, diffusive effects become more and more pronounced and any resistive mode may extract more and more energy and its growth rate increases. Eventually, as Λ decreases further, diffusion will begin to inhibit the growth of the resistive instability until an optimum growth rate is achieved. As $\Lambda \to 0$, diffusive effects become stronger and energy that may have been previously available (at higher Λ) is now diffused away. When diffusion is strong enough, corresponding to $\Lambda = \Lambda_c$, any instabilities become marginally stable and for $\Lambda < \Lambda_c$ the system is stable. An example of this behaviour can be found in Figure 2.3(b).

In Chapter 2 we consider classifying magnetic instabilities as either being of the resistive or of the ideal class. Formulating a linear stability analysis of an s-dependent basic state field, typical of those investigated by Fearn (e.g. 1988), as an eigenvalue problem for the complex growth rate, we show that it is not possible to distinguish between the two instability classes when $\Lambda = O(1)$. This work has appeared in publication by McLean & Fearn (1996).

Much work has been done in understanding magnetic instabilities in the linear regime. However, less nonlinear work has been done and, consequently, it is poorly understood. The main problem lies with the (almost) negligible viscosity of the outer core.

Taylor (1963) found that a peculiarity arising from the purely inviscid case is that

the magnetic torque must vanish over all cylinders $C(s)$ coaxial with the rotation axis. Making the magnetostrophic approximation [i.e. both viscous and inertial terms are neglected from the momentum equation (1.2)] gives

$$\mathbf{1}_z \times \mathbf{V} = -\nabla\Pi + (\nabla \times \mathbf{B}) \times \mathbf{B}. \tag{1.11}$$

Taking the ϕ-component of (1.11) and integrating over any cylinder $C(s)$ coaxial with the rotation axis, we obtain

$$\begin{aligned} \int_{C(s)} V_s \, \mathrm{d}S &= -\frac{1}{s}\int_{C(s)} \frac{\partial \Pi}{\partial \phi}\, \mathrm{d}S + \int_{C(s)} [(\nabla \times \mathbf{B}) \times \mathbf{B})]_\phi \, \mathrm{d}S \\ &= \int_{C(s)} [(\nabla \times \mathbf{B}) \times \mathbf{B})]_\phi \, \mathrm{d}S. \end{aligned} \tag{1.12}$$

The term on the left side of (1.12) measures the total volume of fluid passing across the cylindrical surface $C(s)$. Since the fluid is inviscid, then by mass conservation this quantity must vanish. Thus we have

$$\int_{C(s)} [(\nabla \times \mathbf{B}) \times \mathbf{B}]_\phi \, \mathrm{d}S = 0. \tag{1.13}$$

which is known as Taylor's constraint.

In addition to Taylor's constraint, under the magnetostrophic approximation, there is an undetermined component of the flow. If we take the curl of the momentum equation, $\nabla \times$ (1.2), then

$$\frac{\partial \mathbf{V}}{\partial z} = -\nabla \times [(\nabla \times \mathbf{B}) \times \mathbf{B}]. \tag{1.14}$$

Integration of (1.14) leaves an undetermined z-independent component of the flow $\mathbf{V}_0(s, \phi)$. In the spherical geometry, the no-normal-flow conditions will determine the s- and z-components of $\mathbf{V}_0$. For non-axisymmetric systems, the divergence free condition (1.5) determines the ϕ-component. However, the axisymmetric, azimuthal ϕ-component of $\mathbf{V}_0$ remains undetermined and is called the geostrophic flow V_G [see, for example, Fearn (1997) or Hollerbach (1996) and the references contained therein]. The undetermined component of the flow V_G is purely azimuthal and may only vary between the geostrophic contours $C(s)$ which are concentric circles centred on the axis of rotation.

A completely inviscid approximation of the fluid in the core is, however, a poor approximation. Although viscosity is small, it will become important in the narrow

Ekman layers adjacent to the boundaries. Instead of a completely inviscid fluid, we consider a fluid of very low viscosity where viscous effects are negligible except in the boundary layers. Setting $0 < E \ll 1$ and solving analytically for the boundary layer flow we then obtain a condition which is more general than (1.13). The viscous drag in the boundary layers can balance the magnetic torque. This viscous drag can be related to the mean azimuthal flow (or geostrophic flow) in the fluid main body via a boundary layer analysis (see, for example Fearn, 1994). The nature of the resulting modified Taylor's expression is different than (1.13). The latter is a constraint on the system and is satisfied by choosing the appropriate V_G which will "stretch out" meridional field lines in precisely the right manner so that Taylor's constraint is satisfied. The expression for the geostrophic flow in the spherical geometry is

$$V_G(s,t) = \frac{(2E)^{-1/2}}{2\pi s(1-s^2)^{1/2}} \int_{C(s)} [(\nabla \times \mathbf{B}) \times \mathbf{B}]_\phi \, \mathrm{d}S \,. \tag{1.15}$$

Let us consider the cylindrical geometry under the magnetostrophic approximation. There, Taylor's constraint (1.13) still holds and taking the curl of the momentum equations (1.11) once again leads to (1.14). However, using the method of applying the no-normal-flow and divergence free conditions to find $\mathbf{V}_0(s,\phi)$ up to a mean, undetermined, azimuthal flow fails. The parallel bounding plates together with (1.14) show that $\mathbf{V}_0$ may depend on ϕ as well as s. Hence the geostrophic contours need not necessarily be concentric circles and in general, $\mathbf{V}_0$ will have a component in the radial direction which will necessarily have a non-axisymmetric dependence (so that incompressibility is not violated). This is seen from the two no-normal-flow conditions on the parallel bounding plates. These conditions are no longer linearly independent, both showing that the z-component of $\mathbf{V}_0$ must vanish. This gives the following form for the geostrophic flow

$$V_G^s(s,\phi,t)\mathbf{1}_s + [V_G^\phi(s,\phi,t) + \bar{V}_G^\phi(s,t)]\mathbf{1}_\phi \tag{1.16}$$

where V_G^ϕ is the non-axisymmetric ϕ-component of the geostrophic flow and $\bar{V}_G^\phi$ is the corresponding axisymmetric component. This axisymmetric ϕ-component, $\bar{V}_G^\phi(s,t)\mathbf{1}_\phi$, can be derived in the same way as in the spherical case but modified for the cylindrical geometry. Thus, if we restore viscosity into narrow Ekman layers next to the parallel bounding plates then

$$\bar{V}_G^\phi(s,t) = \frac{(2E)^{-1/2}}{2\pi s} \int_{C(s)} [(\nabla \times \mathbf{B}) \times \mathbf{B}]_\phi \, \mathrm{d}S \,, \tag{1.17}$$

where $C(s)$ represents any coaxial cylinder.

Determination of $V_G^s \mathbf{1}_s + V_G^\phi \mathbf{1}_\phi$ is not done in this thesis. The reason for its exception is two-fold. Firstly, we examine the cylindrical geometry in the hope that it will give us some insight into the stability of the geodynamo. The true geophysical geometry is the spherical shell geometry and geostrophic flows of the form $V_G^s(s,\phi,t)\mathbf{1}_s + V_G^\phi(s,\phi,t)\mathbf{1}_\phi$ are not permitted there. As noted above, the geostrophic flow is necessarily one dimensional and purely azimuthal in the spherical case. Thus, in Chapters 3 and 4 we neglect the non-axisymmetric component of the geostrophic flow and enforce $\bar{V}_G^\phi$ only through (1.17).

The second reason for neglecting the non-axisymmetric geostrophic flow is mathematical. A main reason for considering the (simpler) cylindrical annular geometry over the more realistic spherical shell geometry is that the former geometry is less numerically intensive. However, if we were to include the term $V_G^s \mathbf{1}_s$ then the problem would necessarily become three dimensional (the non-axisymmetric components of V_G coupling with other axisymmetric and non-axisymmetric components). In this event, no advantage is to be gained in using the cylindrical geometry and one would be better employed solving the corresponding two dimensional problem in a spherical geometry.

Let us now consider the impact of V_G on an initially infinitesimal solution to the linearised problem as it grows in the nonlinear regime. As the solution grows and approaches an amplitude $|\mathbf{B}|$, $|\mathbf{V}| = \mathrm{O}(E^{1/4})$ the amplitude of the geostrophic flow approaches O(1). However, all other nonlinear effects are quadratic in the variables $\mathbf{B}$ and $\mathbf{V}$, so are $\mathrm{O}(E^{1/2})$. At this finite amplitude, V_G is the dominant nonlinear effect. When the magnetic field becomes equilibrated at these amplitudes we say that the system has evolved to an Ekman state.

Under the magnetostrophic approximation ($E, Ro \equiv 0$) a Taylor state is an inviscid state satisfying (1.13). Fearn & Proctor (1987) had some success in approaching Taylor states using an optimization technique. In their hydromagnetic problem, the poloidal part of the magnetic field, supported by an imposed emf, sustained the zonal field through a differential rotation. This differential rotation was imposed except for the geostrophic flow and a minimization technique was then employed on Taylor's integral [left side of (1.13)] to determine V_G. For certain choices of initial

fields, states approaching Taylor's condition were found. This, along with examples from other model problems, provided some of the first numerical evidence that Taylor states were possible.

One should realise, however, that directly obtaining Taylor states in a time stepping code is complicated by the fact that one must step in such a fashion as to select structures appropriate to (1.13). Retaining viscosity in Ekman boundary layers allows a modified version of Taylor's condition to be satisfied via an explicit determination of the geostrophic flow. Taylor states can then be characterised by flow and field strengths which are O(1) and where the geostrophic flow, as determined via (1.15), is also O(1). This is achieved by large internal cancellation in the Taylor integral [left side of (1.13)]. This property of internal cancellation leads to numerical difficulties in computing V_G as a Taylor's state is approached.

Malkus & Proctor (1975) proposed a trend for the equilibrated amplitude of magnetic field in a mean field dynamo. In our magnetic stability analysis, the Elsasser number Λ is the appropriate measure of imposed (maximum) field amplitude, B_M. The Malkus & Proctor (1975) scenario describes neatly the evolution of the magnetic field from infinitesimal amplitudes at critical onset ($\Lambda = \Lambda_c$) through to Ekman states [$|\mathbf{B}| = \mathrm{O}(E^{1/4})$] and on to Taylor states [where $|\mathbf{B}| = \mathrm{O}(1)$]. Shortly after linear onset, there is a clearly marked plateau where the solution is viscously limited in the vicinity of $|\mathbf{B}| = \mathrm{O}(E^{1/4})$ before the curve rises steeply to level off, finally, at O(1). For Λ just in excess of Λ_c the geostrophic flow varies quadratically with $|\mathbf{B}|$. However, as Λ increases further, V_G does not increase accordingly. This is an early indication of the progression toward a Taylor state where internal cancellation in the Taylor integral has begun to occur so that eventually Taylor's condition is satisfied.

Zhang (1995) has shown in a magnetoconvection problem that given an unstable basic field along with an unstable temperature gradient, thermal instabilities evolve into purely magnetically driven instabilities as the Rayleigh number Ra (1.8) is decreased and the Elsasser number Λ (1.10) is increased. In short, thermal and magnetic instabilities are both part of the same instability mechanism. Consequently, a hydromagnetic system may then be examined in the absence of buoyancy forces to concentrate on purely magnetic instabilities. If the only nonlinear effect is the

geostrophic flow V_G, it is possible to scale the dependent variables with $E^{1/4}$ in order to remove the explicit appearance of the Ekman number from the governing equations. Axisymmetric basic state fields depending on both the s and z coordinates are geophysically realistic. By including an axial dependence, one may incorporate basic field configurations which contain symmetry or antisymmetry about the equator. Also, any z-dependent basic field can be shown to drive a magnetic wind $\mathbf{V}_M$ (see Chapter 4). If a basic field is chosen which is independent of z, then $\mathbf{V}_M \equiv 0$ and this is certainly unrealistic in view of the results from the dynamo models of Glatzmaier & Roberts (1995a,b) or Kuang & Bloxham (1997).

Fearn, Lamb, McLean & Ogden (1997) [hereafter referred to as FLMO] used an imposed differential rotation in firstly a linear study and then a nonlinear eigenvalue analysis to investigate the possibility of subcriticality induced by the geostrophic flow. In the linear study, it was found that an imposed differential rotation $V(s)$ could lower Λ_c depending on the choice of $V(s)$. The results from their nonlinear eigenvalue analysis showed that the geostrophic flow can destabilise the system. Hutcheson & Fearn (1995a,b; 1996, 1997) looked at the full nonlinear stability problem with viscous effects included. They took $E = \mathrm{O}(10^{-4})$ and made an exhaustive search which revealed no subcritical instabilities. FLMO have therefore concluded that there must be some critical Ekman number below which the geostrophic flow dominates and subcriticality is possible. This important qualitative difference between finite E (taken as small as computational resources will permit but still very much larger than geophysical values) and magnetostrophic calculations emphasizes the continued importance of pursuing the latter despite the difficulties associated with Taylor's constraint.

In Chapters 3 and 4 we consider the stability of purely s-dependent and then s- and z-dependent basic fields to small, but finite perturbations in a time stepping calculation under the magnetostrophic approximation. The nonlinear effect of the geostrophic flow is considered in each chapter and its ability to induce subcriticality is assessed. The work in Chapter 3 complements and extends the nonlinear eigenvalue analysis of FLMO whilst the results of Chapter 4 may be compared with the similar, but viscous analyses of Hutcheson & Fearn (1996, 1997). It should be stressed that the introduction of an axial dependence into the basic fields considered

in Chapter 4 required an extensive modification to the numerical code of Chapter 3. This was necessary to model the coupling of the axial modes introduced through the non-autonomous presence of z in the governing equations.

Chapter 2

Classification of Magnetic Instabilities

2.1 Introduction

In many astrophysical applications we find ourselves in the regime of an almost perfectly conducting fluid. Here, field strengths are high, or the conductivity is so great [$\Lambda \gg O(1)$] that the distinctions between ideal and resistive modes of instability are clear. However, in a geophysical situation Λ is thought to be of $O(1)$. Can we still make a distinction between ideal and resistive instabilities at such low field strengths? In this chapter we investigate this question and show that the nearby presence of double eigenvalues has a profound influence on any such distinction.

The linear stability problem can be formulated as an eigenvalue problem for the complex growth rate $p + is$. This typically depends on several non-dimensional parameters. In the case we examine, these are the Elsasser number Λ and the axial wavenumber n. Jones (1987) has completed an investigation into double eigenvalue points arising from the stability analysis of plane parallel flow (Poiseuille flow). In his paper, Jones locates many double eigenvalue points and discusses the implications of their existence on mode classification. He also showed that the existence of nearby multiple eigenvalue points can have an effect on the path to instability of some 'promising' modes. Jones writes, "The neighbourhood of a double eigenvalue point is ... a place where sharp changes of direction are likely to occur in the eigenvalue paths."

Although we have homed in on the precise location of some double eigenvalues we have been more concerned with the behaviour of unstable modes as Λ and n are varied. By examining the trends exhibited by a mode's growth rate and frequency as $\Lambda \to \infty$ we investigate whether or not magnetic instabilities can be categorized as being of resistive or of the ideal type when $\Lambda \sim \mathrm{O}(1)$. We will also show that it is often the case that marginally stable eigenvalues are associated with nearby double eigenvalues that occur at geophysically relevant values of Λ and n.

2.2 Model and Problem Set Up

The hydromagnetic problem is formulated in terms of cylindrical polar coordinates (s, ϕ, z) and our model consists of an infinite cylindrical annulus (inner radius s_i, outer radius s_o) containing an incompressible conducting fluid and permeated by a toroidal magnetic field. Either insulating or perfectly conducting boundary conditions will be applied to the inner and outer cores. A more realistic geophysical model would use a spherical geometry with the inclusion of buoyancy forces and under a prescribed differential rotation. Whilst this model is more representative of the geodynamo, a simpler model, such as the one we employ, permits a clearer and quicker exploration of the parameter space whilst retaining most of the essential physics.

2.2.1 Perturbation equations and the basic state

Here, following on from the work done by Fearn (1983a,b;1984,1988), we perform a linear stability analysis on our rapidly rotating hydromagnetic system. In a reference frame rotating with the Earth, $\mathbf{\Omega}_0 = \Omega_0 \mathbf{1}_z$, the evolution of the hydromagnetic system is governed by the Navier-Stokes and magnetic induction equations and by the incompressibility constraint. Here we make the magnetostrophic approximation and neglect both viscous and inertial forces in the momentum equation (2.1) as they are judged to have little effect over our chosen timescale (2.5). The linearised, perturbation equations are, in the absence of differential rotation and buoyancy:

$$\mathbf{1}_z \times \mathbf{v} = -\nabla \Pi + [(\nabla \times \mathbf{B}_0 \times \mathbf{b} + (\nabla \times \mathbf{b}) \times \mathbf{B}_0], \tag{2.1}$$

$$\frac{\partial \mathbf{b}}{\partial t} = \nabla \times (\mathbf{v} \times \mathbf{B}_0) + \Lambda^{-1} \nabla^2 \mathbf{b}, \tag{2.2}$$

$$\nabla \cdot \mathbf{v} = 0. \tag{2.3}$$

where it is understood that the magnetic $\mathbf{B}$ and flow $\mathbf{U}$ fields take their following, perturbation form:

$$\begin{aligned} \mathbf{B}(s,\phi,z) &= \mathbf{B}_0(s) + \mathbf{b}(s,\phi,z), \\ \mathbf{V}(s,\phi,z) &= \mathbf{V}_0 + \mathbf{v}(s,\phi,z). \end{aligned} \tag{2.4}$$

We have non-dimensionalised length on the outer cylindrical radius s_o and on the 'slow' magnetohydrodynamic timescale τ_s

$$\tau_s = 2\Omega_0/\Omega_M^2 \quad \text{where} \quad \Omega_M = B_M/s_o\sqrt{\mu\rho} \tag{2.5}$$

so called because events on this timescale are slow compared with the 'fast' inertial timescale (Ω_0^{-1}). Here, Ω_M is the Alfvén frequency. Velocities are non-dimensionalised on s_o/τ_s and the magnetic field on B_M, see (2.6). The basic state we impose on the system takes the form

$$\mathbf{B}_0 = B_M s F(s)\mathbf{1}_\phi \quad \text{and} \quad \mathbf{V}_0 = \mathbf{0} \tag{2.6}$$

where B_M is a typical magnitude of the magnetic field, $\mathbf{1}_\phi$ is the azimuthal unit vector, and we have here chosen the function F to be:

$$F(s) = [2/(1 - s_{\text{ib}}^\alpha)]^2(1 - s^\alpha)(s^\alpha - s_{\text{ib}}^\alpha) \tag{2.7}$$

Here, the basic state can be changed by choosing different values of α. In this investigation we look at the cases $\alpha = 1, 2$. The basic state (2.6) has already been used extensively by Fearn (1983a,b, 1984, 1988) and is believed to be representative of that in the Earth since it vanishes at the inner and outer core boundaries $s = s_{\text{ib}} = s_{\text{i}}/s_{\text{o}}$ and $s = 1$. The field F is also known to be susceptible to both resistive and ideal types of instabilities, Fearn (1983b,1988). The term s_{ib} is the non-dimensionalised inner boundary radius and in this investigation, $s_{\text{ib}} = 0.35$.

2.2.2 The eigenvalue problem

The perturbation equations (2.1),(2.2) and (2.3) along with the basic state (2.6) and either perfectly conducting or insulating, rigid boundary conditions are separable in ϕ, z and t, so a modal expansion of the form

$$V(s,\phi,z,t) = v(s)\exp[i(m\phi + nz - \omega t)] \tag{2.8}$$

may be substituted for the pressure Π and any of the components of the perturbation magnetic or flow fields. The variables Π, b_ϕ and v_ϕ are eliminated from the equations [using equations (2.1)$\cdot\mathbf{1}_\phi$ and (2.3)]. The resulting equations then reduce to a fourth-order system, see Fearn (1983a), of two ordinary differential equations in s upon using the first two components of the momentum equation (2.1) to eliminate v_s and v_z. The annular region $s_{\rm ib} \leq s \leq 1$ was then divided up into N intervals and fourth order finite difference operators were substituted for the differential operators and we obtained the matrix eigenvalue problem

$$\mathbf{A}\mathbf{x} = i\omega\mathbf{x} \tag{2.9}$$

where, as a result of the difference operators, the matrix $\mathbf{A}$ is an $[2(N-1)]^2$ banded n-diagonal matrix (with $n \ll N$) and the eigenvector $\mathbf{x}$ has the form

$$\mathbf{x} = [b_{s,1}, \ldots, b_{s,N-1}, b_{z,1}, \ldots, b_{z,N-1}]^{\rm T} \tag{2.10}$$

with $b_{s,i} = b_s(s_{\rm ib} + i\Delta s)$ and $\Delta s = (1 - s_{\rm ib})/N$. The matrix eigenvalue problem was then solved using two methods: the LR algorithm, and the method of inverse iteration. Each method has its own merits: inverse iteration requires a rough estimate of the eigenvalue and converges to the eigenvalue closest to this guess; the LR algorithm requires storage space for the entire matrix and computes the entire eigenvalue spectrum. Consequently, for a general $[2(N-1)]^2$ matrix, complete spectrum calculations become very expensive for large N. However, in the case of inverse iteration, as $\mathbf{A}$ is an n-diagonal matrix, the required storage space is linear in N as is the cost. For a more detailed description of both methods, see either Fearn (1979b) or Fearn and Proctor (1983a,b). The 'Two Phase Method', discussed in the next section, utilizes both of these methods in identifying and locating double eigenvalue points.

2.3 Identification and Location of Double Eigenvalues

Certain pairs of eigenvalues, distinct at a particular set of parameter values, coalesce into one double eigenvalue (both eigenvalues equal) when viewed from another point

in the parameter space. For example, suppose that t_1 and t_2 are such a pair of distinct eigenvalues found at the point (Λ_0, n_0) and suppose further that when t_1 and t_2 are viewed at the parameter values (Λ_d, n_d) they coalesce to form the double eigenvalue t_d. If t_1 is subsequently tracked around a closed contour starting and ending at (Λ_0, n_0) which encloses (Λ_d, n_d), then traversing this contour will result in the continuous deformation of t_1 into t_2. If one now takes t_2 and tracks it around the same contour, then the original eigenvalue, t_1, is returned. If more than one double eigenvalue is enclosed, then more than one permutation of eigenvalues may occur on successive journeys around the loop. For example, t_1 may deform into t_2 and t_2 into t_3 before t_3 deforms back to t_1. On the other hand, if no double eigenvalues are enclosed by the contour, then the tracked eigenvalue will smoothly change back into itself. This change is not a spurious result generated by our numerical procedure, it is a true mathematical phenomena and a full treatment is given by Jones (1987).

Here we chose our contours to be rectangles and used the following 'Two Phase Method' to identify and then, when necessary, actually find the precise location of a double eigenvalue to within a specified tolerance (typically, three decimal places). The Two Phase Method is, in many ways, much like the bisection method followed by Newton-Raphson technique for finding zeros in simple calculus. However, because our parameter space is two dimensional, instead of halving our interval of interest at each 'bisection-step' we quarter our region at each iteration.

2.3.1 First Phase: Tracking and Quartering

The method of inverse iteration as described by Fearn (1990), was used to track eigenvalues around closed contours in the parameter (Λ, n)-space. Jones (1987) pioneered the use of rectangles in his treatment. Such a rectangle looks like:

$$\begin{array}{ccc} (\Lambda_0, n_0) & \longleftarrow & (10\Lambda_0, n_0) \\ \downarrow & & \uparrow \\ (\Lambda_0, 0.1n_0) & \longrightarrow & (10\Lambda_0, 0.1n_0) \end{array}$$

Each side of the rectangle was split up into *NSTEPS* divisions (typically, *NSTEPS*= 201). On the first three steps the 'corner' eigenvalue is used as an estimate for its tracked value at the next three nodes along one side of the rectangle. Once a guess is given, inverse iteration attempts to converge to a better estimate of the eigenvalue

at that point in (Λ, n)-space. After the first three nodes, quadratic interpolation is used to estimate the next successive eigenvalue. The process begins afresh at each corner and the original and final eigenvalue are noted and compared for change on completion of a rectangle.

Once a rectangle has been traversed and the eigenvalue is observed to deform into another, that rectangle is then cut into four smaller rectangles and each is then examined individually in the manner described. Once the appropriate 'quarter' (during the traversal of which, the eigenvalue deforms) has been identified, the process begins again by quartering the quarter.

2.3.2 Second Phase: Newton-Raphson

As the First Phase proceeds we steadily home in on the region of parameter space containing the double eigenvalue and the eigenvalues which permute into one another grow closer and closer together. When they are sufficiently close to one another, in the same spirit as in the elementary calculus, we switch to a Newton-Raphson type procedure to home in more rapidly on the double. We define the quantities

$$\alpha(\Lambda, n) = (p_1 - p_2)^2, \tag{2.11}$$

$$\beta(\Lambda, n) = (s_1 - s_2)^2, \tag{2.12}$$

where p_i and s_i are the corresponding growth rates and frequencies of the two eigenvalues $(i = 1, 2)$. A 2D Newton-Raphson technique is then applied to these quantities. The technique fails when simply applied to $(p_1 - p_2)$ or $(s_1 - s_2)$ as these functions are not analytic in the parameters (cf. the square root function at the origin). A more detailed explanation is given by Jones (1987). The steps in the Newton-Raphson method are:

$$\alpha(\Lambda_i, n_i) = (\Lambda_i - \Lambda_{i+1})\left.\frac{\partial \alpha}{\partial \Lambda}\right|_i + (n_i - n_{i+1})\left.\frac{\partial \alpha}{\partial n}\right|_i, \tag{2.13}$$

$$\beta(\Lambda_i, n_i) = (\Lambda_i - \Lambda_{i+1})\left.\frac{\partial \beta}{\partial \Lambda}\right|_i + (n_i - n_{i+1})\left.\frac{\partial \beta}{\partial n}\right|_i, \tag{2.14}$$

where all the values at the ith iteration are known. Equations (2.13) and (2.14) are easily inverted to give Λ_{i+1} and n_{i+1} explicitly.

For this stage in the process, we must obtain our eigenvalues using the more expensive LR algorithm. This is necessary since inverse iteration is not able to

distinguish between the two eigenvalues as they grow closer and closer together. When sufficient stages of the First Phase have been completed, the eigenvalues are close enough so that we can readily pick them out as being the pair of eigenvalues that are closest together in the complete spectrum given by LR.

2.3.3 Labelling Double Eigenvalues

Once a double eigenvalue has been identified either to finite numerical precision (3 decimal places) at particular values of the parameters (Λ_d, n_d) or as residing within some closed 'permutation' contour we then wish to label that double eigenvalue by the behaviour exhibited as $\Lambda \to \infty$. It must be emphasized that we are not classifying the double eigenvalue. The labelling will later serve as an illustration of the problems associated with any attempt at mode categorisation which is subject to the distribution of double eigenvalue points. This problem is addressed in the final section.

The double eigenvalues are labelled by their behaviour as both eigenvalue parts (i.e., the parts that when followed to (Λ_d, n_d) constituted the double) were individually tracked with increasing Λ from the starting corner of the permutation contour. It was necessary to track each part from this location since inverse iteration would not have been able to separate each mode as Λ increased from Λ_d.

The labelling was done as follows depending on which eigenvalue part resembled an ideal or resistive mode as $\Lambda \to \infty$:

- RR – both eigenvalue parts appeared to be of the resistive type,
- II – both eigenvalue parts appeared to be of the ideal type,
- RI/IR – first/second eigenvalue part appeared ideal, second/first appeared resistive.

In the mixed case, above, we have distinguished between doubles of type RI and IR since the ordering of the letters will match to the order of the eigenvalues in Tables 2.3 and 2.4 below, and allow us to indicate which part exhibited which trait.

2.4 Results

Before we tabulate and discuss results gathered with various fields and azimuthal wavenumbers we detail the discovery of a particularly interesting double eigenvalue that illustrates the search process well.

2.4.1 Acquiring a Resistive-Ideal Type Double Eigenvalue

In the case of insulating boundary conditions, Fearn (1988) discovered that for the non-monotonic basic state given when $\alpha = 1$, see (2.6), and an azimuthal wavenumber $m = 2$ the first marginally stable, ideal mode occurs at $(\Lambda, n) = (501, 9.601)$ with an eigenvalue of $-0.9358i$. We track this eigenvalue around the closed, rectangular path given by

$$\mathcal{R} = \{(\Lambda, n) : \ 28.17 \leq \Lambda \leq 501.0, \ 0.5399 \leq n \leq 9.601\} \tag{2.15}$$

in a clockwise manner as described in Section 2.3.2. The tracking of each eigenvalue around $\mathcal{R}$ was observed to be smooth and continuous with each inverse iteration step never needing more than six iterations to converge. The results are recorded in Table 2.1, below:

Table 2.1: Tracking the marginally stable eigenvalue around the contour $\mathcal{R}$.

	Λ	n	Eigenvalue
(i)	501.0	9.601	$-0.0000 - 0.9358i$
(ii)	501.0	0.540	$-1.5162 - 0.3034i$
(iii)	28.17	0.540	$-9.5777 - 0.5776i$
(iv)	28.17	9.601	$-7.9206 - 0.4347i$
(v)	501.0	9.601	$-0.7437 + 0.0276i$

Starting with the eigenvalue (v), at $(\Lambda, n) = (501.0, 9.601)$, we track this 'partner' eigenvalue, clockwise, around the contour $\mathcal{R}$. The corner information is tabulated in Table 2.2, below:

Table 2.2: Tracking the partner eigenvalue around the contour $\mathcal{R}$.

	Λ	n	Eigenvalue
(v)	501.0	9.601	$-0.7437 + 0.0276i$
(vi)	501.0	0.540	$-4.9155 + 9.1482i$
(vii)	28.17	0.540	$-11.860 + 19.025i$
(viii)	28.17	9.601	$-5.4318 - 0.8546i$
(ix)	501.0	9.601	$-0.0000 - 0.9358i$

Thus, appealing to the results of the previous section, a double eigenvalue point must reside somewhere within the rectangular region $\mathcal{R}$. The eigenfunctions corresponding to the perturbed axial flow v_z and radial magnetic field b_s at each corner of $\mathcal{R}$ during the two loops are reproduced in a series of eighteen "snapshots" in Figures 2.1 and 2.2. The eigenfunctions have been normalised by dividing through by the quantity $b_z^r(s) + ib_z^i(s)$ which has been evaluated at $s = s_{max}$ giving the maximum of its modulus over $s \in [s_{\text{ib}}, 1]$.

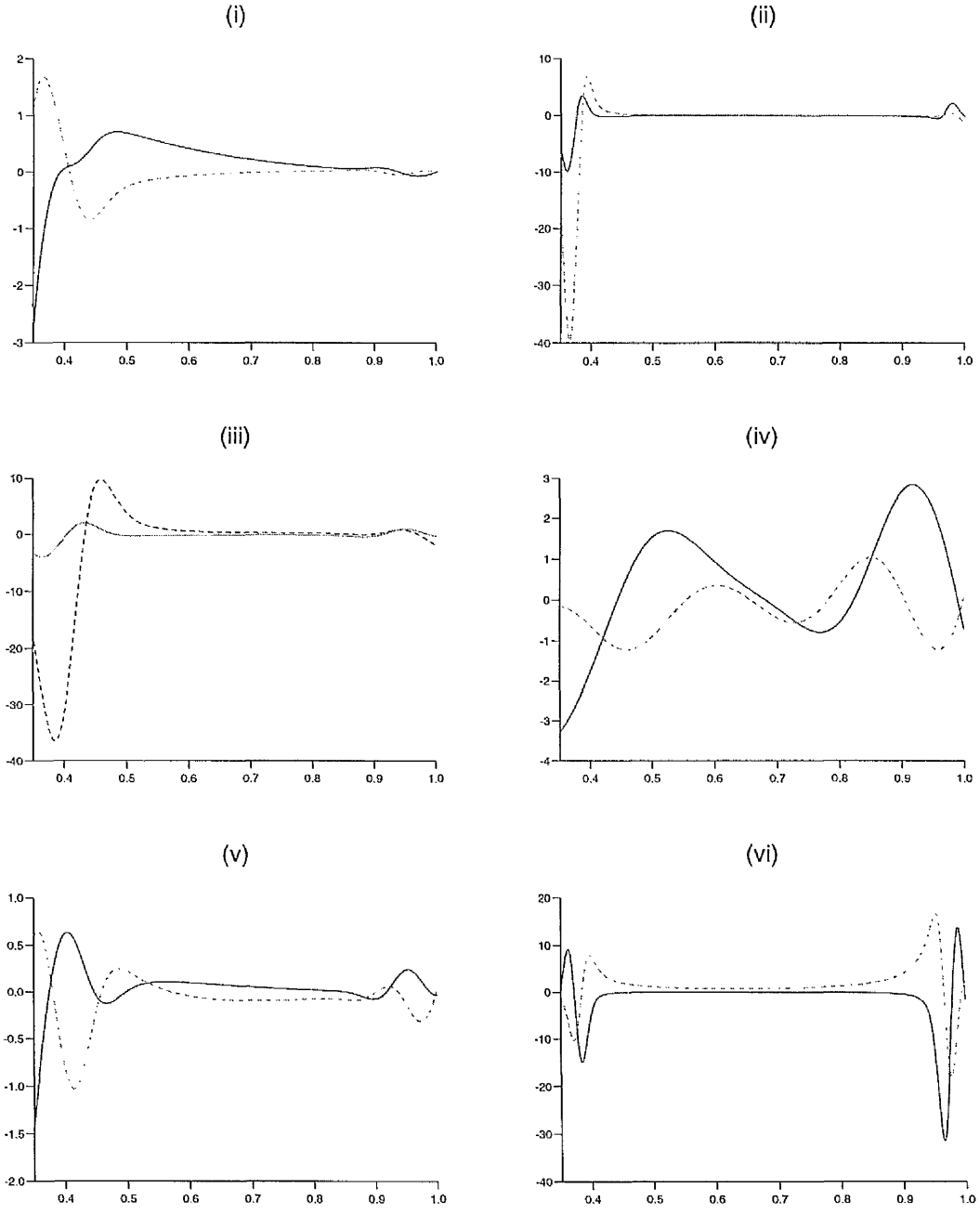

Figure 2.1: The first 6 of 9 snapshots showing the perturbed axial flow at each corner of $\mathcal{R}$ as the marginally stable eigenvalue $-0.9358i$ is tracked twice around $\mathcal{R}$. Each frame corresponds to the eigenfunction at the successive 'corner' of $\mathcal{R}$. The full line is the real part of the eigenfunction and the dashed line the imaginary part. The numerals correspond to the numerals on Tables 2.1 and 2.2.

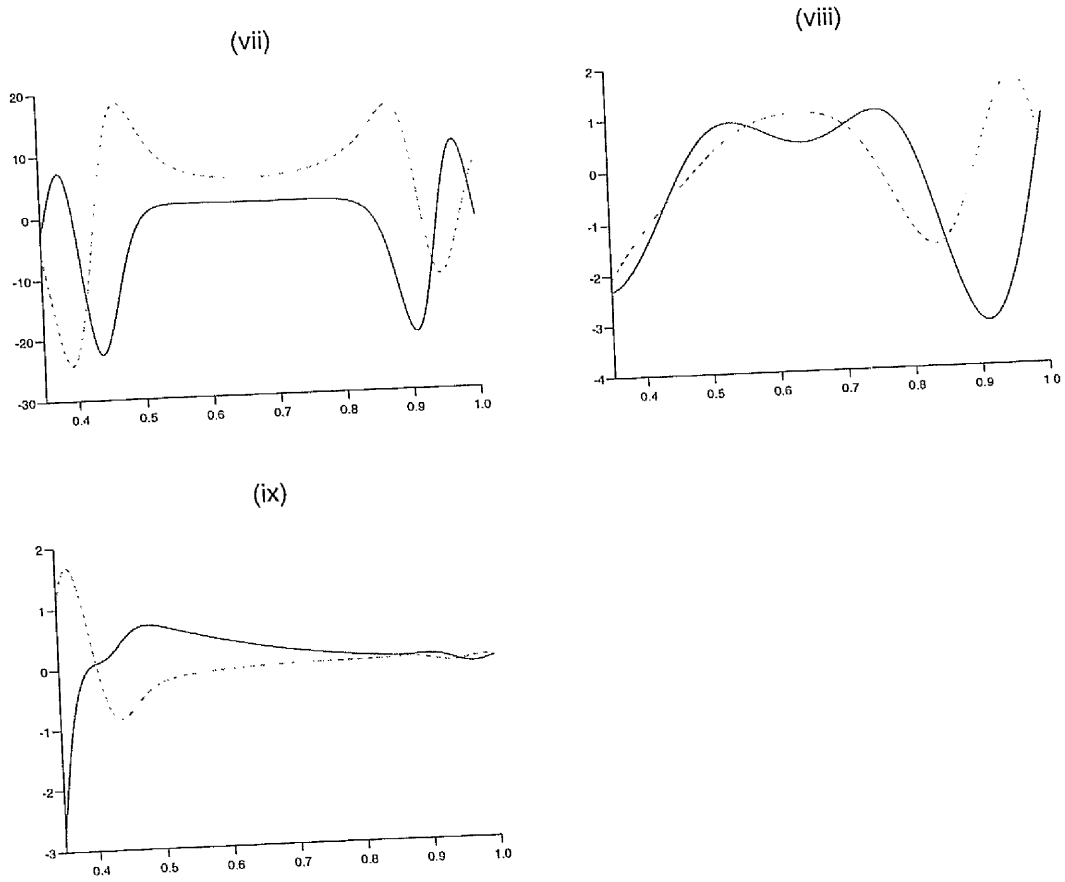

Figure 2.1 continued.

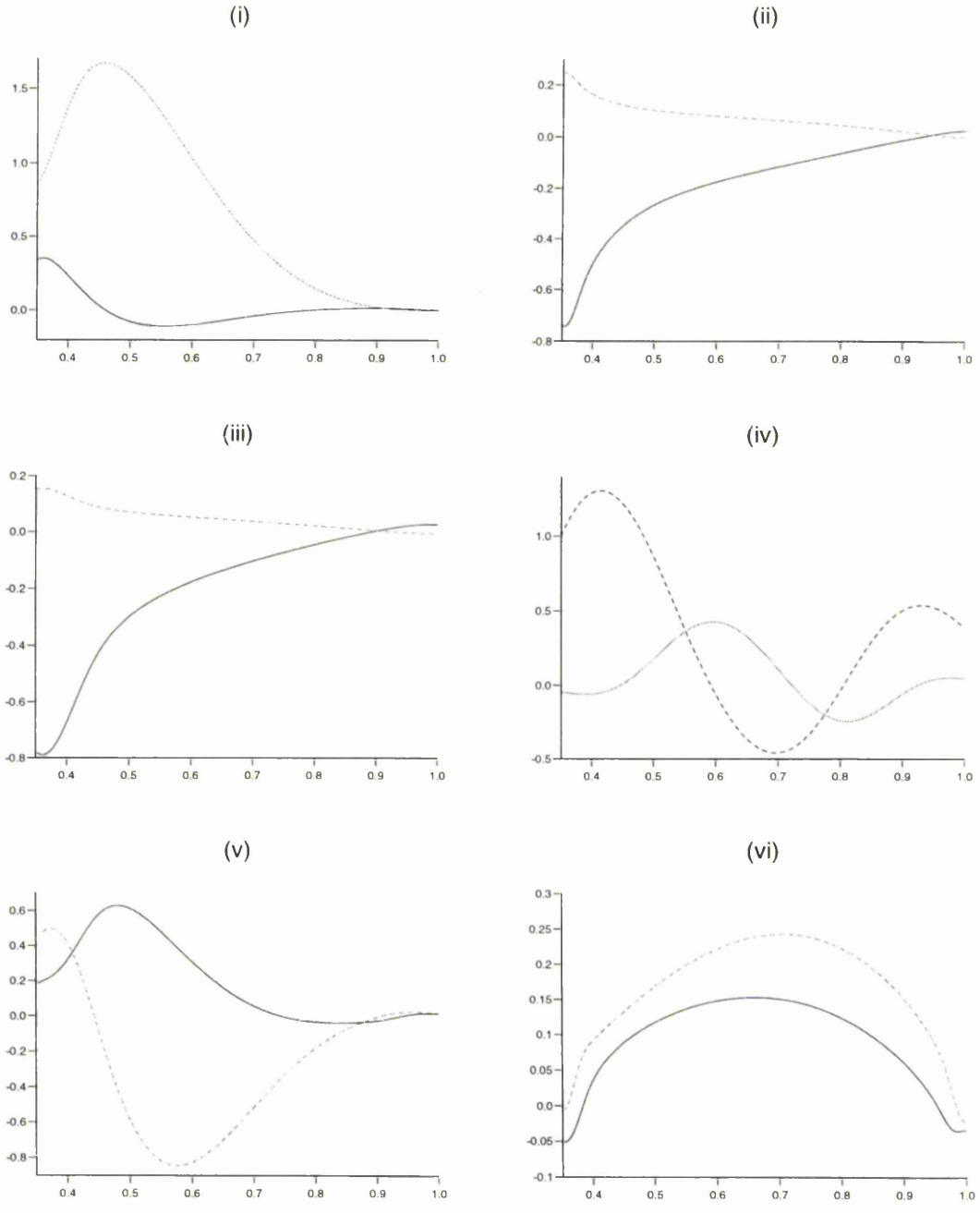

Figure 2.2: Similarly to Figure (2.1), the first 6 of 9 snapshots showing the perturbed radial magnetic field at each corner of $\mathcal{R}$.

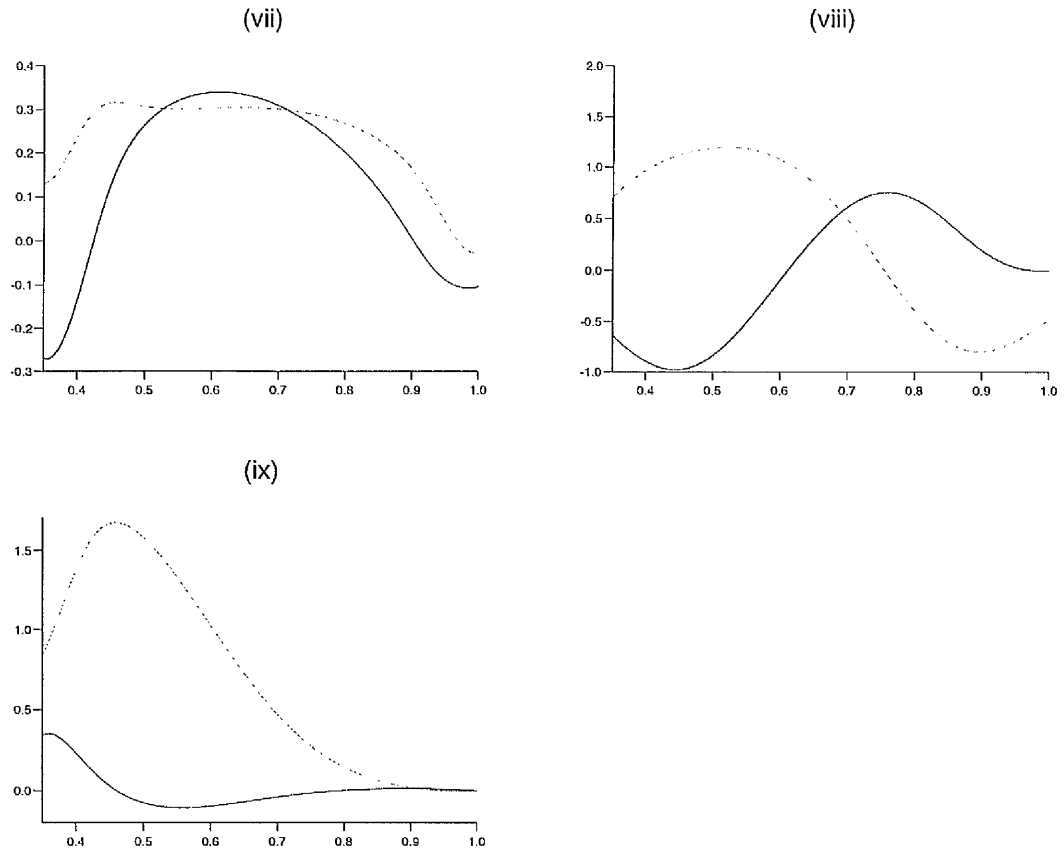

Figure 2.2 continued.

Although the main thrust of this work did not require us to discover the exact location of any one double eigenvalue point, on this occasion we illustrate our 'Two Phase Method' for locating such points. The region $\mathcal{R}$ is first 'cut' into the following four 'quarters'

$$\begin{aligned}
\mathcal{R}_{11} &= \{(\Lambda, n):\ 28.17 \leq \Lambda \leq 118.8,\ 0.540 \leq n \leq 2.277\}, \\
\mathcal{R}_{12} &= \{(\Lambda, n):\ 118.8 \leq \Lambda \leq 501.0,\ 0.540 \leq n \leq 2.277\}. \\
\mathcal{R}_{21} &= \{(\Lambda, n):\ 28.17 \leq \Lambda \leq 118.8,\ 2.277 \leq n \leq 9.601\}, \\
\mathcal{R}_{22} &= \{(\Lambda, n):\ 118.8 \leq \Lambda \leq 501.0,\ 2.277 \leq n \leq 9.601\},
\end{aligned} \tag{2.16}$$

Because of the nature of the prior tracking and because the marginally stable eigenvalue and its partner reside at the top right hand corner of $\mathcal{R}_{22}$ then the next step in locating our doublet requires us to track each part around this contour. Here, we observe no interchange in eigenvalues and, indeed, on returning to the starting point, each eigenvalue continuously deformed back into itself. This leads us to the conclusion that no double eigenvalue lies within $\mathcal{R}_{22}$, but more importantly, *because* there are no doubles present in this region then we have *successfully* tracked each part right around the contour. We are now able to confidently track either partner around each of the remaining contours $\mathcal{R}_{11}, \mathcal{R}_{12}$ and $\mathcal{R}_{21}$. Once we have located the appropriate contour whose traversal produces a change in eigenvalue then we have a new and better estimate of where the doublet actually lies.

As the process of quartering and traversing contours is continued the tracked marginally stable eigenvalue and its partner grow closer and closer together. Eventually, eigenvalue and partner are close enough together so that we may use the Newton-Raphson technique of Section 2.3.3 in our search process. In this particular example, the Newton-Raphson procedure was able to give an estimate of the double eigenvalue to within three decimal places at the point $\Lambda = 28.89$, $n = 3.472$ with value $-4.79 + 0.821i$.

This particular double eigenvalue can be labelled RI using our criterion of examining the growth rate and frequency of both partners as they are tracked with increasing Λ. In this example, both parts were tracked from their values at the point $(\Lambda, n) = (501.0, 9.601)$ in parameter space. Figures 2.3(a) and (b), below, reproduce the trends for the resistive and ideal instabilities' growth rates and frequencies. Observe how the growth rate and frequency of the eigenvalue in (a) levels off at around

$p = 0.133$ and $s = -0.481$ as $\Lambda \to \infty$. This is indicative of an ideal instability. On the other hand, in (b) the magnitude of the growth rate and frequency can be seen to steadily decay towards zero as Λ increases. This is typical of the resistive class of instability. One point which is worth noting is that the trend for the ideal mode is analogous to the trend of growth rate versus magnetic Reynolds' number (measuring the strength of the shear flow) for a fast dynamo [see Hollerbach *et al* (1995)]. The trend for the resistive mode is similar to that of a slow dynamo.

Another point of interest associated with this particular double eigenvalue is that it shares the same ideal mode as another double eigenvalue in close proximity. Fearn (1988) located the first marginally stable resistive mode under the same boundary conditions, basic state and azimuthal wave number as the above example. The marginal, resistive-type mode occurs at $(\Lambda, n) = (28.95, 9.487)$ with eigenvalue $-0.928i$. Using the Two Phase Method it was found that this resistive eigenvalue is associated with the RI double eigenvalue point $-6.72 - 0.605i$ located at $(\Lambda, n) = (24.88, 10.91)$. The ideal part of this double is actually the ideal part of the previous double but seen at a different point in the parameter space. This is best illustrated in conjunction with Figure 2.3(c). If we track the ideal part of the double eigenvalue D_1 occurring at S_1 around the closed rectangle $S_1PS_2QS_1$ then on completion of a loop, no change is observed. More importantly, on arrival at S_2, the ideal eigenvalue has continuously deformed into the ideal component of the double eigenvalue D_2. If we similarly take the resistive component of D_1 occurring at S_1 and track it around the loop $S_1PS_2QS_1$ then no change is observed. However, on arrival at S_2, the resistive eigenvalue has not deformed into the resistive component of D_2 and so the resistive components of D_1 and D_2 are distinct.

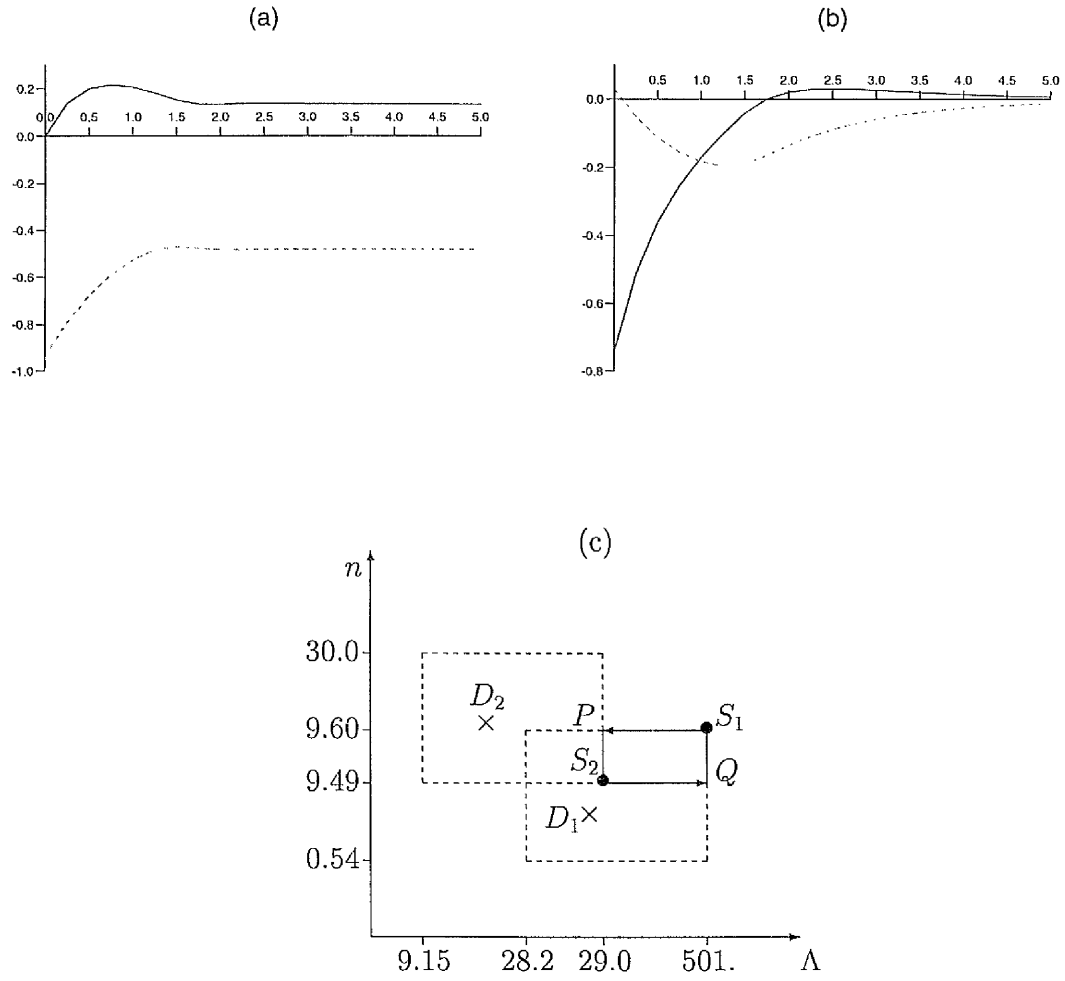

Figure 2.3: Top figures: the growth rates and frequencies of the (a) ideal and (b) resistive instabilities associated with the double eigenvalue $-4.79 + 0.821i$ as they are tracked with increasing Λ from the point $(\Lambda, n) = (501.0, 9.601)$ plotted against x where x is given in $\Lambda = 501.0 \times 10^x$. The solid line represents the growth rate p and the dashed line, the frequency s. (c) Bottom figure: an illustration of the relative positions of the two permutation contours (shown as one dashed and one full rectangle), with starting points S_1 and S_2. The marginally stable resistive mode, $-0.9280i$, found by Fearn (1988) occurs at the point S_2 whereas his marginally stable ideal mode, $-0.9358i$, occurs at S_1. Both double eigenvalues D_1 and D_2 share the same ideal component but different resistive components.

2.4.2 Summary of other results

When we began this study we did not know where double eigenvalues were located in parameter space or even if they existed at all for our hydromagnetic stability problem. It was decided that a suitable starting point for our investigation lay in the region of parameter space that had $\Lambda, n \sim \mathrm{O}(1)$ as these values are directly relevant to the geophysical problem. Fearn (1983b,1988) conducted a linear stability analysis into the location of marginally stable eigenvalues for perfectly conducting and insulating boundary conditions. We follow on from that work and investigate whether any of those marginally stable eigenvalues are associated with double eigenvalues in their close proximity. Using the non-monotonic basic state (2.6) we examine two cases, $\alpha = 1, 2$. We also look at the two values of the azimuthal wavenumber: $m = 1, 2$. As already noted, it was not the main thrust of this work to locate the precise points at which the double eigenvalues occur. In the results, tabulated below, we cite the rectangle within which the double eigenvalue was contained, its type and the values of the two 'partner' eigenvalues that were seen to interchange on traversing that rectangle. From this data, it is readily seen that double eigenvalues are not uncommon and that they are associated with marginally stable modes.

(i) Perfectly Conducting Boundaries:

Table 2.3: Results found for perfectly conducting boundary conditions.

				Eigenvalues		Rectangle	Double
α	m	Λ	n	1st Part	2nd Part	Traversed	Type
1	1	126.0	3.790	$-1.04i$	$-0.425 - 0.901i$	$126.0 \leq \Lambda \leq 1260$, $0.379 \leq n \leq 3.790$	IR
1	2	1250.	15.00	$-0.959i$	$-0.198 + 0.055i$	$1250. \leq \Lambda \leq 12500$, $1.500 \leq n \leq 15.00$	II
$*2$	1	28.15	2.235	$-1.90i$	$-3.425 - 0.170i$	$890.2 \leq \Lambda \leq 2815$, $0.707 \leq n \leq 2.235$	RI
2	2	1146.	11.61	$-0.775i$	$-0.156 + 0.048i$	$114.6 \leq \Lambda \leq 1146$, $1.161 \leq n \leq 11.61$	RI

In the search for doubles it frequently arose that in tracking eigenvalues around some rectangular contours more than one change was seen. In this event, it was found to be the case that more than one double was present within that region of parameter space. This could easily be remedied by further dividing that particular region into smaller and smaller pieces, as in Section 2.3.2, until tracking the appropriate eigenvalue around any such sub-region yielded only one such change. This occurred in the case $*$ where the closed loop followed consisted of firstly tracking the marginally stable eigenvalue at constant n to the top left hand corner of the rectangle cited, then traversing this rectangle in a counter-clockwise direction before finally returning to the start point (along the reverse of the initial path) at constant n. Successive completions of this closed contour yielded the interchange of the two partner eigenvalues in $*$.

(ii) Insulating Boundaries:

Table 2.4: Results found for insulating boundary conditions.

				Eigenvalues		Rectangle	Double
α	m	Λ	n	1st Part	2nd Part	Traversed	Type
$*1$	1	133.3	5.838	$0.049i$	$-1.102+0.670i$	$42.17 \leq \Lambda \leq 133.3$, $5.839 \leq n \leq 18.46$	RI
$\dagger 1$	2	501.0	9.601	$-0.936i$	$-0.744+0.028i$	$28.17 \leq \Lambda \leq 501.0$, $0.540 \leq n \leq 9.601$	IR
$\ddagger 1$	2	28.95	9.487	$0.160i$	$-5.196+0.288i$	$9.154 \leq \Lambda \leq 28.95$, $9.487 \leq n \leq 30.00$	RI
2	1	103.6	2.250	$-0.004i$	$-1.052+0.442i$	$103.6 \leq \Lambda \leq 1036$, $0.225 \leq n \leq 2.250$	RR
2	2	16.60	3.000	$-0.163i$	$-4.719+1.318i$	$16.60 \leq \Lambda \leq 52.49$, $3.000 \leq n \leq 9.487$	RR

Once again, in the case of $*$ and $\ddagger$, the marginally stable eigenvalues were tracked to the appropriate corner of the rectangle and tracked around that rectangle from

there as in the perfectly conducting example. The results † and ‡ are the cases already discussed in Section 2.4.1.

2.5 Discussion and Conclusions

In this investigation we have discovered double eigenvalues at every combination of basic state and azimuthal wavenumber we have tried. In one particular case, the $\alpha = m = 1$ case, we produced the complete eigenvalue spectrum from our LR algorithm with a mesh size, or truncation of $N = 100$. We then automated Section 2.3.2 of our rectangular search pattern taking each eigenvalue, in turn, and tracking it around various rectangles in the plane. Many double eigenvalues were found to lie within our 'test' region

$$\mathcal{D} = \{(\Lambda, n) : \ 1 \leq \Lambda \leq 10^4, \ 0.05 \leq n \leq 5\}. \tag{2.17}$$

We believe that it is not unusual for double eigenvalue points to occur often, and that they are not simply restricted to one particular basic state. Indeed, as Jones (1987) has discovered, they do exist in other physical problems such as plane Poiseuille flow. It is also important to note that, in the hydromagnetic problem, they are not confined to a small region of the parameter space and they do occur at geophysically relevant values of Λ and n.

It is now obvious that following eigenvalues along contours in parameter space is heavily path dependent in a similar way to flow fields which are potential everywhere except at singularities. In fact, for stability analyses in general, extreme care must be taken to ensure that whilst tracking eigenvalues in parameter space, the nearby presence of double eigenvalue points do not 'swap' one eigenvalue (and hence the eigenvector) for another. This could have the effect of overestimating critical parameter values. The method used by Fearn (1983b,1984,1988) to find the critical parameter values was to firstly produce a complete list of the eigenvalue spectrum using the LR algorithm at low truncation (say, $N = 50$), then to reduce Λ until only one mode was unstable. At this point all eigenvalue calculations have been done using the LR algorithm and are free from the problems so far discussed involving double eigenvalues. The next step involved increasing the level of truncation considerably (to perhaps $N = 500$) using inverse iteration. This was necessary to better

resolve the instability and to ensure that it was not a spurious result due to the lack of resolution. The instability was then tracked along a path in parameter space to find Λ_c (i.e. $p = 0$) and then to minimise $\Lambda_c(n)$. This involves following a path in (Λ, n)-space. As we have already seen, this is fraught with difficulty. The proximity of double eigenvalue points could lead to a wrong conclusion about such critical parameter values. This problem can be circumvented by frequently producing the complete eigenvalue spectrum via the LR algorithm. However, when we consider the cost involved in complete spectrum calculations, especially at high truncation, it is unclear how often we should produce such lists.

We note immediately that this problem extends to our method of labelling magnetic instabilities. Our work clearly shows that at $\Lambda \sim O(1)$ we cannot make a distinction between the ideal and the resistive instability. This phenomena is well illustrated in the $\alpha = m = 1$ perfectly conducting boundary result, see Figure 2.4. When we try to track the partner of the marginally stable eigenvalue to the critical value of its parameters (the point in parameter space giving rise to instability first) we discover that the partner has changed from its resistive character to that of an ideal mode. Although we never completed a closed loop in parameter space, this eigenvalue, and hence its character, have continuously deformed into another eigenvalue with, perhaps, a different character. The method of labelling an eigenvalue by its behaviour as $\Lambda \to \infty$ cannot therefore be considered as providing a useful method of magnetic mode classification.

In our study of the double eigenvalues and their effect in the hydromagnetic stability problem we have tried to provide a concise set of results that clearly illustrate the problems associated with following eigenvalues across parameter space. We have shown that it is not unusual for marginally stable modes to be associated with double eigenvalues and we have shown that this phenomena occurs for a variety of basic states and azimuthal wavenumbers. Although the true spherical problem permits only discrete values of the axial wavenumber there are many more continuous parameters that we may vary (such as the Rayleigh number) in the geophysically relevant spherical geometry to establish the reality of this problem.

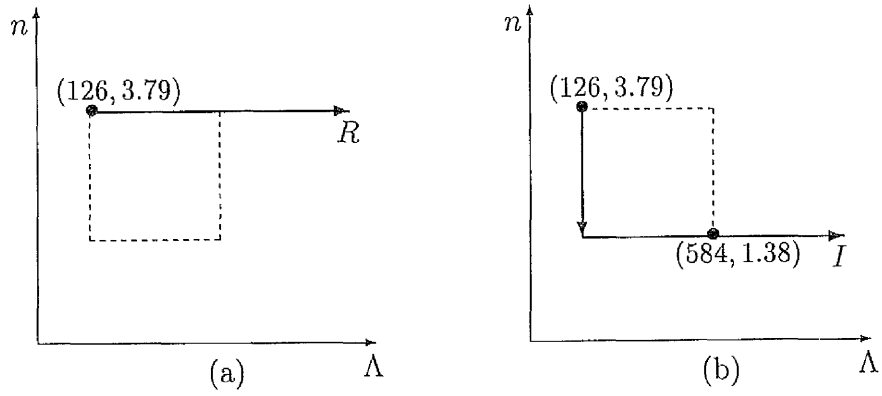

Figure 2.4: An illustration showing that by simply traversing the 'L' shaped contour of (b) from (126, 3.79) to (584, 1.38) the resistive instability of (a) changed character to one of ideal type in (b). The dashed rectangle contains a double eigenvalue.

Chapter 3

The Geostrophic Flow and Magnetic Instability

3.1 Introduction

In this chapter we consider the nonlinear stability of axisymmetric basic fields which depend only on the cylindrical radial coordinate s. The rapidly rotating hydromagnetic system is considered in the absence of buoyancy forces to concentrate on purely magnetic instabilities. The only nonlinear effect is that of the geostrophic flow V_G, and the dependent variables have been scaled with $E^{1/4}$ in order to remove the explicit appearance of the Ekman number from the governing equations. Since V_G is a function of radius and time only, the problem remains separable in ϕ and z and hence computational requirements remain light. In this way, we examine (i) the possibility of the geostrophic flow inducing subcriticality [i.e. Λ(nonlinear onset) $< \Lambda_c$] and (ii) Ekman states as stepping stones to Taylor states.

We find that, under the magnetostrophic approximation and with the geostrophic flow as the only nonlinearity, subcriticality exists for the most unstable mode in many basic field configurations and aspect ratios that are considered. Where this subcriticality occurs, however, the Ekman branch is unstable. For other choices of basic field we find that field equilibration by the geostrophic flow can exist. These stable Ekman solutions are supercritical in nature.

The chapter is ordered as follows: in Section 3.2 we set up the magnetic stability problem. Section 3.3 describes the linear and nonlinear methods that were

employed in the time-stepping calculations and also details the various tests that were performed to check the computer program. Section 3.4 contains the results, linear and nonlinear, and we conclude with a discussion in Section 3.5.

3.2 Model and Equations

3.2.1 Cylindrical Annular Model

Using cylindrical polar coordinates (s^*, ϕ, z^*) we model the Earth by a cylindrical annulus $\mathcal{A}^*$ of inner and outer radii s_i and s_o, respectively, bounded in axial extent by the flat, horizontal plates $z^* = \pm d$. The annular region

$$\mathcal{A}^* = \{(s^*, \phi, z^*) \; : \; s_i < s^* < s_o, \; |z^*| < d\} \tag{3.1}$$

is filled with an incompressible, isothermal conducting fluid of constant density ρ_0 and rapidly rotates with angular frequency Ω_0 about the z^*-axis. The cylindrical annular model was chosen over the more realistic geometry of the spherical shell for a number of reasons. Firstly, this work represents a progression from previous work completed in the annular geometry [see, for example, FLMO or Hutcheson & Fearn (1995a,b, 1996, 1997)]. We, like FLMO, will consider purely s-dependent basic states [see (3.8)] and as a result, retain separability in the azimuthal and axial directions. This allows the ϕ- and z-dependences to be parametrised by their azimuthal and axial wavenumbers, respectively. Consequently, the numerical resolution can be completely focussed on the radial dependence and this makes computation far less numerically intensive than with similar fields in the spherical geometry. It is worth noting that the cylindrical polar co-ordinate system is the natural co-ordinate system for evaluation of the geostrophic flow. If a spherical geometry were adopted, a transformation between the spherical and cylindrical grids would be required for every evaluation of the geostrophic flow.

Within the framework of a cylindrical annulus, the governing equations are not numerically intensive and a thorough exploration of the parameter space is possible. We believe that the cylindrical geometry retains much of the essential physics although, clearly, some features are missing [e.g., the difference in the flow field interior and exterior to the tangent cylinder of the Earth's inner core as analysed by

Hollerbach (1994) and Hollerbach & Proctor (1993)].

3.2.2 Governing Equations and the Magnetic Basic State

The time-evolution of an isothermal, electrically conducting fluid $\mathbf{V}^*$ and its associated magnetic field $\mathbf{B}^*$ is governed by the Navier-Stokes and magnetic induction equations. These, together with the fluid incompressibility constraint and the divergence free condition for the magnetic field complete our hydromagnetic system. In dimensional form, these are:

$$\rho_0 \left[\frac{\partial \mathbf{V}^*}{\partial t} + \mathbf{V}^* \cdot \nabla \mathbf{V}^* \right] + 2\boldsymbol{\Omega}_0 \times \mathbf{V}^* = -\nabla \Pi^* + \nu \nabla^2 \mathbf{V}^* + \mu^{-1} (\nabla \times \mathbf{B}^*) \times \mathbf{B}^*, \quad (3.2)$$

$$\frac{\partial \mathbf{B}^*}{\partial t} = \nabla \times (\mathbf{V}^* \times \mathbf{B}^*) + \eta \nabla^2 \mathbf{B}^*, \quad (3.3)$$

$$\nabla \cdot \mathbf{V}^* = \nabla \cdot \mathbf{B}^* = 0. \quad (3.4)$$

We nondimensionalise length on the outer annular radius s_o. The conducting fluid is then confined to the annular region $\mathcal{A} = \{(s, \phi, z) : s_{\rm ib} < s < 1, \ |z| < \zeta\}$ where $s_{\rm ib} = s_i/s_o$ and $\zeta = d/s_o$. In this work we take $s_{\rm ib} = 0.35$ and $\zeta = \pi/2$. Time is scaled with the slow magnetohydrodynamic (or dynamo) timescale

$$\tau_s = 2\Omega_0/\Omega_M^2, \quad \Omega_M^2 = B_M^2/s_o^2 \mu \rho. \quad (3.5)$$

Here Ω_M is the Alfvén frequency. The magnetic field is scaled by its maximum amplitude B_M as $\mathbf{B}^* = B_M \mathbf{B}$ and the flow as $\mathbf{V}^* = s_o \mathbf{V}/\tau_s$. We make the decompostions

$$\mathbf{B}(s, \phi, z, t) = \mathbf{B}_0(s) + \mathbf{b}(s, \phi, z, t) \quad (3.6)$$

$$\mathbf{V}(s, \phi, z, t) = [\mathbf{V}_0(s) + V_G(s, t)\mathbf{1}_\phi] + \mathbf{v}(s, \phi, z, t) \quad (3.7)$$

where $\mathbf{b}$ and $\mathbf{v}$ are small, but finite, perturbations to the flow and magnetic fields. Here, $\mathbf{1}_s, \mathbf{1}_\phi$ and $\mathbf{1}_z$ are the cylindrical polar base vectors. The imposed basic fields are defined as

$$\mathbf{B}_0 = sF(s)\mathbf{1}_\phi\,, \quad (3.8)$$

$$\mathbf{V}_0 = \mathcal{R}_m V_0(s)\mathbf{1}_\phi\,. \quad (3.9)$$

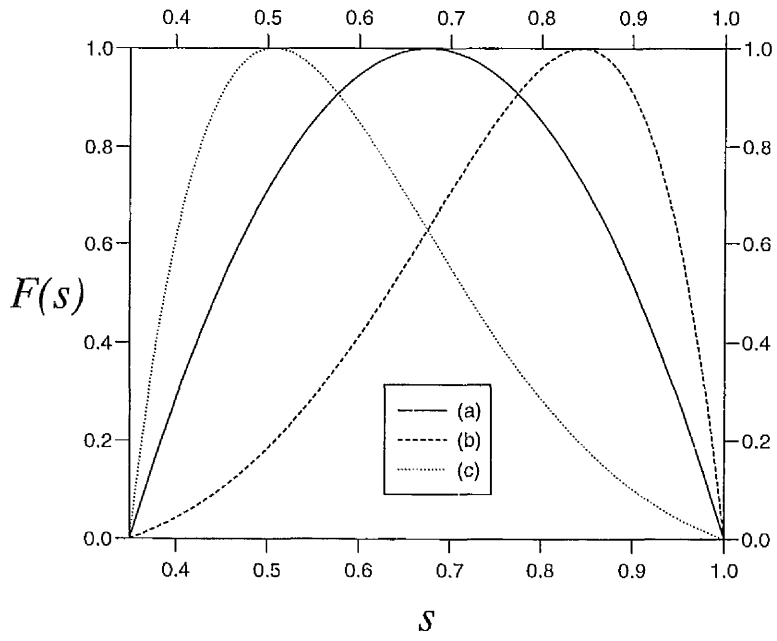

Figure 3.1: Profiles for the s-dependence $F(s)$ in the basic imposed fields (3.8) where (a) corresponds to (3.10), (b) to (3.11) and (c) to (3.12).

The geostrophic flow, $V_G(s,t)\mathbf{1}_\phi$, is dynamically determined through the modified Taylor's condition (1.15). Although we have decomposed the axisymmetric flow into an imposed field $\mathbf{V}_0$ and geostrophic flow $V_G\mathbf{1}_\phi$, we never enforce both simultaneously. Here we consider the effect of an imposed differential rotation or geostrophic flow separately. The forms we chose for F are

$$F(s) = [2/(1-s_{\rm ib})]^2(s-s_{\rm ib})(1-s) \tag{3.10}$$

$$F(s) = [2/(1-s_{\rm ib}^4)]^2(s^4-s_{\rm ib}^4)(1-s^4) \tag{3.11}$$

$$F(s) = [2/(1-s_{\rm ib}^4)]^2[(1+s_{\rm ib}-s)^4-s_{\rm ib}^4][1-(1+s_{\rm ib}-s)^4] \tag{3.12}$$

where (3.11) concentrates field to the CMB, (3.12) to the ICB and (3.10) to the middle of the annular gap. These choices of s-dependence were made so that $\mathbf{B}_0$ would vanish on the cylindrical surfaces $s = s_{\rm ib}$ and $s = 1$ which is consistent with the hidden toroidal component of the Earth's field. The fields (3.10), (3.11) have been used extensively in the past by, for example, Fearn (1983b), FLMO. The

Geodynamo model calculations of Glatzmaier & Roberts (e.g. 1995a,b) show field that tends to concentrate towards the ICB. The basic field (3.12) was included so that the stability of fields which concentrate to the ICB could be examined. Field profiles showing the various forms of $F(s)$ can be found in Figure 3.1.

Substituting the perturbation forms (3.7) and (3.6) into the nondimensionalised governing equations and neglecting all nonlinear terms except where V_G is involved, yields the perturbation equations

$$\Lambda Ro\left[\frac{\partial \mathbf{v}}{\partial t}+(\mathbf{V}_0+V_G\mathbf{1}_\phi)\cdot\nabla\mathbf{v}+\mathbf{v}\cdot\nabla(\mathbf{V}_0+V_G\mathbf{1}_\phi)\right]+\mathbf{1}_z\times\mathbf{v}$$
$$=-\nabla\pi+E\nabla^2\mathbf{v}+(\nabla\times\mathbf{B}_0)\times\mathbf{b}+(\nabla\times\mathbf{b})\times\mathbf{B}_0\,, \tag{3.13}$$

$$\frac{\partial \mathbf{b}}{\partial t}=\nabla\times(\mathbf{v}\times\mathbf{B}_0)+\nabla\times(\mathbf{V}_0\times\mathbf{b})+\nabla\times(V_G\mathbf{1}_\phi\times\mathbf{b})+\Lambda^{-1}\nabla^2\mathbf{b}, \tag{3.14}$$

$$\nabla\cdot\mathbf{b}=\nabla\cdot\mathbf{v}=0 \tag{3.15}$$

where $Ro=\eta/2\Omega_0 d^2$ is the Rossby number. Given the smallness of Ro and E we employ an approximation which is almost magnetostrophic: $Ro=0$ and $0<E\ll 1$. This allows us to neglect fluid inertia from (3.13) and an order analysis allows us to neglect the viscous term. However, viscosity remains important in the boundary layers and this is accommodated via the modified Taylor's condition. Thus, we obtain a solution which implicitly incorporates the viscous effects from the boundary layers and is valid everywhere in the inviscid mainstream.

3.2.3 Boundary Conditions

We impose no-normal flow, perfectly conducting boundary conditions on the horizontal plates, giving

$$\mathbf{1}_z\cdot\mathbf{v}=0,\quad \mathbf{1}_z\cdot\mathbf{b}=0\quad\text{and}\quad \mathbf{1}_z\times\mathbf{e}=\mathbf{0}\quad\text{on}\quad z=\pm\zeta. \tag{3.16}$$

where $\mathbf{e}$ is the perturbed electric field. In component form these are equivalent to

$$v_z=0,\quad b_z=0,\quad \frac{\partial b_z}{\partial\phi}=s\frac{\partial b_\phi}{\partial z}\quad\text{and}\quad \frac{\partial b_z}{\partial s}=\frac{\partial b_s}{\partial z}\quad\text{on } z=\pm\zeta. \tag{3.17}$$

The use of perfectly conducting boundary conditions is made for numerical convenience; for a purely s-dependent $\mathbf{B}_0$, the problem remains separable in z and good resolution in radius is then inexpensive. We use a Galerkin-type method to satisfy

the boundary conditions on the horizontal plates $z = \pm\zeta$ by making the substitutions

$$X = X_n(s,t)\cos\bar{n}(z+\zeta)e^{im\phi} + \text{CC} \tag{3.18}$$

$$Y = Y_n(s,t)\sin\bar{n}(z+\zeta)e^{im\phi} + \text{CC} \tag{3.19}$$

where X represents any of v_s, v_ϕ, b_s or b_ϕ and Y stands for either v_z or b_z. Here, CC stands for "complex conjugate". All functions with subscript $n \in [1,2,...)$ are complex. Here $\bar{n} = n\pi/2\zeta$ and since we have chosen $\zeta = \pi/2$, then $\bar{n} = n$. This gives an aspect ratio (cylindrical diameter to height) of $1:\pi/2$ in our model. In general, choosing $\zeta = \pi/2k$ restricts the range of possible $\bar{n}$ to the multiples kn. Because the most unstable mode in this model always corresponds to the mode with lowest $\bar{n}$ [see Fearn (1988)] then concentrating our attention on the k^{th} mode allows us to consider the most unstable mode in the system where $\zeta = \pi/2k$. This allowed us to study the effect of variation in height of our annulus without resorting to further calculations.

For the curved annular side walls we wish to impose perfect electrical insulating conditions as the Earth's mantle, to a very good approximation, acts as an insulator. Since the perturbed current density $\mathbf{j} = \nabla \times \mathbf{b}$ vanishes in the regions $s \leq s_{\text{ib}}$ and $s \geq 1$ then the magnetic field may be described by a magnetostatic scalar potential $U(s,\phi,z)$ such that

$$\mathbf{b}^{(e)} = -\nabla U. \tag{3.20}$$

On the surfaces $s = s_{\text{ib}}$ and $s = 1$ the interior field $\mathbf{b}$ must match to the exterior potential field $\mathbf{b}^{(e)}$. Upon applying the divergence free condition to $\mathbf{b}^{(e)}$ we find that U satisfies Laplace's equation $\nabla^2 U = 0$. If, for U, we associate an expansion similar to that given in (3.18) then one can show

$$b_{s,n} = \gamma_n b_{z,n} \qquad n \in [1,2,...) \tag{3.21}$$

where

$$\gamma_n = \begin{cases} -I_{m+1}(\bar{n}s_{\text{ib}})/I_m(\bar{n}s_{\text{ib}}) - m/\bar{n}s_{\text{ib}} & \text{if } s = s_{\text{ib}}, \\ K_{m+1}(\bar{n})/K_m(\bar{n}) - m/\bar{n} & \text{if } s = 1. \end{cases} \tag{3.22}$$

(see Fearn, 1988). Here, I_m and K_m are modified Bessel functions [see Abramowitz & Stegun (1965), Ch. 9].

Since each boundary $s = s_{\rm ib}, 1$ is a perfect insulator, the normal component of current density j_s must vanish at those boundaries

$$j_s \equiv \frac{1}{s}\frac{\partial b_z}{\partial \phi} - \frac{\partial b_\phi}{\partial z} = 0 \quad \text{on } s = s_{\rm ib}, 1. \tag{3.23}$$

Upon using $\nabla \cdot \mathbf{b} = 0$, (3.21) and the expansions (3.18), (3.19) we can rewrite (3.23) in the form

$$[s + s^2 D + (\bar{n}^2 s^2 + m^2)/\gamma_n \bar{n}] b_{s,n} = 0 \qquad n \in [1, 2, ...) \tag{3.24}$$

on $s = s_{\rm ib}, 1$ and where $D \equiv {\rm d}/{\rm d}s$.

The differential order, in s, of our system has dropped from being tenth order to fourth order upon neglecting fluid inertia and viscosity and so the six boundary conditions (3.21), (3.24) and $v_s = 0$ associated with the curved annular surfaces cannot all be accommodated by the inviscid mainstream. However, Fearn (1983a) has shown that in the limit of vanishing viscosity $\nu \to 0$ the no-normal flow conditions are supported by the viscous boundary layers. There must be large flows in the viscous boundary layers since, wherever fluid flows into the layer, fluid must flow out elsewhere in order that mass be conserved. We do not concern ourselves with this boundary layer flow and solve for the mainstream flow only. In order to close our hydromagetic problem, we enforce the four boundary conditions (3.21), (3.24).

As explained in the introduction, we then enforce the nonlinear geostrophic flow V_G modified from its spherical representation (1.15) to the cylindrical form (1.17). We do not include the non-axisymmetric component of the geostrophic flow as this is not geophysically relevant and leads to a problem which is fully three dimensional and not so numerically tractable.

The perturbed flow and magnetic field are scaled with $E^{1/4}$ in order to remove the explicit appearance of the Ekman number from (3.13) and (3.14). Using the expansion functions (3.18), (3.19) we can write (1.17) in terms of the components of the perturbed field. This gives

$$V_G = (2^{1/2}\zeta)\Re\left\{(s^{-1} b_{s,n} + b_{s,n} D - \bar{n} b_{z,n}) b^*_{\phi,n}\right\} \tag{3.25}$$

which is equivalent to the form given for the geostrophic angular velocity $\Omega_G = V_G/s$ found by Skinner & Soward (1988, 1990). For a derivation of (3.25), see Appendix C. With V_G now given in its component form we can implement our numerical scheme.

3.3 Program Design, Implementation and Testing

3.3.1 Design

In the governing equations (3.13), (3.14) and (3.15) the ϕ- and z-dependences were separated and parametrised by their azimuthal and axial wavenumbers m and n, respectively. The radius was then split up into $N+1(=101)$ equally spaced grid points amenable to a (fourth-order) finite difference scheme in space. The discretized governing equations, reduced to 2 prognostic induction equations and two diagnostic momentum equations in the variables b_s, b_z, v_s and v_z, were then solved using a semi-implicit time stepping method utilising a Crank-Nicholson scheme for the diffusive terms and an Adams-Bashforth treatment for the remaining terms. The method of solution proceeded in the following manner:

(i) the perturbed magnetic field $\mathbf{b}$ was evolved using the prognostic induction equation (3.14),

(ii) the perturbed flow field $\mathbf{v}$ was evaluated explicitly from the diagnostic momentum equation (3.13),

(iii) the geostrophic flow was then computed via (3.25).

Step (i) reduced to solving a linear system which, as a result of the finite difference scheme, involved a system matrix which was pentadiagonal. Since the system matrix remained constant throughout any computational cycle the stability problem was solved using an LU-decomposition. The initial conditions for the instability were either arbitrarily chosen, taking the form of an impulse

$$b_{s,z}(s = i\Delta s) = \delta \quad \forall i = 0, 1, ..., N \tag{3.26}$$

at time $t = 0$ whose magnitude was modulated by δ [generally, $\delta = \mathrm{O}(0.001 - 0.1)$] or a previous solution was used as a starting point. When a such a previous solution $b^{(0)}_{s,z}$ was used, its amplitude was often stretched by a parameter Γ:

$$b_{s,z}(s = i\Delta s) = \Gamma b^{(0)}_{s,z} \quad \forall i = 0, 1, ..., N. \tag{3.27}$$

It was found that in many calculations for a chosen basic field and fixed m, n, the solution varied with increasing Λ by growing in amplitude but preserving the same

overall structure. Once a solution was known at moderate Λ, it was often possible at higher Λ to find a value $\Gamma > 1$ that gave an excellent approximation to the new solution. This process considerably reduced computational time.

Step (ii) involved explicitly evaluating the flow field at each of the radial node points and Step (iii) similarly required calculation of the geostrophic flow at each of those node points $s_0, ..., s_N$.

3.3.2 Measure

It is important to realise that when the field configuration is varied, the basic state energy budget will also vary. Let the energy of a vector valued function $\mathbf{f}^*$, defined over the annular volume $\mathcal{A}^*$, be

$$\frac{1}{\mathrm{Vol}^*(\mathcal{A}^*)} \int_{\mathcal{A}^*} \mathbf{f}^* \cdot \mathbf{f}^* \, \mathrm{d}V^* \tag{3.28}$$

where $\mathrm{Vol}^*(\mathcal{A}^*) = 2\zeta\pi(1 - s_{\mathrm{ib}}^2)s_o^3 = \mathrm{Vol}(\mathcal{A})s_o^3$ is the (dimensional) volume of the annulus $\mathcal{A}^*$. Here, starred variables represent dimensional quantities and unstarred variables represent non-dimensional quantities. The energy of the basic field $\mathbf{B}_0^* = B_M \mathbf{B}_0$ is then

$$E^*(\mathbf{B}_0^*) = \frac{1}{\mathrm{Vol}^*(\mathcal{A}^*)} \int_{\mathcal{A}^*} \mathbf{B}_0^* \cdot \mathbf{B}_0^* \, \mathrm{d}V^* = \frac{B_M^2}{\mathrm{Vol}(\mathcal{A})} \int_{\mathcal{A}} \mathbf{B}_0 \cdot \mathbf{B}_0 \, \mathrm{d}V = B_M^2 E(\mathbf{B}_0). \tag{3.29}$$

The energies associated with each field configuration are given in Table 3.1

TABLE 3.1: Dimensionless field energies $E(\mathbf{B}_0)$.

Basic Field Dependence, $F(s)$	Total Field Energy, $E(\mathbf{B}_0)$
(3.10)	0.299
(3.11)	0.267
(3.12)	0.105

Based on the total dimensional energy E^* of the basic field, let us define the "energetic Elsasser number" Λ' as

$$\Lambda' = \frac{E^*(\mathbf{B}_0^*)}{2\Omega_0\rho_0\mu\eta} = \frac{B_M^2}{2\Omega_0\rho_0\mu\eta} E(\mathbf{B}_0) = E(\mathbf{B}_0)\Lambda. \tag{3.30}$$

Although we quote our stability results in terms of Λ for consistency with the results of Fearn (1988), a redefinition of Λ in terms of the basic field energy $E(\mathbf{B}_0)$ facilitates

a realistic comparison between the different field configurations defined by (3.10), (3.11) and (3.12). To this end, results for the most unstable modes will also be tabulated in terms of Λ'. Note that Λ'_c values can be found from Λ_c upon using (3.30) and Table 3.1.

3.3.3 Implementation

The linear and nonlinear stability results were gathered in three stages. Firstly, critical parameter values Λ_c for the onset of magnetic instability were found for a variety of m and n by repeating only Steps (i) and (ii) of the scheme above (without calculating the geostrophic flow). The procedure for determining Λ_c required following the trend in magnetic energy $E(\mathbf{b})$ and observing the growth rate of the field. In order to calculate the complex growth rate, $\lambda = \sigma + i\omega$, we use a Taylor series. Suppose that b represents any of the components of the perturbed magnetic field. For the linear problem, we may write $b = b_0(s)e^{-i\lambda t}$ and obtain our eigenvalue λ upon observing that $-i\lambda = b^{-1}\mathrm{d}b/\mathrm{d}t$ and then using a Taylor series truncated at $\mathrm{O}(\Delta t)^2$ to approximate $\mathrm{d}b/\mathrm{d}t$. Then, for $\Delta t \ll 1$

$$\lambda = \frac{i}{\Delta t}\left[\frac{b(t_{i+1})}{b(t_i)} - 1\right]. \tag{3.31}$$

In the second stage, and after the critical values of Λ had been found, the geostrophic profile was computed once [using (3.25)] from the linear eigensolution at $\Lambda = \Lambda_c$. After being modulated to have a maximum amplitude of unity, this structure, $V_G^{(0)}$, was then imposed as the (steady) differential rotation

$$\mathbf{V}_0 = \mathcal{R}_m V_G^{(0)} \mathbf{1}_\phi \,. \tag{3.32}$$

For infinitesimal values $0 < \mathcal{R}_m \ll 1$ and amplitudes of the perturbed field close to Λ_c this differential rotation coincides arbitrarily closely with the geostrophic flow. Thus, for small values of $\mathcal{R}_m$ and Λ close to Λ_c [i.e. on a neighbourhood of $(\mathcal{R}_m, \Lambda_c)$] we can expect the behaviour of the geostrophic flow to be reproduced by (3.32). Enforcing the geostrophic structure as a differential rotation at $\Lambda = \Lambda_c$ successfully identified the sub/supercritical nature of the magnetic instability.

In the final stage, the geostrophic flow was dynamically updated at every time step and the equilibrated solution $(\mathbf{b}, \mathbf{v}, V_G)$ found as a function of Λ. The

geostrophic flow has the potential to quench the exponential growth of linear eigensolutions. If $||\mathbf{b}||$ was seen to converge with the growth rate of the field tending to zero, the solution was said to have become equilibrated in an Ekman state. At that point, the frequency, field and geostrophic amplitudes were noted. This allowed us to plot the stable Ekman branch bifurcating from its linear critical value.

When no stable solutions were found, it was possible to track the unstable Ekman branch by varying δ in (3.26) or Γ in (3.27). By examining the trend in growth rate and field amplitude, it was possible to determine values $\delta = \delta_c(\Lambda)$ or $\Gamma = \Gamma_c(\Lambda)$ above which field growth was slightly positive and below which, field growth was slightly negative (typically, $\pm 10^{-5}$, respectively). As the example in Figure 3.10(a) typifies, careful choice of Γ led to a separation of the timescales over which initial transient features decayed and exponential growth/decay ensued. We found that the transient features completely vanished after the first slow dynamo timescale in any calculation. Use of the logarithmic scale for time in Figure 3.10(a) and good upper and lower bounds for Γ_c showed that exponential growth or decay could be delayed almost indefinitely (but limited by numerical precision). This made it possible to sandwich the structure and amplitude of the singular, unstable Ekman solution between marginal growth and marginal decay. The computations were carried out beginning with either arbitrary initial data (3.26) or, as illustrated by example in Figure 3.10(a), upon using the modulated linear eigenfunction found at $\Lambda = \Lambda_c$, (3.27). After a number of slow timescales had passed (typically 100), solutions showing very small growth were indistinguishable from solutions showing very small decay [corresponding to "I" and "II", respectively, in Figure 3.10(a)]. Both types of initial condition, i.e. either (3.26) or (3.27), gave the same solution; the only difference being that the initial transient features were stronger in amplitude when arbitrary initial data was used.

3.3.4 Testing

We tested our numerical code in two ways: firstly, we investigated a linear problem with a prescribed differential rotation; and secondly, we checked our nonlinear code against the work of FLMO.

In the linear part of our testing, we imposed a differential rotation $V_0(s) = s\Omega(s)$

and time evolved our solution. For the choice $n = 3$ and $m = 2$ we investigated the differential rotation

$$\Omega(s) = -\mathcal{R}_m s^2 \tag{3.33}$$

with basic field given in (3.10). Here $\mathcal{R}_m = V_M \tau_s / s_o = R_m / \Lambda$ is the modified magnetic Reynolds' number and V_M is the maximum amplitude of our velocity field. Fearn (1988) found, using an eigenvalue analysis, that the critical onset of instability in the absence of differential rotation ($\mathcal{R}_m = 0$) occurred at $\Lambda_c = 28.9$ with eigenvalue $\omega_c = 0.160$. Our results are in good agreement with this: $\Lambda_c = 28.9$ and $\omega_c = 0.159$.

For the same problem, FLMO considered $\mathcal{R}_m > 0$ and obtained the critical curve for the onset of linear instability. This may be compared with our results in Figure 3.2.

We checked the nonlinear part of our program with the corresponding results of FLMO by comparing our geostrophic profiles generated by the $m = 2$, $n = 3$ mode and for the imposed fields given by setting $\alpha = 1, 2, 3$ and 4 in (3.10). Here, we computed the geostrophic structures obtained from the linear eigenfunctions at the onset of instability ($\Lambda = \Lambda_c$). Excellent agreement was found with FLMO (see their Figure 5) and the geostrophic flow profiles are shown in Figure 3.2.

3.4 Results

Further to the results of Fearn (1988) and FLMO, in Tables 3.2 and 3.3 we have tabulated the critical parameter values for the basic fields given by (3.10) and (3.11) along with their associated critical frequencies ω_c. In Table 3.4, we show the results for the basic field given in (3.12).

TABLE 3.2: Λ_c and ω_c (italicised) parameter values for the basic field (3.10).

	$n=1$		$n=2$		$n=3$		$n=4$	
$m=1$	5.950	*-1.031*	20.89	*-1.049*	58.00	*-1.182*	73.52	*-1.259*
$m=2$	4.394	*-.1328*	11.78	*-.0516*	28.94	*.1594*	71.47	*.4223*
$m=3$	8.744	*2.063*	19.49	*1.956*	36.33	*1.831*	64.68	*1.699*
$m=4$	27.28	*2.544*	57.73	*2.442*	96.17	*2.287*	146.0	*2.110*

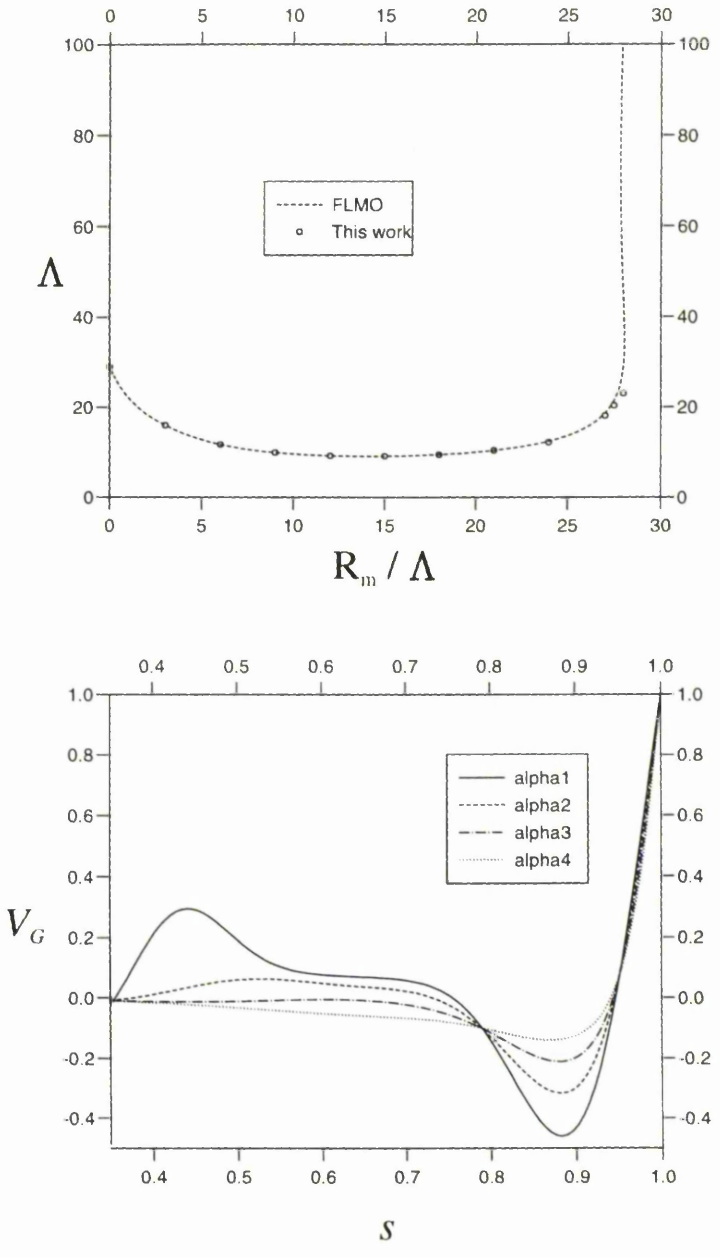

Figure 3.2: (i) Top: the neutral stability curve with imposed differential rotation $\Omega = -\mathcal{R}_m s^2$ and parameters (3.10), $m = 2$, $n = 3$. The circles are from our calculations and the dotted line from FLMO. (ii) Bottom: V_G that should be compared with Figure 5 of FLMO. Values of $\alpha = 1, 2, 3$ and 4 have been substituted in place of the superscript "4" in (3.11) at $\Lambda = \Lambda_c(\alpha)$ with $m = 2$ and $n = 3$.

TABLE 3.3: As Table 3.2 but for the basic field (3.11).

	$n=1$		$n=2$		$n=3$		$n=4$	
$m=1$	4.652	*-1.024*	10.10	*-1.036*	16.37	*-1.043*	23.69	*-1.050*
$m=2$	2.308	*-.8122*	5.146	*-.8828*	9.160	*-.8970*	15.05	*-.8497*
$m=3$	1.876	*1.198*	4.082	*1.137*	7.083	*1.187*	11.34	*1.350*
$m=4$	1.959	*5.372*	4.108	*5.209*	6.742	*5.060*	10.19	*4.995*

TABLE 3.4: As Table 3.2 but for the basic field (3.12).

	$n=1$		$n=2$		$n=3$	
$m=1$	7.775	*-1.202*	27.64	*-1.711*	47.49	*-1.872*
$m=2$	6.919	*-1.159*	52.94	*-2.599*	>60	–
$m=3$	>60	–	>60	–	>60	–

Comparing Tables 3.2, 3.3 and 3.4 it would appear that, in every case of m and n, the imposed field (3.11) is more unstable than (3.10), which is in turn more unstable than (3.12). This comparison may be misleading, however, as the three different fields each have different basic field energies $E(\mathbf{B}_0)$ associated with them (see Table 3.1). Table 3.5 shows a selection of the most unstable modes (i.e. those for which $n=1$) across the different fields.

TABLE 3.5: Λ_c' values for the basic fields (3.10)–(3.12).

$F(s)$	$m=1$	$m=2$	$m=3$	$m=4$
(3.11)	1.392	.6909	.5615	.5864
(3.10)	1.589	1.174	2.336	7.288
(3.12)	.8138	.7242	>6.5	>6.5

Table 3.5 shows that the field (3.11) concentrating near the CMB is the most unstable field. As instability tends to form around where the basic field is strongest, we expect field which concentrates to the ICB to become more stable (diffusion is more effective on instabilities forming over shorter lengthscales). This stabilising effect is observed in field (3.12) for modes $m>2$. For the modes $m=1$ and $m=2$, diffusion is not so effective and as all the energy from the basic field is concentrated over a smaller volume, field (3.12) is more unstable than (3.10).

The linear eigenfunctions at linear onset from the most unstable modes in each of fields (3.11) and (3.12) can be found in Figures 3.3 and 3.4, respectively. The associated geostrophic flows are shown in Figure 3.5 where they may be compared along with the geostrophic profile from the most unstable mode under field (3.10).

Using the method of imposing the structure of the geostrophic flow at $\Lambda = \Lambda_c$ as a differential rotation (3.32), it was found that the most unstable mode, for each n in Table 3.2, was of the subcritical class. As explained in Section A.1, consideration of the most unstable mode in each of $n = 1, 2, 3$ and 4 is equivalent to considering the most unstable mode for the annular half-heights $\zeta = \pi/2$, $\pi/4$, $\pi/6$ and $\pi/8$, respectively. Further to the work of FLMO, we have found that for the field (3.10) and for every case of ζ considered, the geostrophic flow reduced Λ_c for the most unstable mode. In contrast to this, the field (3.11) produced only supercritical results for the most unstable mode irrespective of the annular half-height. The field (3.12) produced a mixture of sub- and supercritical bifurcations. The most unstable mode ($m = 2$, $n = 3$) was of the subcritical class under an aspect ratio of $1 : \pi/2$. Upon reducing ζ to $\pi/4$ and then to $\pi/6$ the most unstable modes ($m = 1$, $n = 2$ and then $m = 1$, $n = 3$, respectively, on Table 3.4) became supercritical in nature.

From Figure 3.5 we found a tendency for V_G to concentrate where the basic field was strongest. This is not immediately obvious as V_G depends on the basic field implicitly through $\mathbf{b}$ in (3.25). It is apparent, from Figure 3.5(b), that the geostrophic flow associated with the supercritical instability of the field (3.11) with $m = 3$ and $n = 1$ contains only modest negative outward gradient compared with Figures 3.5(a) or (c). The eigenfunction (see Figure 3.3) shows field concentration close to the CMB leaving negligible field in the remainder of the annular gap. This leads to geostrophic flow which is likewise concentrated near the CMB with little chance for negative outward gradient which FLMO have shown to be a common feature of subcritical instability.

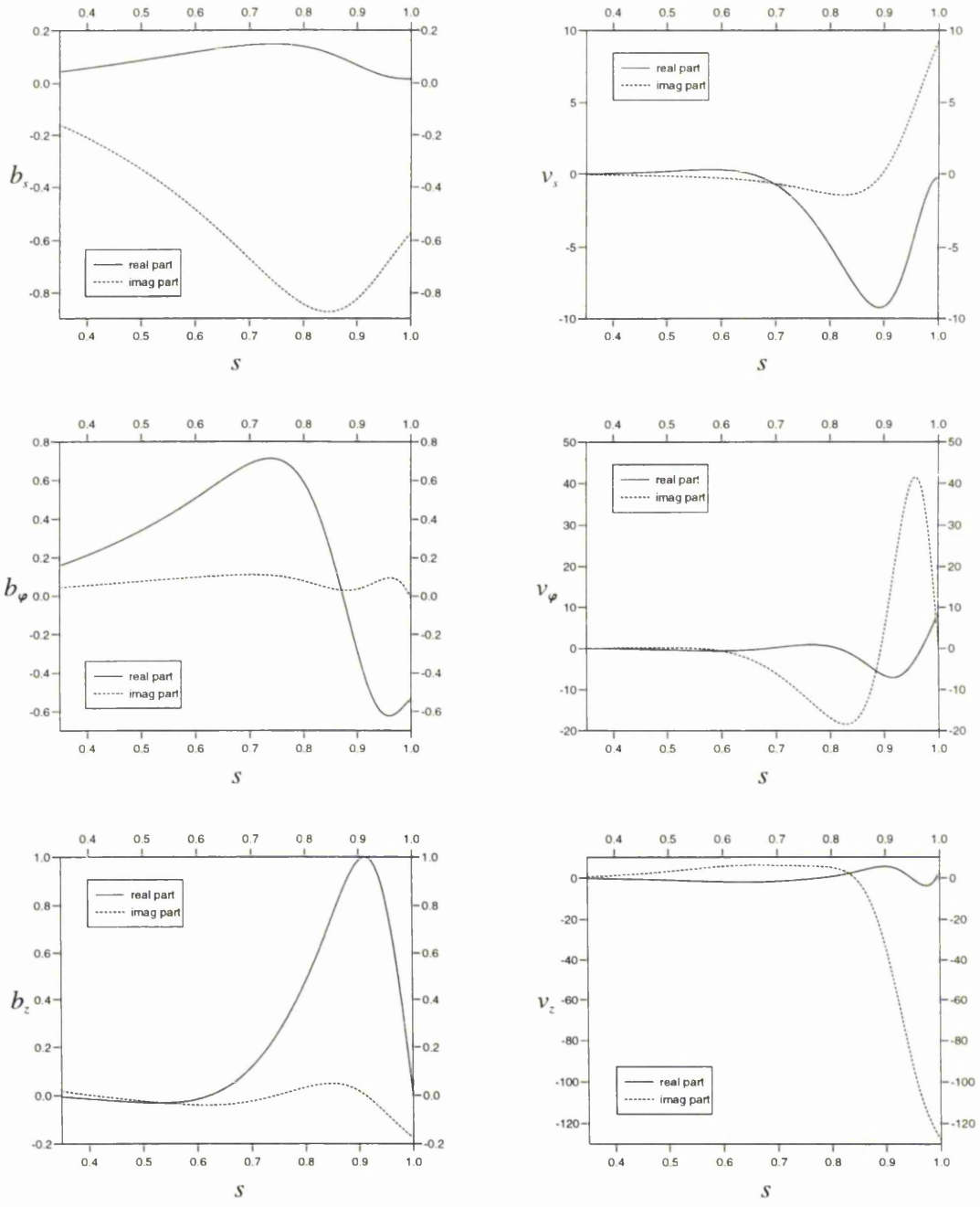

Figure 3.3: The linear eigenfunctions at $\Lambda_c = 1.876$ for the most unstable mode $(m = 3, n = 1)$ under the basic field (3.11) which concentrates field to the CMB (see Figure 3.1(b)). The critical frequency $\omega_c = 1.198$.

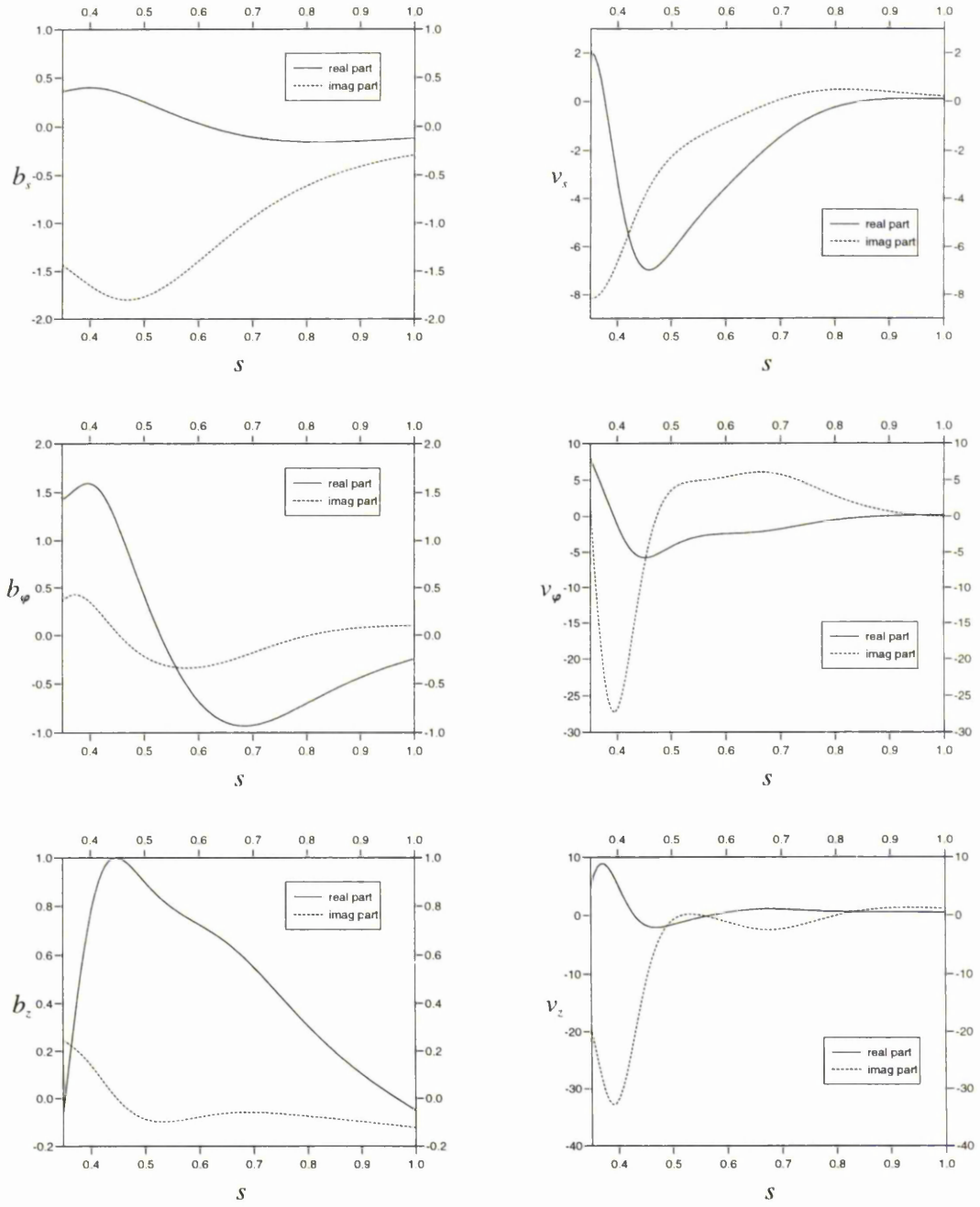

Figure 3.4: The linear eigenfunctions at $\Lambda_c = 6.919$ for the most unstable mode ($m = 2$, $n = 1$) under the basic field (3.12) which concentrates field to the ICB (see Figure 3.1(c)). The critical frequency $\omega_c = -1.159$.

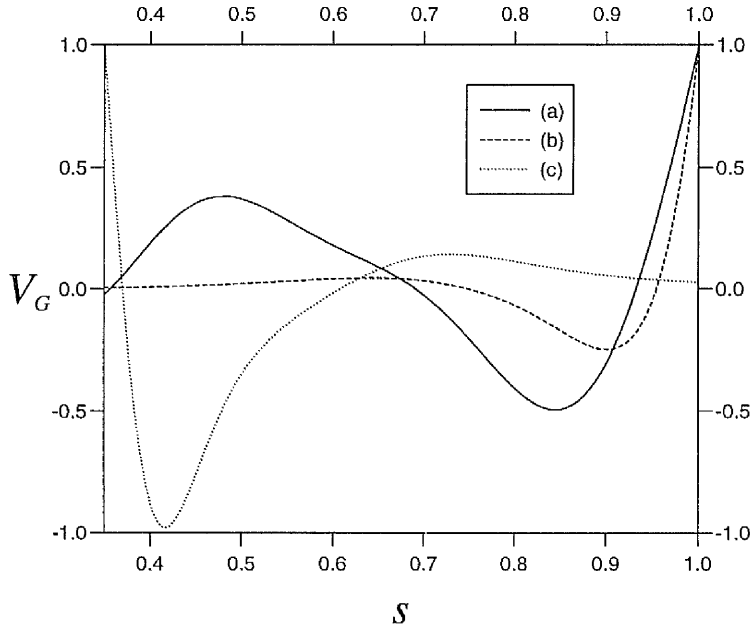

Figure 3.5: Corresponding to (a),(b) and (c) in Figure 3.1, profiles of V_G at $\Lambda = \Lambda_c$ for each of the most unstable modes from the fields (3.10), (3.11) and (3.12), respectively. Observe how V_G concentrates where the basic field is strongest.

In the remainder of this section we focus on the nonlinear development of two particular examples from Tables 3.2 and 3.3 above. We consider the two most unstable modes from the fields (3.10) and (3.11): firstly, we examine the supercritical example $m = 3$, $n = 1$ from field (3.11) [on Table 3.3]; and secondly, we investigate the subcritical example $m = 2$, $n = 1$ from field (3.10) [on Table 3.2]. In each case, ζ is considered fixed at $\pi/2$.

3.4.1 Supercritical Case

Under the basic field defined by (3.11) the onset of instability for the most unstable mode ($m = 3$, $n = 1$) case occurs at $\Lambda_c = 1.876$ with an associated frequency of -1.198. We begin by investigating the effect the geostrophic flow has by imposing its structure as a differential rotation in a linear problem and modulated by the modified magnetic Reynolds' number $\mathcal{R}_m$. Figure 3.6 shows that for small values of $\mathcal{R}_m$ (typically 10^{-3}) $\mathbf{V}_0$ stabilises the system. Therefore, in the nonlinear problem,

the dynamics of the geostrophic flow will have a stabilising effect. Also plotted on Figure 3.6 is the trend for the frequency.

In the nonlinear calculation, where the geostrophic flow is dynamically determined at each time step, Figure 3.7(a) shows the trends of the field and geostrophic amplitudes against time at $\Lambda = 1.885$. One immediately sees the effect the geostrophic flow has on an initially exponentially growing solution. As the field amplitude increases, so does the geostrophic flow, until, eventually, after 500 slow timescales, the field growth is almost completely quenched. The frequency of the instability has converged to 1.260 and the geostrophic flow has attained a steady profile with time. It is well worth noting that the geostrophic flow and the field structure do not appreciably change over the period of equilibration. The z-component of the equilibrated field is reproduced in Figure 3.7(b). Although the nonlinear problem contains an amplitude as part of its solution, b_z in Figure 3.7(b) has been normalised so that the maximum modulus is unity and the value of this maximum modulus stated. This was done to focus on the underlying structure rather than reproduce a snapshot of a rapidly vacillating solution.

While Figure 3.7 shows one computational run, Figure 3.8 summarises several similar runs. Here, we have varied Λ from its critical value of 1.876 to 1.894. Figure 3.8(a) shows the equilibrated amplitudes of $\mathbf{b}$ and V_G where each bullet/circle point represents one computational run and the results have been interpolated linearly for clarity. For values of Λ close to 1.876 the field and geostrophic flow grow sharply from zero and their profiles with Λ are concave down. However, at around $\Lambda = 1.884$, the field amplitude undergoes an inflexion and begins to increase more and more rapidly. The geostrophic flow undergoes no such change and maintains a concave down profile. This is indicative of an increasing amount of internal cancellation in the Taylor integral [see lhs of (1.13)] since otherwise, the geostrophic flow would grow in proportion to the square of the field. For high values of Λ this is clearly not the case and it should come as no surprise that calculations become more and more stiff as Λ was set to higher and higher values. Figure 3.6 shows how the structure of the geostrophic flow changes between values of $\Lambda = \Lambda_c = 1.876$ and $\Lambda = 1.894$. The maximum amplitude of V_G grows to 5.894 whilst the change is the geostrophic profile is more subtle.

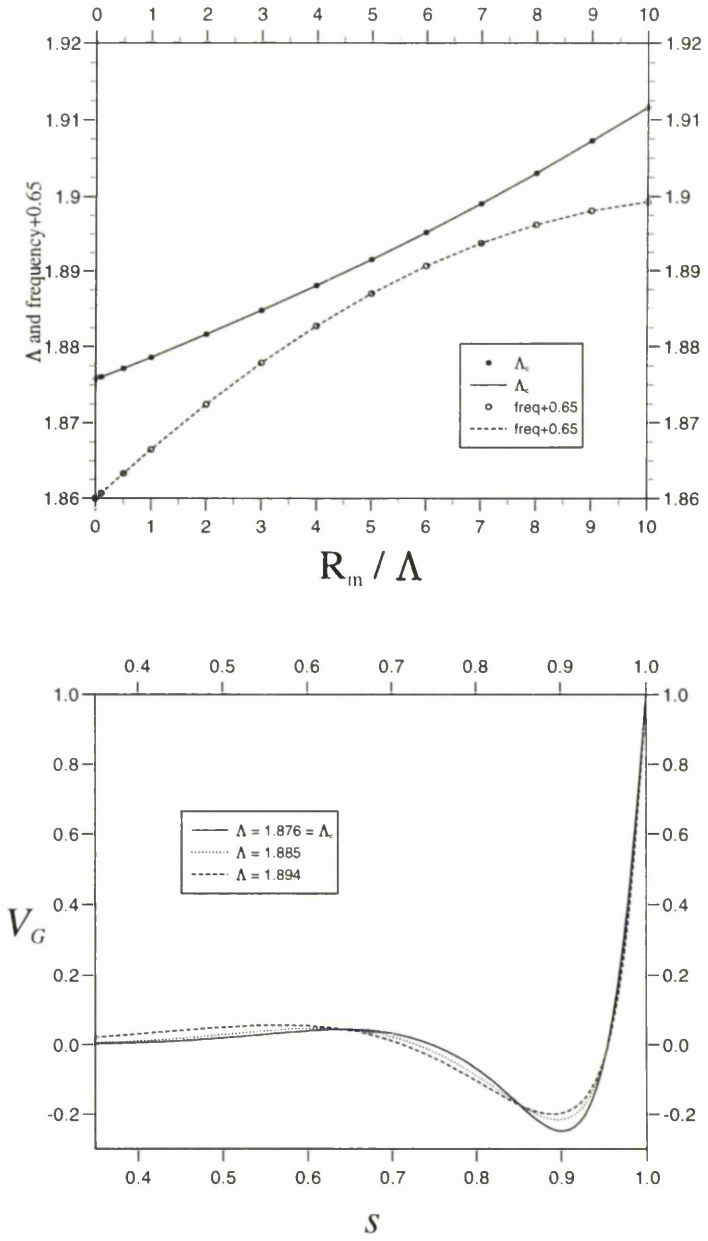

Figure 3.6: For the basic field (3.11) and $m = 3$, $n = 1$, (a) Top figure: critical curve (full line) including the geostrophic structure at $\Lambda = \Lambda_c$ as a differential rotation (3.32) (frequency shown dashed). (b) Bottom figure: V_G taken at $\Lambda = \Lambda_c$, 1.885 (scaled by 3.082) and at $\Lambda = 1.894$ (scaled by 5.894). V_G has been normalised so that $|\max_{s\in[s_{\rm ib},1]} V_G^2| = 1$.

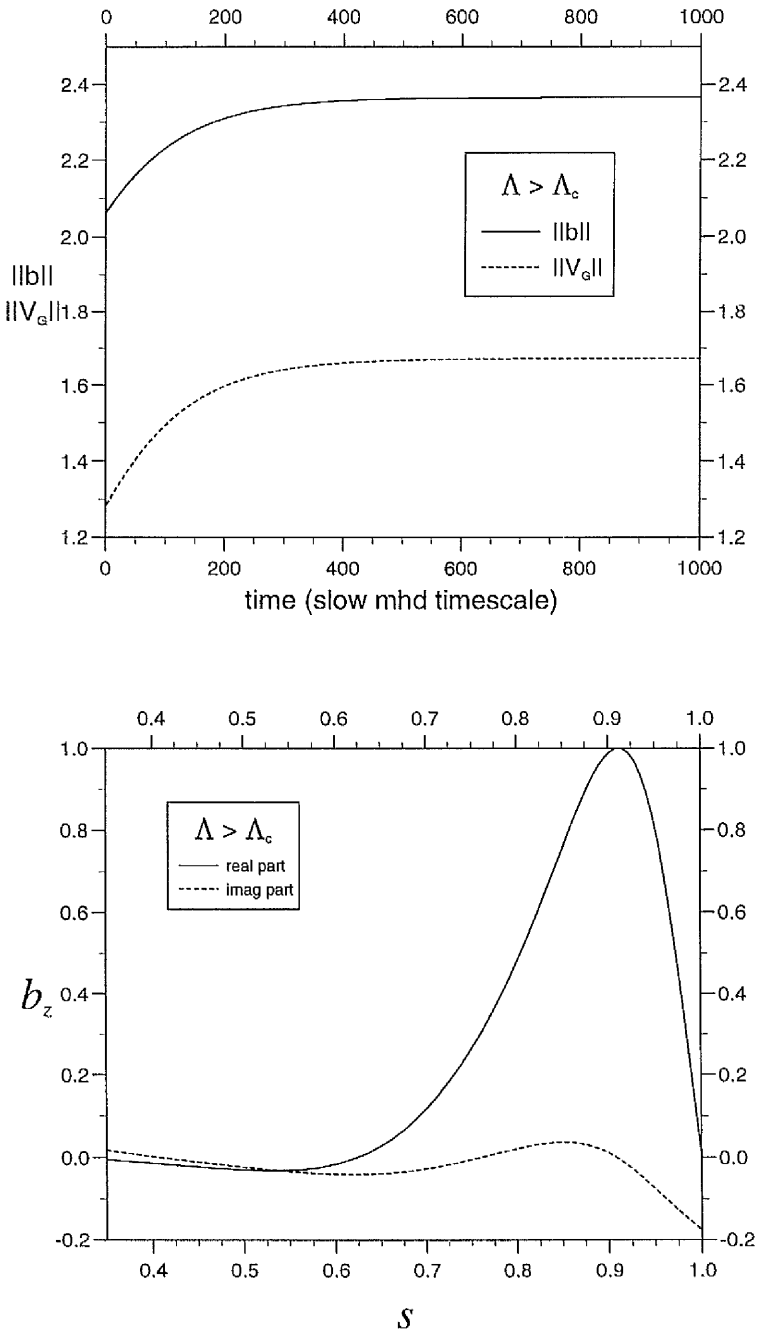

Figure 3.7: For the case $\Lambda = 1.885$, with field (3.11), $m = 3$ and $n = 1$, (a) Top figure: the trends of $||\mathbf{b}|| \equiv E(\mathbf{B}_0)^{1/2}$ and $||V_G|| \equiv E(V_G \mathbf{1}_\phi)^{1/2}$; (b) Bottom figure: the solution b_z normalised by 0.8217.

We stress that all results here lie in the Ekman regime although we have shown an increased amount of internal cancellation in the Taylor integral suggestive of a progression towards a Taylor state. The trend for the field in Figure 3.8(a) is in good agreement with the trend proposed by Malkus & Proctor (1975) for the progression from infinitesimal field amplitudes through Ekman states towards Taylor states. Figure 3.8(b) shows the corresponding (converged) frequencies of the equilibrated fields as Λ is increased. Observe that at first, the frequency increases linearly with Λ. As more and more internal cancellation begins to occur in the Taylor integral and we approach higher values of Λ, the frequency begins to level off (near $\Lambda \cong 1.891$). This feature has been observed by Ogden (1997) in a similar nonlinear stability calculation including the geostrophic flow. There the instabilities were driven by thermal buoyancy forces rather than by energy from the magnetic basic state.

3.4.2 Subcritical Case

In the second of two examples, we consider the basic field (3.10) and where $m = 2$, $n = 1$. This mode is the most unstable mode for the basic field (3.10). The critical parameter value is $\Lambda_c = 4.394$ with corresponding frequency -0.1328.

By computing the linear eigenfunction at $\Lambda = \Lambda_c$ we may use (3.25) to determine the corresponding geostrophic structure $V_G^{(0)}(s)$. We normalise the geostrophic profile to have a maximum amplitude of unity and, as in Section 3.4.1, we begin by considering the purely linear problem with an imposed differential rotation $\mathbf{V}_0 = \mathcal{R}_m V_G^{(0)}(s)\mathbf{1}_\phi$. The geostrophic profile V_G used is identical to that shown as dashed in Figure 3.9(b). For small values of the magnetic Reynolds' number, $\mathcal{R}_m = 10^{-3}$, we find that the geostrophic flow has a destabilising effect on the system. Having established the destabilising effect of this differential rotation, it is worth observing that as $\mathcal{R}_m$ is increased, the critical curve reaches a minimum at $\mathcal{R}_m = 7$ and $\Lambda_c = 4.029$. From this point, Λ_c increases, passing through $\Lambda = 4.394$ at $\mathcal{R}_m = 12$ after which it has a stabilising effect on the system. The frequency, also plotted on Figure 3.9(a), exhibits a roughly linear, decreasing trend from 0.1330 at $\mathcal{R}_m = 0$.

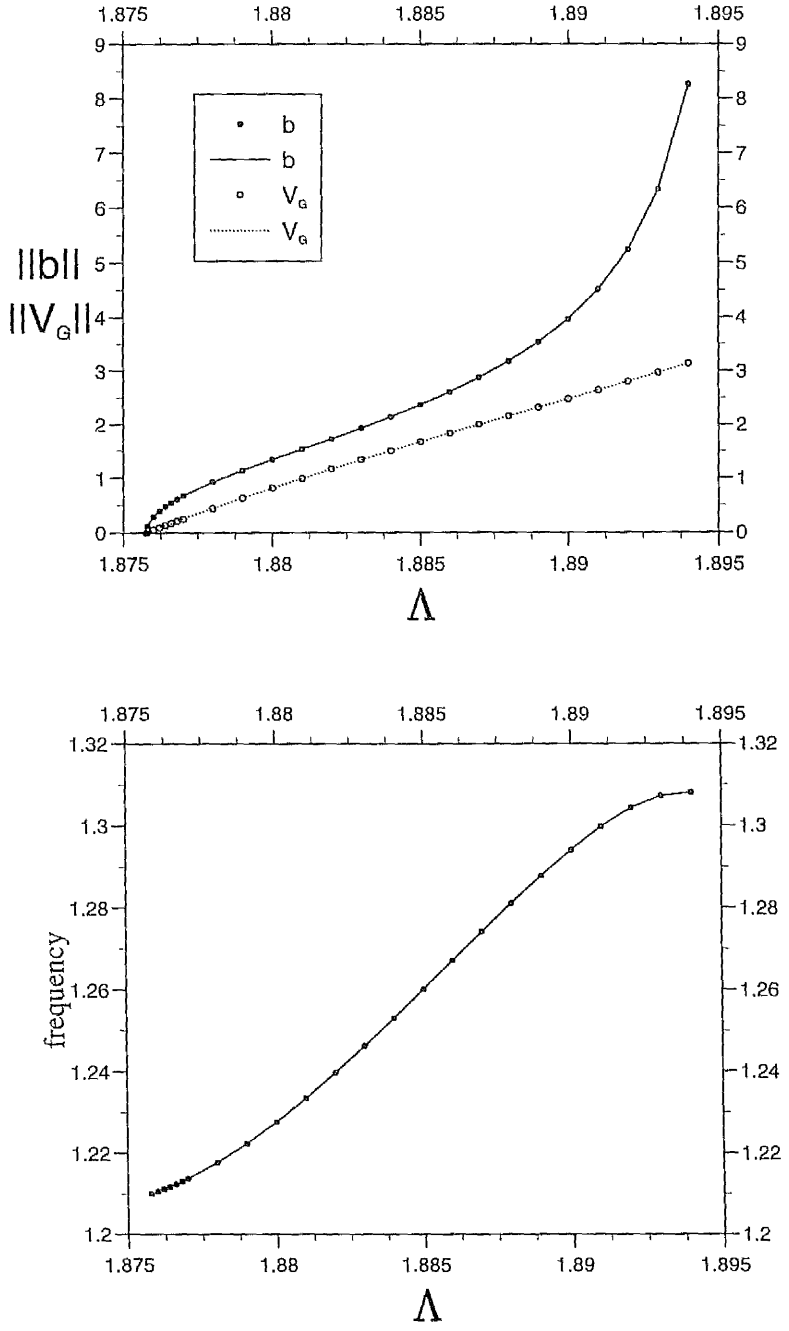

Figure 3.8: For the field (3.11) $m = 3$ and $n = 1$, (a) Top figure: equilibrated field (full line) and V_G amplitudes (dotted line); (b) Bottom figure: the corresponding trend for the frequencies in (a). Bullets/circles indicate computational runs which are interpolated linearly for clarity.

Figure 3.9(b) shows the geostrophic profiles at $\Lambda = \Lambda_c = 4.394$, $\Lambda = 4.375$ and $\Lambda = 4.355$. As seen from Figure 3.11(a), $||V_G||$ greatly increased from infinitesimal amplitudes at $\Lambda = \Lambda_c$ to O(1) values at $\Lambda = 4.355$ whilst the underlying structure has changed only subtly, becoming smoother. In accord with FLMO who showed that large outward negative gradients of differential rotation $V(s)$ could reduce the onset of instability, we find a large region negative gradient of V_G for $s \in (0.5, 0.85)$ (see Figure 3.9) which leads to subcriticality.

As one would expect, the Ekman branch bifurcating from Λ_c was found to be an unstable branch. For $\Lambda < \Lambda_c$ and any value of δ (or Γ) in excess of some critical value δ_c (or Γ_c), the resulting solution suffered exponential growth and for any smaller value, exponential decay. In Figure 3.10(a) we set $\Lambda = 4.375$ and by taking the critical linear eigenfunction modulated by a stretching parameter Γ as initial conditions, then using Section 3.3.3, we were able to determine the structure and amplitude of the singular Ekman solution on the unstable branch. As can be seen from Figure 3.10(a), transient features decayed over the period of one timescale after which we were able to bound the marginal Ekman state between very small growth and very small decay. (Refer to Section 3.3.3 for a more detailed explanation.) The solution for b_z is reproduced in Figure 3.10(b) (normalised by 0.2590 so that the maximum modulus of b_z has amplitude one).

Figure 3.11(a) represents a number of computational runs which collectively allowed us to track the subcritical (unstable) Ekman branch which bifurcates from the linear onset of instability at $\Lambda_c = 4.394$. We have plotted both the field amplitude and the geostrophic flow amplitude for a number of values of Λ ranging from 4.355 to 4.394. This was achieved as described above and in Section 3.3.3. The trend exhibited in Figure 3.11(a) is quite similar to that in Figure 3.8(a) but in the reverse direction. Here, the bifurcation curve separates the character of the solution and gives an idea of by how much Λ_c may be reduced and still get instability. We have not extended the diagram back further due to stiffness problems requiring a reduced time step but it does appear plausible that the critical parameter value may be reduced below $\Lambda = 4.35$.

Finally, in Figure 3.11(b) we have plotted the frequencies corresponding to the unstable Ekman states.

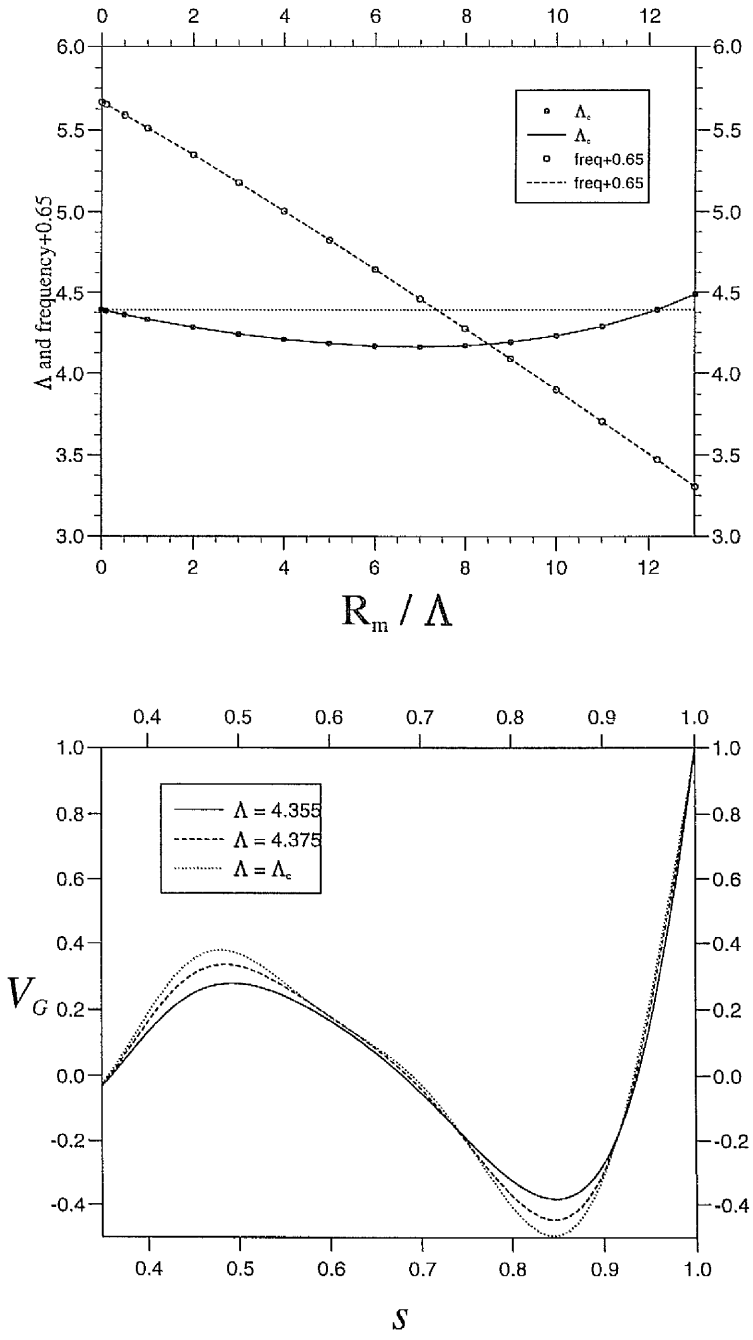

Figure 3.9: For the field (3.10) and $m = 2$, $n = 1$, (a) Top figure: same as for Figure 3.6(a); (b) Bottom figure: profiles of V_G at $\Lambda = \Lambda_c$ at 4.393 (dashed line) and at $\Lambda = 4.355$ (full line). Each profile has been scaled by 9.196×10^{-3} and 1.080, respectively, to give maximum amplitudes of unity.

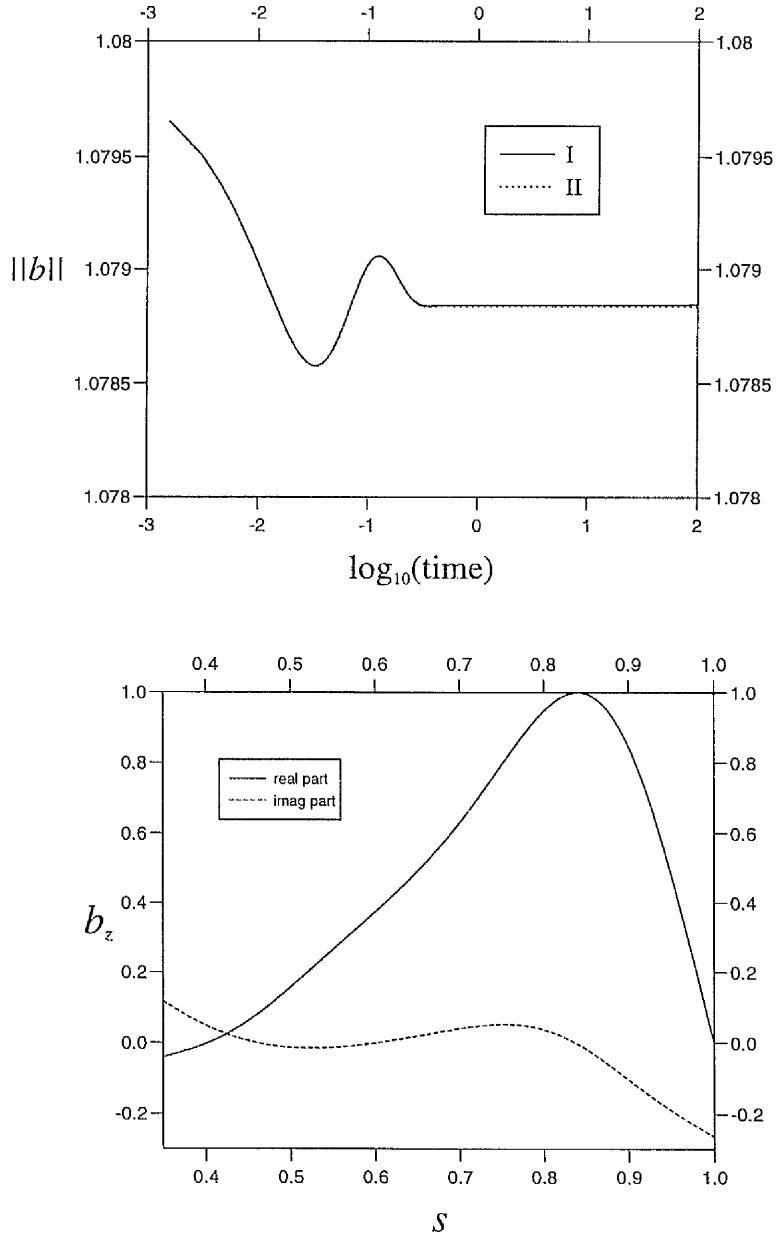

Figure 3.10: At $\Lambda = 4.375$, with field (3.10) and $m = 2$, $n = 1$: (a) Top figure: $||\mathbf{b}||$ versus $\log_{10}$(time). The eigenfunction at Λ_c, scaled by Γ, was used as the initial condition [see (3.27)]. "I" represents very slight growth of solution, and "II", very slight decay. (b) Bottom figure: the corresponding solution for b_z (scaled by 0.2590 as described).

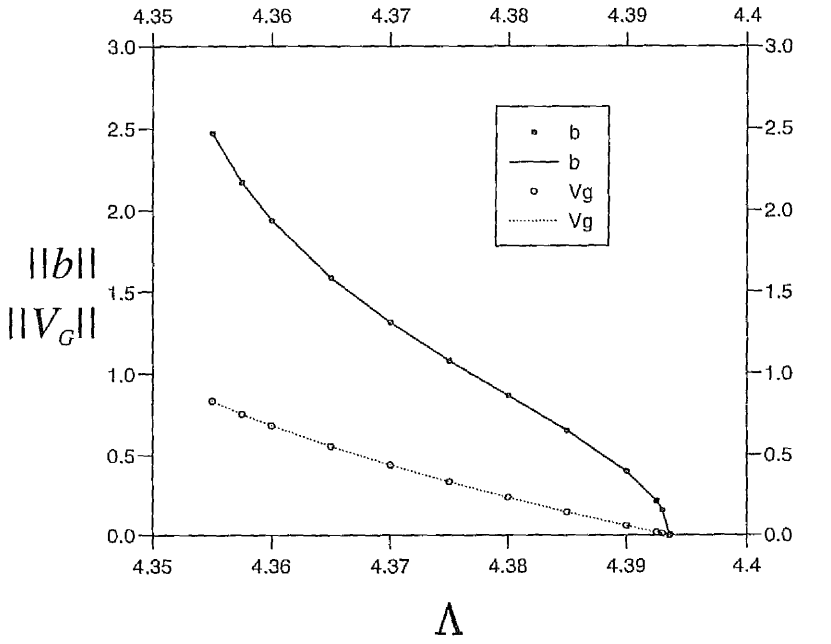

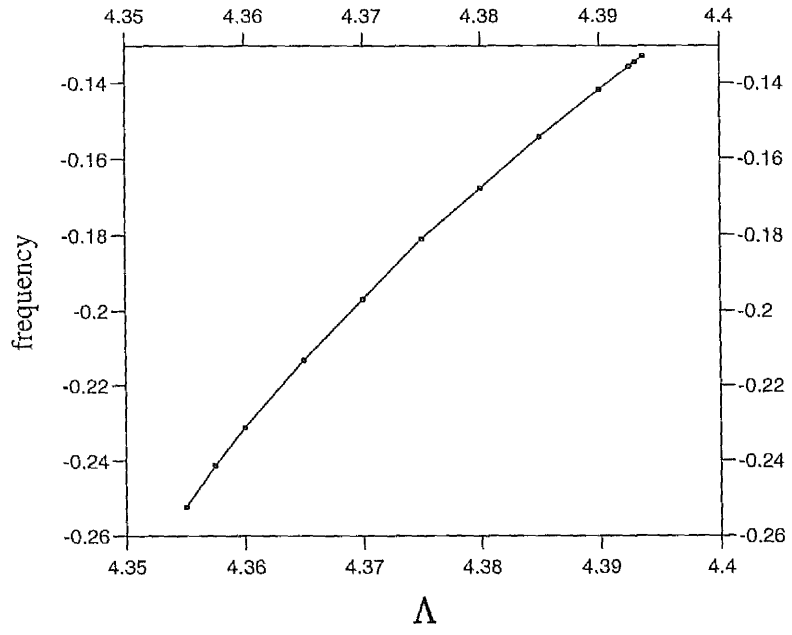

Figure 3.11: For the field (3.10) and $m = 2$, $n = 1$, (a) Top figure: the unstable, subcritical, Ekman branch; (b) Bottom figure: the corresponding frequencies. Bullets/circles indicate computational runs which have been interpolated linearly for clarity.

3.5 Remarks

In this chapter we discussed the stability of three different examples of radially dependent basic state. The configurations (3.11) and (3.12) each concentrated field to the CMB and to the ICB, respectively, whereas (3.10) concentrated to the middle of the annular gap. The field (3.12) has not been studied before and is new. In order to compare critical parameter values it was necessary to redefine the Elsasser number Λ in terms of the basic state energy. The stability results showed that the new field was unstable but not unstable as (3.11). Since magnetic instabilities tend to concentrate wherever the basic field is strongest, the limiting effects of diffusion damped all but the two lowest order azimuthal modes $m = 1$, 2 for (3.12).

The linear eigenfunction was used at marginal stability to construct a differential rotation with the structure of the geostrophic flow. This was then used to determine if an instability would follow a supercritical or subcritcial bifurcation into the nonlinear regime without actually having to compute in the nonlinear regime. The results showed that V_G could induce subcriticality for the most unstable mode in some instances. FLMO found that, when subcriticality occurred, it was accompanied by large negative gradients in the shear flow. We have shown examples that corroborate their finding.

We investigated the full nonlinear development of the most unstable modes from the basic states (3.11) and (3.10). The first lead to a stable Ekman state, consistent with a Malkus & Proctor (1975) type development for equilibrated field amplitude. The full Malkus & Proctor scenario could never be realised in our calculations as we were limited to the Ekman regime. However, a corresponding profile of $||V_G||$ showed that as Λ increased, $||\mathbf{b}||$ began to increase more and more rapidly whilst $||V_G||$ did not. This was indicative of internal cancellation occurring within the Taylor integral and of the approach to a state where, although we are always in the Ekman regime, Taylor's constraint is being more closely satisfied.

In a second example we found a way to obtain the unstable Ekman branch for the most unstable mode for the basic field configuration (3.10). This bifurcation diagram showed a similar profile to the Malkus & Proctor scenario when field amplitude was plotted against Λ. This time, however, the bifurcation curve moved off right to left from Λ_c.

One point which is worth noting is the small range in Λ covered by the Ekman state. For example, the bifurcation diagram in Figure 3.8 for the supercritical example shows considerable progression in the Ekman regime toward a Taylor state (where $\Lambda \geq \Lambda_T$) yet Λ has only varied between $\Lambda_c \cong 1.876$ and 1.894. Skinner & Soward (1990), investigating a magnetic stability problem driven by thermal buoyancy, found a similar result. Their modified Rayleigh number Ra [see Chapter 1, eq. (1.8)], was found to vary over a small parameter range in the nonlinear regime before approaching Ra_T. This similarity between thermal and magnetical instabilities is consistent with the result of Zhang (1993), i.e. both types of instability are part of the same mechanism.

A similar but viscous stability analysis completed by Hutcheson & Fearn (1995b) found no subcritical bifurcations. A possible explanation for the qualitative difference, discovered by FLMO, between viscous and magnetostrophic analyses in the cylindrical geometry is that the viscous analysis implicitly includes the non-axisymmetric component of the geostrophic flow. This work, along with all other magnetostrophic calculations in the past which used a cylindrical geometry, did not include the non-axisymmetric component of the geostrophic flow. It may be this difference, rather than a geophysically unrealistic Ekman number taken in the viscous calculations, that will eventually explain the qualitative difference.

Chapter 4

The Stability of Dipole and Quadrupole Fields

4.1 Introduction

With a view to assessing the stability of the geomagnetic field, we study the stability of s- and z-dependent axisymmetric field configurations to non-axisymmetric perturbations. As in the previous chapter, the cylindrical polar coordinate system (s, ϕ, z) is used. This work represents a natural progression from the stability analyses of Chapter 3 which considered only radially dependent basic fields. The addition of a z-dependence to the basic field configuration is geophysically realistic but it does lead to a more complicated problem formulation since the axial modes may no longer be considered in isolation as in the previous chapter. Now the presence of the independent variable z in the perturbation equations (3.11, 12, 13) couples the axial modes together and the problem becomes fully two-dimensional. As a result, extensive modifications have been made to the computer program so that it may accomodate a wider range of basic, toroidal fields.

Zhang & Fearn (1994) assessed the linear stability of toroidal field configurations in the spherical shell geometry. There, problems of resolution were encountered and the annular geometry is the logical alternative that is more tractable. Our magnetostrophic study complements the work of Hutcheson & Fearn (1995a,b, 1996, 1997) [hereafter referred to as HF1-4, respectively] who solved essentially the same problem but at a finite Ekman number. They did not use the magnetostrophic approx-

imation and included many other nonlinear interactions neglected in our analysis. HF1,2 considered the stability of radially dependent basic state fields which are best compared with results in Chapter 3 whereas HF3,4 examined s- and z-dependent basic (azimuthal) fields

$$\mathbf{B}_0 = sF(s)G(z)\mathbf{1}_\phi \tag{4.1}$$

which we consider in this chapter.

The radial dependencies are prescribed by the function $F(s)$ of which we examine two basic types

$$F(s) = [2/(1-s_{\rm ib}^\alpha)]^2(1-s^\alpha)(s^\alpha - s_{\rm ib}^\alpha) \tag{4.2}$$

$$F(s) = [2/(1-s_{\rm ib}^\alpha)]^2(1-(1+s_{\rm ib}-s)^\alpha)((1+s_{\rm ib}-s)^\alpha - s_{\rm ib}^\alpha). \tag{4.3}$$

and a value of $\alpha = 4$ is used in this chapter.

The function $G(z)$ contains the z-dependence of the basic field. Therefore, the z-independent fields of Chapter 3 correspond to taking $G(z) = 1$. In this chapter G is varied to give either equatorially symmetric or antisymmetric field symmetries about the equator $z = 0$. Using the nomenclature of Gubbins & Zhang (1993), a scalar function $\psi \in E^S$ if $\psi(s,\phi,-z) = \psi(s,\phi,z)$ and $\psi \in E^A$ whenever $\psi(s,\phi,-z) = -\psi(s,\phi,z)$. For a vector quantity, the description is a little more involved. A vector function $\mathbf{\Psi} = (\psi_s, \psi_\phi, \psi_z)$ is equatorially symmetric if, in terms of its components,

$$\psi_s, \psi_\phi \in E^S \text{ and } \psi_z \in E^A \tag{4.4}$$

and is said to be equatorially antisymmetric if

$$\psi_s, \psi_\phi \in E^A \text{ and } \psi_z \in E^S\,. \tag{4.5}$$

The types of basic fields examined, which all satisfy the magnetic boundary conditions on $z = \pm\zeta$ and $s = s_{\rm ib}, 1$, can be categorised by their symmetry about the equator. We consider both equatorially symmetric and antisymmetric field dependencies contained in the function $G(z)$:

$$G(z) = \cos\frac{\pi}{2\zeta}(z+\zeta), \tag{4.6}$$

$$G(z) = \cos\frac{\pi}{\zeta}(z+\zeta). \tag{4.7}$$

The E^A basic field, when accompanied by its associated E^S magnetic wind [see below, (4.11)] is certainly consistent with a dynamo mechanism of the $\alpha\omega$-type.

There, a large zonal differential rotation (likely to be a symmetric, thermal wind) winds lines of force about the inner core resulting in an antisymmetric field configuration. This argument certainly seems simplistic in the light of recent dynamo calculations [see, e.g., Glatzmaier & Roberts (1995a,b)] which show that field and flow structures interior to the core are highly complex and do not clearly indicate E^A or E^S preferences. It should be noted that although we use pure dipole or pure quadrupole basic fields here, our problem has been formulated so that *any* basic field may be considered.

The magnetic stability problem that we formulate is governed by the set of non-axisymmetric equations (3.13, 3.14, 3.15) which have been separated from their axisymmetric parts [see, for example, Fearn (1997)]. We then prescribe the mean magnetic field as a basic state $\mathbf{B}_0$. In general, the mean field takes the form

$$\bar{\mathbf{B}} = B_0 \mathbf{1}_\phi + \nabla \times (A \mathbf{1}_\phi) \tag{4.8}$$

where $B_0(s,z)$ is the toroidal field and $A(s,z)$ is the poloidal scalar. Although we do not prescribe A, it can be generated from the ϕ component of the mean electromotive force (see Appendix D). In the Ekman regime $A = \mathrm{O}(E^{1/2})$ and so its effect may be ignored in the non-axisymmetric equations [since the instabilities are of $\mathrm{O}(E^{1/4})$]. However, A makes an O(1) contribution to V_G. We have not included the effect of A in our geostrophic flow since a similar analysis to ours but in a sphere (Fearn, Proctor & Sellar, 1994) showed that the effect of A in the geostrophic flow was negligible. Future work is planned that will include the effect of A in the geostrophic flow.

In general, any basic field $\mathbf{B}_0$ that is at least a function of both the radial and axial coordinates will drive a magnetic wind $\mathbf{V}_M$. This can be seen from the curl and azimuthal average of the momentum equation (1.11):

$$\frac{\partial \mathbf{V}}{\partial z} = -\nabla \times [(\nabla \times \mathbf{B}) \times \mathbf{B}] \tag{4.9}$$

where $\mathbf{B}$ is the axisymmetric part from the sum of the basic field $\mathbf{B}_0$ and perturbed field $\mathbf{b}$. The solution for the flow, as already seen in the previous chapter, is the sum of the magnetic wind $\mathbf{V}_M$ and geostrophic flow $V_G \mathbf{1}_\phi$. Here

$$\mathbf{V}_M = \int_z^\zeta \nabla \times [(\nabla \times \mathbf{B}) \times \mathbf{B}] \, \mathrm{d}z' \tag{4.10}$$

and $V_G\mathbf{1}_\phi$ is given in Chapter 3. Now, the contribution to $\mathbf{V}_M$ from $\mathbf{b}$ is of $O(E^{1/4})$ and may be neglected in an order analysis. After some computation

$$\nabla \times [(\nabla \times \mathbf{B}_0) \times \mathbf{B}_0] = -\frac{\partial}{\partial z}\left(\frac{B^2}{s}\right)\mathbf{1}_\phi .$$

Thus

$$\begin{aligned} \mathbf{V}_M &= -\left[s^{-1}B^2\right]_z^\zeta \mathbf{1}_\phi \\ &= s^{-1}\{B^2(s,z) - B^2(s,\zeta)\}\mathbf{1}_\phi \end{aligned}$$

and if G takes one of the forms (4.6) or (4.7) then

$$\mathbf{V}_M = sF^2(G^2-1)\mathbf{1}_\phi . \tag{4.11}$$

The stability results for the basic state $\mathbf{B}_0$ with its associated magnetic wind $\mathbf{V}_M$ can then be found for both the E^A and E^S-fields. In each case, the magnetic wind is symmetric about the equator $z = 0$ and is westward travelling.

Since we fix the outer core radius at $s = 1$ then our aspect ratio of cylindrical radius to half-height will always be of the form $1 : \zeta$. In future, then, we will also refer to ζ as being the aspect ratio.

In order to make a comparison between the results of the previous chapter and with the results of FLMO, we have used an aspect ratio of outer annular radius to half-height of $\zeta = \pi/2$. However, in the viscous analyses of HF3,4, an aspect ratio of 1 was used. For both E^A and E^S-fields, we rework the stability problem for the aspect ratio of $\zeta = 1$ to directly compare our magnetostrophic results with the viscous results of HF3.

In each stability analysis conducted in the past, either by Fearn (1983b, 1984, 1985, 1988), HF1-4, or FLMO the s-dependence has always been taken in the form (4.2). Referring to Figure 3.1(i), as the parameter α is increased, the field becomes more and more concentrated towards the core-mantle-boundary (CMB). Recent evidence from the dynamo calculations of Glatzmaier & Roberts (1995a,b,1996,1997) suggests that field concentration towards the inner-core-boundary (ICB) may be important. To this end, we also consider the stability of s- and z-dependent basic fields whose radial dependence is given in (4.3). The choices (4.2) and (4.3) allow us to compare the stability results arising from similar field profiles: one concentrating towards the CMB and one towards the ICB. Contour plots showing meridional sections of the (axisymmetric) basic fields are shown in Figure 4.1.

In the previous chapter, we defined the "energetic Elsasser number" $\Lambda' \equiv E(\mathbf{B}_0)\Lambda$ [(3.30)]. Here $E(\mathbf{B}_0)$ is the dimensionless field energy, see (3.29), associated with the basic field $\mathbf{B}_0$. For the $s-$ and $z-$dependent basic fields considered in this chapter, values for $E(\mathbf{B}_0)$ are given in Table 4.1

TABLE 4.1: Dimensionless field energies $E(\mathbf{B}_0)$

Radial Dependence, $F(s)$	Axial Dependence, $G(z)$	Total Field Energy, $E(\mathbf{B}_0)$
(4.2)	(4.6)/(4.7)	0.150
(4.3)	(4.6)/(4.7)	.0523

In this chapter, all critical Elsasser numbers are quoted for the energetic version Λ'. The only cases where we use the traditional Elsasser number Λ are in Sections 4.3.4 and 4.4.4. This was necessary to compare our results with the viscous work of HF3.

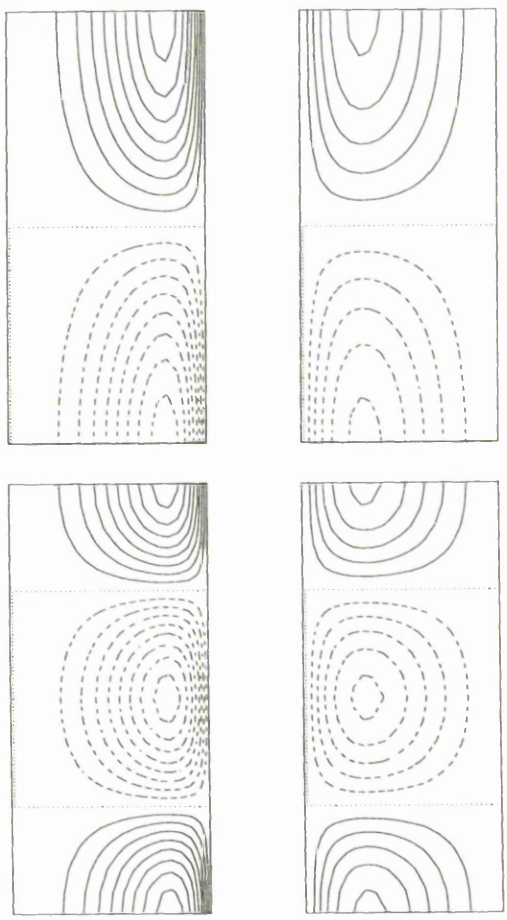

Figure 4.1: Meridional sections of the basic field $\mathbf{B}_0$. Top row: Dipole fields using G from (4.6). From left to right: (i) using F from (4.2), (ii) using F from (4.3). Bottom row: Quadrupole fields using G from (4.7). From left to right, the same order of s-dependencies $F(s)$ as used in the top row.

This chapter is concerned with determining the linear stability of s- and z-dependent basic fields and then analysing the impact of the (nonlinear) geostrophic flow on the instabilities. FLMO showed that for simple s-dependent basic fields, certain imposed differential rotations can lower Λ_c. In the previous chapter, we showed that the geostrophic flow induced subcritical behaviour in the most unstable mode for some combinations of basic fields and aspect ratios. Here, the linear results are new; previous eigenvalue analyses only considered basic fields of the form $\mathbf{B}_0(s)$. We also investigate whether subcriticality exists for the most unstable mode under dipolar and quadrupolar field configurations. problems (in which case V_G is identical between the problems) and

4.2 Problem Set Up

4.2.1 Expansions

Our model problem is identical in many respects to that discussed in the previous chapter. The main difference between this work and Chapter 3 is in the choice of basic field (4.1) which now provides for a z-dependence.

Working in the same annular geometry $\mathcal{A}$, using the same nondimensionalisation (3.5), governing equations (3.13, 3.14, 3.15) and field and flow decompositions (3.6, 3.7), the non-autonomous presence of the axial co-ordinate creates a coupling between the axial modes. This then requires solution expansions of the following form

$$X = \sum_{n=0}^{NZ} X_n(s,t)\cos\bar{n}(z+\zeta)e^{im\phi} + \text{CC} \tag{4.12}$$

$$Y = \sum_{n=1}^{NZ} Y_n(s,t)\sin\bar{n}(z+\zeta)e^{im\phi} + \text{CC} \tag{4.13}$$

where X represents any of v_s, v_ϕ, b_s or b_ϕ and Y stands for either v_z or b_z and NZ is the axial mode truncation. A value of $NZ = 8$ and a finite difference radial node truncation of $N = 101$ gave well converged solutions. As before, CC stands for "complex conjugate". All functions with subscripts $n \in [1, 2, ...)$ are complex. Here $\bar{n} = n\pi/2\zeta$ where we have chosen either $\zeta = \pi/2$ in order to compare our results with FLMO and Chapter 3, or $\zeta = 1$ in order to compare with HF3,4.

The boundary conditions remain unchanged from the previous chapter as they are autonomous in the variable z. Consequently, (3.21) and (3.24) are enforced at the FD node points corresponding to $s = s_{\rm ib}, 1$ over all the axial modes NZ. The perfect electrical conductor and no-normal flow conditions are once again enforced by using a Galerkin technique.

It should be pointed out that, under the magnetostrophic approximation, the governing equations do not determine the radial flow component corresponding to the zeroth axial mode $v_{s,0}$ [see (4.12)]. As discussed in the introduction, this zeroth axial mode is actually the non-axisymmetric part of the radial geostrophic flow [see (1.16)]

$$v_{s,0} = V_G^s - \langle V_G^s \rangle \tag{4.14}$$

where $\langle \cdot \rangle = (2\pi)^{-1} \int_0^{2\pi} \cdot \, \mathrm{d}\phi$. Further work is needed to resolve V_G^s and hence $v_{s,0}$. At present, however, we set $v_{s,0} \equiv 0$, since our motivation for examining this magnetic stability problem is that much of the physics will carry over to a similar problem in a spherical shell geometry.

4.2.2 Symmetry and Solution

The choice of basic E^A or E^S field leads to a partitioning of the linear stability problem into solutions of the dipole type and of the quadrupole type. This can be seen in the perturbation equations (3.11,12,13) from the particular choice of G. Although the equations are not separable in z, the (linear) instabilities manifest themselves through the following symmetries. As illustrated by Gubbins & Zhang (1993), when $\mathbf{B}_0 \in E^A$ then either the dipolar symmetry arises

$$\mathcal{D}: \quad \mathbf{b} \in E^A \text{ and } \mathbf{v} \in E^S \tag{4.15}$$

or the quadrupolar symmetry arises

$$\mathcal{Q}: \quad \mathbf{b} \in E^S \text{ and } \mathbf{v} \in E^A \,. \tag{4.16}$$

Similarly, if $\mathbf{B}_0 \in E^S$ then either a dipolar instability appears

$$\mathcal{D}': \quad \mathbf{b} \text{ and } \mathbf{v} \in E^A \tag{4.17}$$

or a quadrupole type instability appears

$$\mathcal{Q}': \quad \mathbf{b} \text{ and } \mathbf{v} \in E^S \,. \tag{4.18}$$

Strictly speaking, both symmetries are present in any problem, but one symmetry will dominate the other by being more unstable. In terms of the basic field $\mathbf{B}_0$ (and the magnetic wind $\mathbf{V}_M$) we may think of our basic configuration as being dipolar in the case of an equatorially antisymmetric $\mathbf{B}_0$ or quadrupolar in nature when $\mathbf{B}_0 \in E^S$.

For the linear problem, and by virtue of our choice of basic field symmetry, two problems are being solved simultaneously and independently. However, as one moves into the nonlinear regime, it is not clear if the symmetries from the linear problem will be maintained. It is very possible that a symmetry-breaking bifurcation may take place where one symmetry excites the other through the nonlinear action of the geostrophic flow. As shown in the Appendix, V_G is dependent on the various contributions from each axial mode

$$V_G = 2^{1/2}\Re \sum_{n=0}^{NZ} \alpha_n (s^{-1} b_{s,n} + b_{s,n} D - \bar{n} b_{z,n}) b^*_{\phi,n} \tag{4.19}$$

$$\text{where } \alpha_n = \begin{cases} 2\zeta & \text{if } n = 0 \\ \zeta & \text{if } n > 0 \end{cases} \tag{4.20}$$

Here, V_G is as implemented in Chapter 3. In the cases where we examine the effect of the finite ageostrophic magnetic wind, Appendix C also shows that $\mathbf{V}_M$ does not alter the axial mode interaction in the linear regime. The magnetic wind is implemented by setting $\mathbf{V}_0 = \mathbf{V}_M = sF^2(G^2 - 1)\mathbf{1}_\phi$ from (4.11) in the induction equation (3.12).

The stability problem was then solved by an LU-decomposition method applied to a part spectral and part finite-difference discretization of the governing equations. As in the previous chapter, a semi-implicit method was employed incorporating the Crank-Nicholson scheme for the diffusive terms and an Adams-Bashforth method for the remaining terms. The main difference between this chapter and the last lies in the fact that the axial modes remain coupled and the solution must be sought for each axial mode simultaneously. Using the Crank-Nicholson/Adams-Bashforth allowed us to deal with the terms coupling individual axial modes to explicitly. This resulted in a block-banded system matrix where each axial mode $i = 0, ..., NZ$ has an associated $(2N-1, 2N-1)$ block over the real numbers. The block-banded structure was made use of to quickly LU-decompose the system matrix by individually decomposing each block in turn. This proved highly efficient.

4.2.3 Consistency Condition

Consider the perturbation form of the magnetostrophic momentum equation

$$\mathbf{1}_z \times \mathbf{V} = -\nabla\pi + (\nabla \times \mathbf{B}_0) \times \mathbf{b} + (\nabla \times \mathbf{b}) \times \mathbf{B}_0. \tag{4.21}$$

If one takes the z-component of the curl of (4.21) then

$$-\frac{\partial v_z}{\partial z} = \{\nabla \times [(\nabla \times \mathbf{B}_0) \times \mathbf{b} + (\nabla \times \mathbf{b} \times \mathbf{B}_0)]\}_z. \tag{4.22}$$

Now, the no-normal-flow boundary conditions require that $v_z = 0$ on $z = \pm\zeta$. Therefore

$$\int_{-\zeta}^{\zeta} \frac{\partial v_z}{\partial z}\, \mathrm{d}z = \left[v_z\right]_{-\zeta}^{\zeta} = 0.$$

Consequently, any solution we find must satisfy the consistency relationship

$$\int_{-\zeta}^{\zeta} \{\nabla \times [(\nabla \times \mathbf{B}_0) \times \mathbf{b} + (\nabla \times \mathbf{b} \times \mathbf{B}_0)]\}_z \, \mathrm{d}z = 0 \tag{4.23}$$

$$\iff \quad \int_{-\zeta}^{\zeta} \frac{1}{s}\frac{\partial}{\partial s}\left[b_s \frac{\partial}{\partial s}(sB_0)\right] + \frac{1}{s}\frac{\partial}{\partial s}\left[sb_z \frac{\partial B_0}{\partial z}\right] + \frac{1}{s^2}\frac{\partial b_\phi}{\partial \phi}\frac{\partial}{\partial s}(sB_0) + \frac{B_0}{s^2}\frac{\partial^2}{\partial s \partial \phi}(sb_\phi) - \frac{B_0}{s^2}\frac{\partial^2 b_s}{\partial \phi^2}\, \mathrm{d}z = 0. \tag{4.24}$$

Where we have written $\mathbf{B}_0 = B_0\mathbf{1}_\phi$ for the basic state field. Immediately, we see that if the basic field is z-independent as in Chapter 3 [$B_0 = sF(s)$] then (4.24) will always be satisfied. This can be verified upon substituting the expansion forms for $\mathbf{b}$ and integrating in z. Since the term involving b_z vanishes from (4.24) because B_0 is z-independent, then the remaining terms are all proportional to $\cos\bar{n}(z+\zeta)$ (with $n > 0$). On integration between $z = -\zeta$ and ζ (4.24) vanishes.

However, if we take $B_0 = sF(s)G(z)$ as is done in this chapter with $G(z)$ selected from (4.6) or (4.7), then it is not clear upon making the substitutions (4.12), (4.13) that (4.24) will be satisfied. This issue can partly be resolved in the following way. Each term in (4.24) will be proportional to either

$$\begin{aligned} G(z)\cos\bar{n}(z+\zeta) &= \frac{1}{2}[\cos(\bar{n}+\bar{l})(z+\zeta) + \cos(\bar{n}-\bar{l})(z+\zeta)] \\ G'(z)\sin\bar{n}(z+\zeta) &= -\frac{1}{2}[\cos(\bar{n}+\bar{l})(z+\zeta) - \cos(\bar{n}-\bar{l})(z+\zeta)] \end{aligned}$$

where $\bar{n} = n\pi/2\zeta$, $n \in [0, 1, 2, ...)$ and a prime indicates the z-derivative. Consider the dipole field configuration created by choosing $l = 1$ [see (4.6)] for $G(z)$. Provided

the most unstable instability is quadrupolar in nature, then it is the even modes n which are selected and consequently (4.24) must vanish. A similar result exists if one chooses $l = 2$ [see (4.7)] and the dipolar instability. However, it is not clear as to whether (4.24) will or will not be satisfied if either of the other two combinations of basic field and instability are selected. In this event, we cannot say anything about our results and they are not quoted.

This represents a serious deficiency in cylindrical models under the magnetostrophic approximation in the *linear* regime. In order to address this problem, further work is needed. The restoration of a some form of viscosity to the right hand side of the magnetostrophic momentum equation (4.21) may help to resolve the problem (Hollerbach, private communication).

4.3 Dipole Field Results

In this section we examine the stability results for a number of basic field configurations of the dipole type (4.1). Throughout this section, the form (4.6) is chosen for $G(z)$. We will then refer to the field whose s-dependence F is chosen from (4.2) as being the *dipole field*. In Section 4.3.3 we use the form (4.3) for F. In that section only, we will refer to the basic state as being the *dipole field concentrating to the ICB*.

The results are organised as follows. Firstly we consider magnetic instabilities arising from the basic state field with annular aspect ratio of $\zeta = \pi/2$. Then, in the same problem, the impact of the consistent magnetic wind is assessed. For the third case, we investigate field concentration to the ICB. Finally, the stability for the basic field is reworked for the new aspect ratio of 1.

4.3.1 Comparison with the z-Independent Results

The stability results for the dipole field are detailed in Table 4.2 below. A field profile for the dipolar axisymmetric basic state can be located in Figure 4.1.

TABLE 4.2: Critical parameter values for the dipole field.

m	1	2	3	4
Λ_c'	2.381	0.8159	0.5256	0.4955
ω_c	-0.8963	0.6835	-5.227	-11.93
Modes	$\mathcal{Q}$	$\mathcal{Q}$	$\mathcal{Q}$	$\mathcal{Q}$
Bifurcation	Sub	Sub	Sub	Sub

The results for the first four azimuthal modes, considered in isolation due to the separability in ϕ, are shown. The higher azimuthal modes are significantly more damped by ohmic diffusion than those shown here and are consequently not quoted. In Table 4.1 we have already demonstrated that the z-dependent basic fields have weaker average field strengths than their z-independent counterparts of Chapter 3. Use of the energetic Elsasser number allows a realistic comparison across z-independent and z-dependent basic fields. The values of Λ_c' corresponding to the z-independent field using (4.2) (see Table 3.5) are the correct comparison with the results in this chapter. Here, the only difference between the basic fields is in the form for G: the z-dependent case (4.6) versus the z-independent case where $G(z) = 1$. On inspection of Tables 4.2 and 3.5, we see that the introduction of a z-dependence has had a destabilising effect.

The most unstable mode for the dipolar basic field is the $m = 4$, quadrupolar $\mathcal{Q}$-instability with frequency -11.93. Further, the instability would appear to resist the formation of columnar convection cells which are equatorially symmetric in nature (Busse, 1970). Comparison of our most unstable $m = 4$ mode contrasts with the similar but viscous results of HF3 which suggest that $m = 2$ is the preferred mode. This has prompted us to rework our problem for their aspect ratio of $\zeta = 1$ later in the chapter.

In the manner of Chapter 3, we use the linear eigenfunction at $\Lambda = \Lambda_c$ (or equivalently $\Lambda' = \Lambda_c'$) to generate the geostrophic flow $V_G^{(0)}(s)$ through (4.19). Normalising that flow and modulating it with the modified magnetic Reynolds' number and enforcing the flow as the differential rotation

$$\mathbf{V}_0(s) = \mathcal{R}_m V_G^{(0)} \mathbf{1}_\phi \tag{4.25}$$

allows us to determine the initial effect of V_G on the solution in the nonlinear regime. [Typically, $\mathcal{R}_m = 10^{-3}$.] In contrast with the results of HF4 who did not find subcritical instability, we find that the geostrophic flow has an inherently destabilising nature with the most unstable modes forming subcritical instabilities. The subcritical effect was verified in the fully nonlinear regime (i.e., by calculating the geostrophic flow at every time step) and instability was found at value of $\Lambda' = 0.4875$ ($\Lambda_c = 0.4955$). Unfortunately, due to the subcritical nature of the bifurcation, we expect and find that the Ekman branch is unstable. At $\Lambda' = 0.4875$ we found exponentially growing solutions and no field equilibration.

The real and imaginary parts of the linear solution $\mathbf{b}$ and $\mathbf{v}$ [see (4.12) and (4.13)] are represented in Figures 4.2 and 4.3. Meridional sections, drawn as contour plots, show the structure of the most unstable, $m = 4$, mode at $\Lambda'_c = 0.4955$. The eigenfunctions for $\mathbf{b}$ and $\mathbf{v}$ have been normalised separately but in the same way. For example, the field was normalised by dividing by the quantity

$$\sum_{n=0}^{NZ} (b^r_{z,n} + ib^i_{z,n}) \sin \bar{n}(z+\zeta) e^{im\phi} \tag{4.26}$$

evaluated at the point $P = (s_{max}, \phi_{max}, z_{max})$. Here, a superscript r/i refers to the real/imaginary part. P was found as the point which maximised the real part of b_z, i.e. P is the point for which

$$\Re(b_z) = \sum_{n=0}^{NZ} (b^r_{z,n} \cos m\phi - b^i_{z,n} \sin m\phi) \sin \bar{n}(z+\zeta) \tag{4.27}$$

$$\text{where } \phi = \frac{1}{m} \arctan\left(-\frac{b^i_{z,n}}{b^r_{z,n}}\right) \tag{4.28}$$

is a maximum.

The first observation that can be made is that the instability, as one intuitively expects, tends to concentrate in the region close to the CMB (towards the right hand side of the plots). The quadrupolar nature of the instability is also evident. The plots are well resolved showing large scale structure occurring on lengthscales over the radius of the annulus. The corresponding geostrophic flow structure is shown in Figure 4.4.

We reserve comparing the field (3.12) from Chapter 3 with the dipole field concentrating to the ICB until Section 4.3.3.

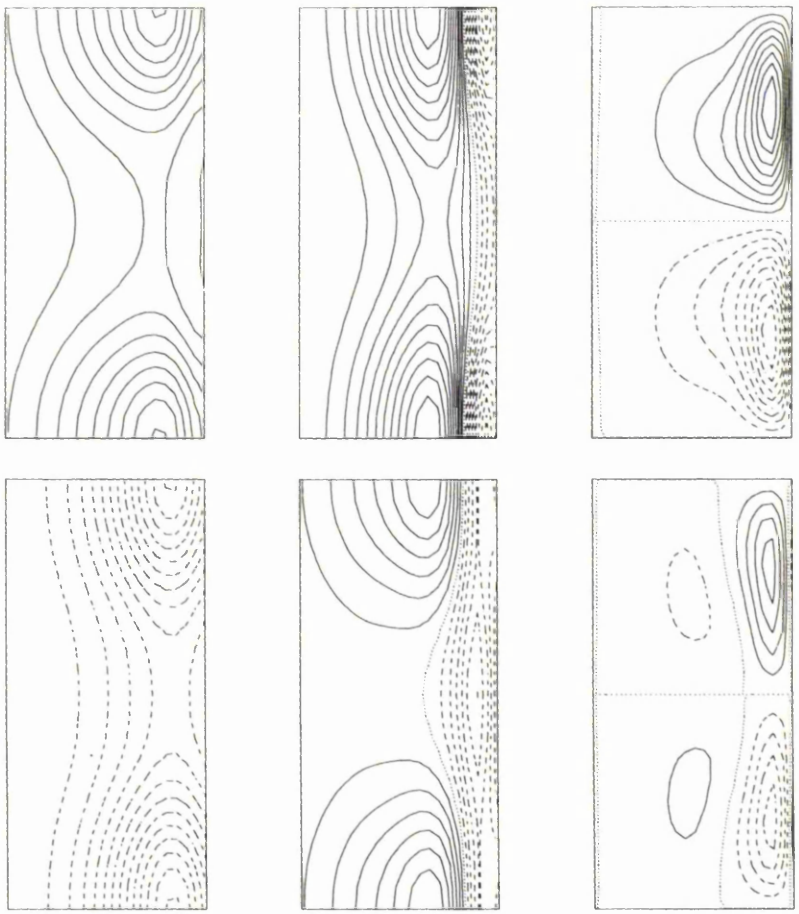

Figure 4.2: The perturbed magnetic field **b**. Meridional sections maximising over ϕ for the most unstable $m = 4$ mode under the dipole field configuration in Figure 4.1(i). Top row, from left to right: the real part of (i) b_s, (ii) b_ϕ and (iii) b_z. The bottom row is as the top row but shows the corresponding imaginary parts. All figures use the same contour interval.

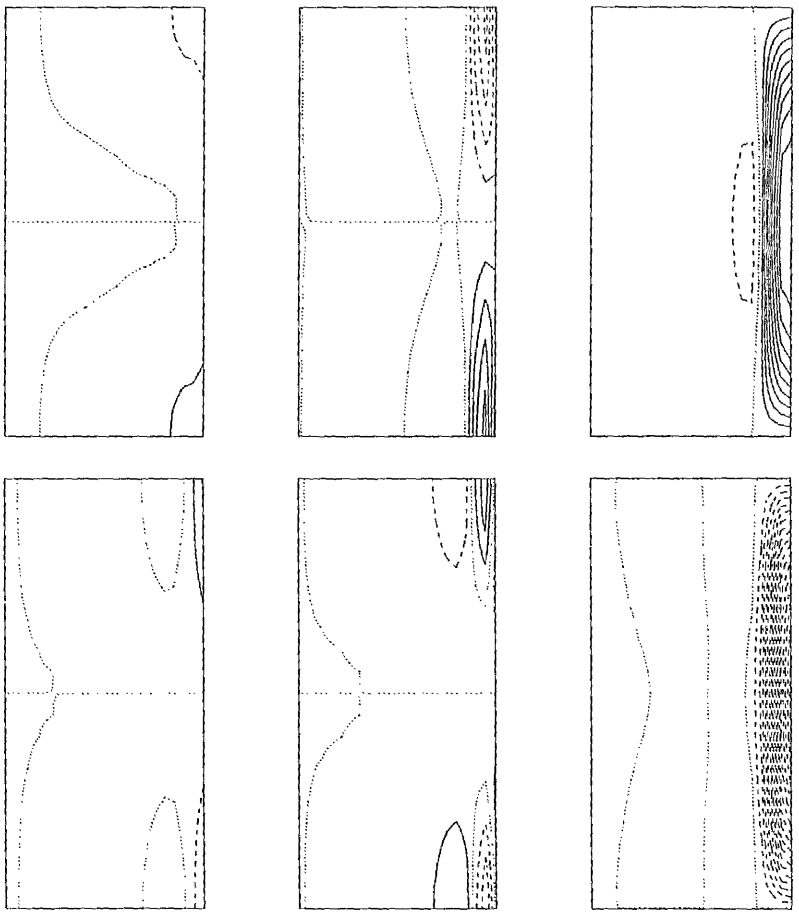

Figure 4.3: The perturbed flow field $\mathbf{v}$. Meridional sections maximising over ϕ for the most unstable $m = 4$ mode under the dipole field configuration in Figure 4.1(i). Top row, from left to right: the real part of (i) v_s, (ii) v_ϕ and (iii) v_z. The bottom row is as the top row but shows the corresponding imaginary parts. All figures use the same contour interval.

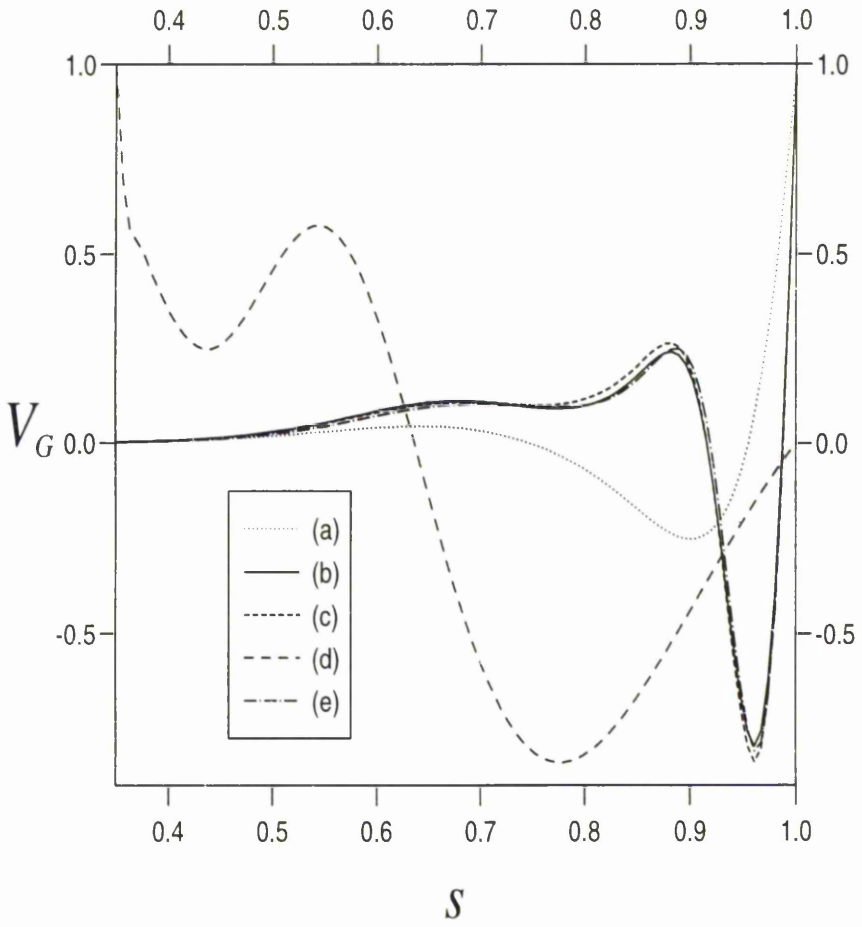

Figure 4.4: Profiles of the geostrophic flow at $\Lambda' = \Lambda'_c$. In the annular container with $\zeta = \pi/2$, V_G is shown as it arises from the most unstable mode resulting from perturbations to the following basic fields: (a) the z-independent field with $F(s)$ taken from (4.2); and for the following dipolar basic fields with (b) $F(s)$ taken as in (4.2) and $G(z)$ taken in (4.6), (c) as part (a) but with the consistent magnetic wind $\mathbf{V}_M$ in place, (d) where basic field concentrates to the ICB, and (e) the aspect ratio is modified to $\zeta = 1$ for case (b).

4.3.2 The Effect of the Magnetic Wind

Along with the basic $\mathcal{D}$-field configuration, we add the equatorially symmetric magnetic wind into the stability analysis. Here, with $\zeta = \pi/2$, we implement (4.11) with F and G taken as in (4.2) and (4.6), respectively. This is achieved in the problem by setting $\mathbf{V}_0 = \mathbf{V}_M$ in the perturbation equations (3.11, 12, 13). The results, in the same form as Table 4.2, are given in Table 4.3.

TABLE 4.3: Critical parameter values for the $\mathcal{D}$ basic field with $\mathbf{V}_M$.

m	1	2	3	4
Λ_c'	–	0.8661	0.5394	0.5027
ω_c	–	−1.355	−4.688	−11.49
Modes	–	$\mathcal{Q}$	$\mathcal{Q}$	$\mathcal{Q}$
Bifurcation	–	Sub	Sub	Sub

The crucial question regarding the effect of the magnetic wind is does it change the results of the previous section? The effect of $\mathbf{V}_M$ is very slight indeed and the same qualitative features are seen in the eigenfunctions with and without the presence of $\mathbf{V}_M$. We do not reproduce these here since the eigenfunctions appear identical to the plots in Figures 4.2 and 4.3.

In general, the magnetic wind has a mildly stabilising influence and raises the critical Λ_c' for the most unstable mode from $\Lambda_c' = 0.4955$ to $\Lambda_c' = 0.5027$ whilst preserving its quadrupolar symmetry. One of the few changes induced by the magnetic wind occurs for the $m = 1$ mode. Here, this mode becomes more stable, exchanges its quadrupolar symmetry for a dipolar symmetry under $\mathbf{V}_M$, and the nonlinear effect due to the geostrophic flow leads to a supercritical bifurcation. The presence of the magnetic wind, here, changes the nonlinear development of the instability. Although the introduction of $\mathbf{V}_M$ has altered some of the frequencies, it has changed the frequency of the most unstable mode only slightly.

In the light of the (almost) identical eigenfunctions with and without the magnetic wind, it comes as no surprise that the geostrophic flow profiles are very similar. The profile for V_G can be seen as graph (c) on Figure 4.4.

4.3.3 The Effect of Field Concentration Towards the ICB

Prior to this work, studies of the stability of field profiles in the annular domain have been primarily restricted to certain choices of basic state. In particular, those basic states were initially only chosen to be s-dependent as this led to a problem separable in z. The main aim of this chapter has been the introduction of an axial dependence, and its associated symmetries, into the basic field configuration.

The s-dependencies of our basic states have, at this point, lain unchanged from those first studies [e.g., Fearn (1983b)]. The particular form for F was chosen so that the basic toroidal field would vanish on the inner and outer core boundaries whilst a parameter α allowed variations on this theme (see Figure 3.1 for examples). It was then possible to gain some insight into how results depended on the choice of basic field. However, the function F, tended to concentrate field *away* from the ICB (Figure 3.1). We now investigate the form (4.3) for F in a field concentrating to the ICB. The structure of the new basic state can been seen in Figure 4.1(iii).

TABLE 4.4: Critical parameter values using F in (4.3).

m	1	≥ 2
Λ'_c	1.633	> 2.6
ω_c	1.318×10^{-3}	–
Modes	$\mathcal{Q}$	–
Bifurcation	Sub	–

What is immediately obvious from the stability results in Table 4.4 is that those modes that were most unstable when the "traditional" form for F, (4.2), was used have now been completely damped by ohmic diffusion. For the azimuthal modes having $m \geq 2$, the energetic Elsasser number Λ' now lies in excess of 2.6 (corresponding to $\Lambda \geq 65$) and the most unstable mode is now the $m = 1$ mode.

The difference can be explained in the following way. We know that any instability will tend to concentrate where the basic field is strongest and our new choice of s-dependence has forced the instability towards the ICB. Now, ohmic diffusion acts on modes which contain a lot of structure (essentially, it is there that the ohmic diffusive $\nabla^2\mathbf{b}$ term can become large). Consider an instability with azimuthal wavenumber m forming at a radius $s = a$ and then consider the same

non-axisymmetric mode appearing at a radius $s = b < a$. The wavelength of the m^{th} azimuthal mode forming at $s = b$ is $2\pi b/m$ and must be less than its corresponding wavelength at $s = a$. However, the instability still contains m oscillations at $s = b$ and ohmic diffusion "sees" a more compact structure that it can damp quite effectively. This is explains why the higher order m modes have been heavily damped for field concentration towards the ICB. The most unstable mode is the $m = 1$ instability and $\Lambda_c' = 1.633$. This is as opposed to $m = 4$ and $\Lambda_c' = 0.4955$ in the case of field concentration towards the CMB. So the effect of field concentration to the ICB has stabilised the system. However, the actual $m = 1$ mode itself, which is a quadrupole instability, has been destabilised by the new field concentration.

The eigenfunctions for the field and flow may be seen in Figures 4.5 and 4.6. One immediately notices that both field and flow concentrates towards the ICB boundary and that the azimuthal flow now fills the length of the annulus.

Although the most unstable mode retains its quadrupolar symmetry, the simple effect of concentrating field to the ICB has slightly increased Λ_c', swapped the most unstable mode and drastically reduced the frequency from -11.93 to 3.284×10^{-3} – the instability is now almost stationary. The nonlinear effect of the geostrophic flow still remains subcritical.

It is worth observing that the addition of this section's dipolar modulation to a previously z-independent basic field [i.e. in Chapter 3, field (3.12)] has stabilisied the system. This contrasts the destabilising result of Section 4.3.1.

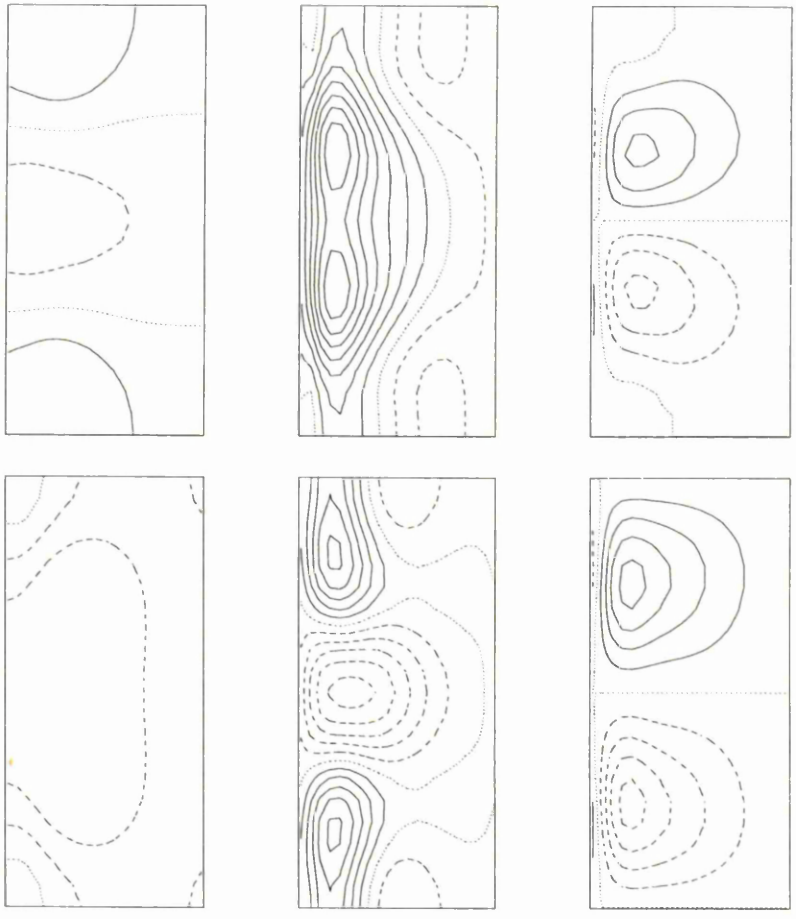

Figure 4.5: For basic dipolar field concentration to the ICB: Top row, the real parts of (i) b_s, (ii) b_ϕ and (iii) b_z. The corresponding imaginary parts are shown in the bottom row. All plots share the same contour interval.

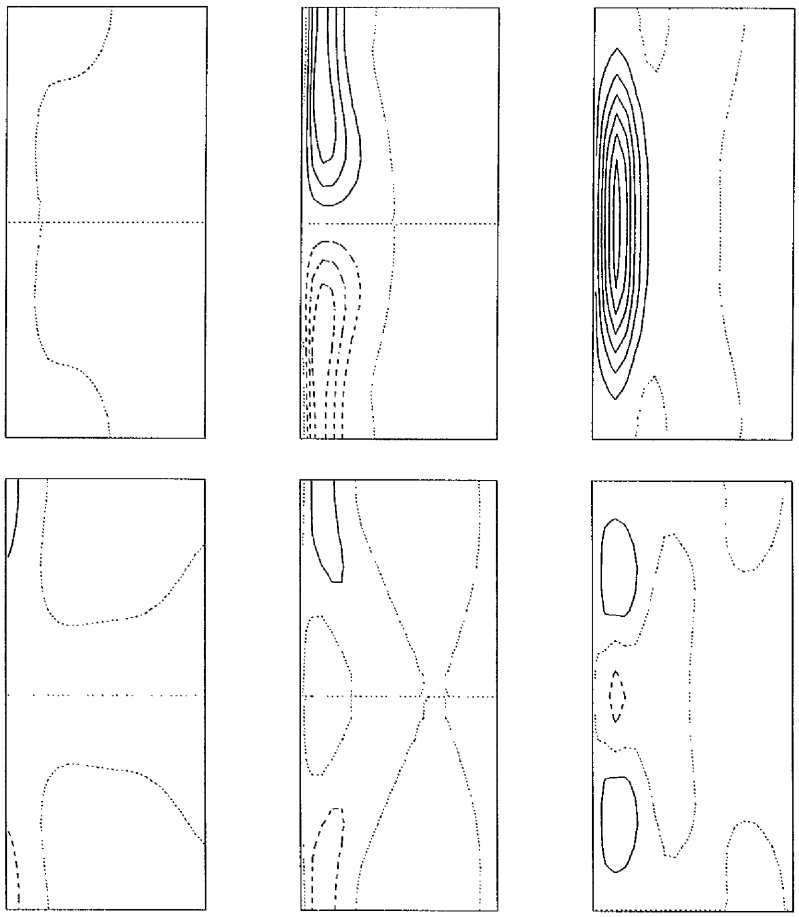

Figure 4.6: For basic dipolar field concentration to the ICB: Top row, the real parts of (i) v_s, (ii) v_ϕ and (iii) v_z. The corresponding imaginary parts are shown in the bottom row. All plots share the same contour interval.

4.3.4 Comparison with the Aspect Ratio $\zeta = 1$

Thus far, we have considered only aspect ratios of $\zeta = \pi/2$ We now modify the aspect ratio to $\zeta = 1$.

This modification facilitates a closer comparison of our magnetostrophic results with the viscous analyses of HF3 who used an aspect ratio of $\zeta = 1$ and took the Ekman number $E = 10^{-4}$. Choosing our basic state as in Section 4.3.1 we rework the magnetostrophic stability analysis for the new aspect ratio. The results along with the comparable viscous analysis (shown italicised and courtesy of HF3) are presented in Table 4.5 below.

TABLE 4.5: Critical values for the aspect ratio $\zeta = 1$. [HF3 italicised.]

m	1	2	3	4
Λ_c	–	13.98	7.082	5.871
	1.85	*1.67*	*2.86*	–
ω_c	–	−2.939	−5.722	−11.45
	-0.28	*-0.27*	*0.20*	–
Modes	–	$\mathcal{Q}$	$\mathcal{Q}$	$\mathcal{Q}$
	D	*D*	*D*	–
Bifurcation	–	Sub	Sub	Sub
	Super	*Super*	*Super*	–

The critical parameter values in Table 4.5 are given in terms of Λ and without recourse to the energetic Elsasser number Λ'. This was done since we used precisely the same basic field as HF3 and their results were given in terms of Λ.

It is immediately obvious that the viscous analysis shows a basic field which is far more unstable than its corresponding magnetostrophic counterpart. This is somewhat surprising since the presence of viscosity might be expected to provide a stabilising influence. This was observed when HF2 compared their (linear) viscous results for $\mathbf{B}_0 = \mathbf{B}_0(s)$ with the corresponding magnetostrophic results of Fearn (1988). The unknown role of the zeroth and undetermined axial mode $v_{s,0}$ may well be the cause of the discrepancy or there may be no discrepancy at all since we were unable to find the corresponding dipolar instability [see Section 4.2.3]. A viscous

analysis in an annular geometry allows determination of $v_{s,0}$ but, as already stated, further work will be required to determine $v_{s,0}$.

Let us now describe the effect of changing the aspect ratio between our two magnetostrophic cases. As in Section 4.3.1, the most unstable mode is the $m = 4$ azimuthal mode, the instability remains quadrupolar and the bifurcation due to the geostrophic flow is still subcritical. The frequency of the most unstable mode has changed only slightly: from a value of -11.93 to -11.45 for $\zeta = 1$. The frequencies of the $m = 1$ and $m = 2$ modes have changed and these modes are considerably more damped. The results for the energetic Elsasser number Λ'_c are shown in Table 4.6.

TABLE 4.6: Comparison of Λ' between aspect ratios.

Aspect Ratio ζ	$m = 1$	$m = 2$	$m = 3$	$m = 4$
1	–	2.097	1.062	0.8807
$\pi/2$	2.381	0.8159	0.5256	0.4955

One can see from Table 4.6 that the critical parameter values have become stabilised on decreasing ζ from $\pi/2$ to 1. Again, the increase in Λ'_c can be understood in terms of diffusion acting with greater vigour on axial modes now compressed into an annulus of smaller height. Note that the symmetry of each mode remains unchanged on changing the aspect ratio except for the $m = 1$ mode. The components of the most unstable mode are shown in Figure 4.7 and 4.8. The nonlinear development due to V_G has remained the same, again with the exception of the $m = 1$ azimuthal mode which has become supercritical in the new aspect ratio.

4.4 Quadrupole Field Results

In a similar fashion to the previous section, we examine the stability of a number of quadrupolar basic states (4.1). The results are organised in an analogous way to Section 4.3 and unless otherwise stated, we set $\zeta = \pi/2$. We consider the stability of (4.1) with G taken from (4.7) and refer to it as the *quadrupole field*. Similarly to the stability analyses for the dipolar basic field in Section 4.3, we consider the ageostrophic magnetic wind and then field concentration towards the ICB [referring to this configuration as the *quadrupole field concentrating to the ICB*] before concluding with a stability analysis of the *quadrupole field* where $\zeta = 1$.

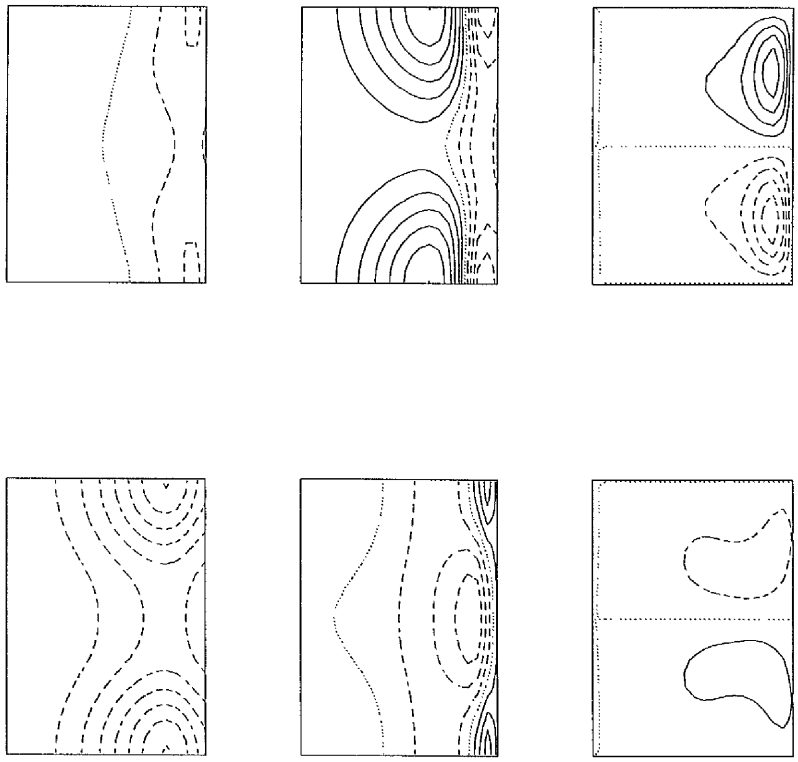

Figure 4.7: As for Figure 4.2 but for $\zeta = 1$ and where $F(s)$ is taken from (4.2) and $G(z)$ is taken from (4.6). Top row, the real parts of (i) b_s, (ii) b_ϕ and (iii) b_z. The corresponding imaginary parts are shown in the bottom row. All plots share the same contour interval.

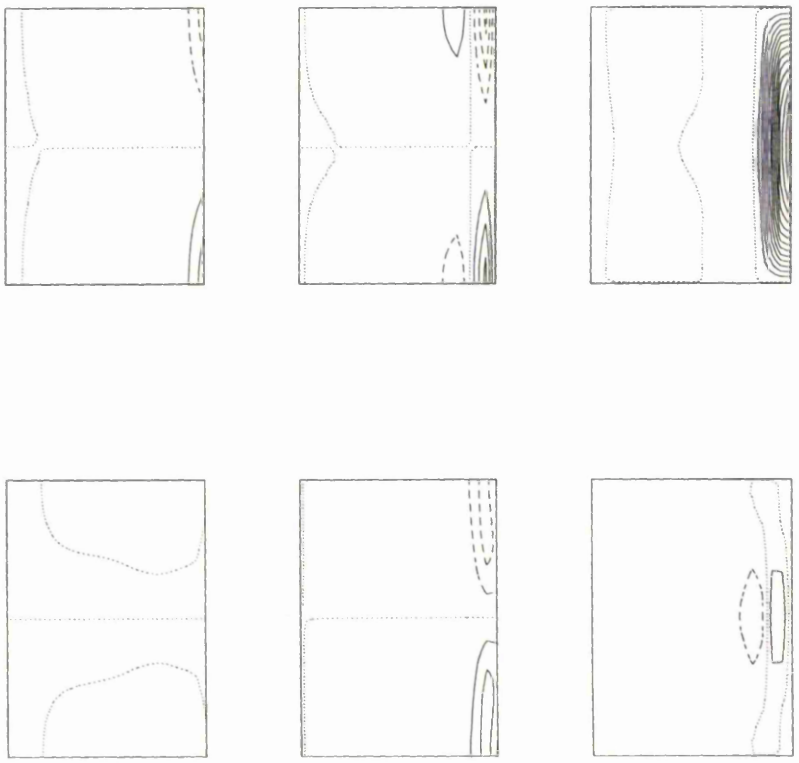

Figure 4.8: Similarly to Figure 4.7 but for the flow field $\mathbf{v}$. Top row, the real parts of (i) v_s, (ii) v_ϕ and (iii) v_z. The corresponding imaginary parts are shown in the bottom row. All plots share the same contour interval.

4.4.1 Comparison with z-Independent Results

The stability results for the quadrupole field are detailed in Table 4.7. A meridional section showing the basic state can be seen in Figure 4.1(iii).

TABLE 4.7: Critical parameter values for the $\mathcal{Q}$ basic state.

m	1	2	3	4
Λ'_c	1.761	0.9101	0.6447	0.6216
ω_c	-0.4679	-1.177	-4.231	-10.20
Modes	$\mathcal{D}'$	$\mathcal{D}'$	$\mathcal{D}'$	$\mathcal{D}'$
Bifurcation	Sub	Sub	Sub	Sub

As in Section 4.3, the results for the first four azimuthal modes are shown (the higher azimuthal modes being significantly more damped than those shown here).

The most unstable mode for the quadrupolar basic field is the $m = 4$, dipolar $\mathcal{D}'$-instability with frequency -10.20. The viscous stability analysis of HF3 suggest that the $m = 2$, quadrupole $\mathcal{Q}'$ instability is the preferred mode. However, they worked with $\zeta = 1$ and our results are for $\zeta = \pi/2$. In Section 4.4.4, we rework our problem for their aspect ratio.

It is possible to compare the results of Table 4.7 directly with the z-independent results of the previous chapter. In terms of the energetic Elsasser number Λ', Tables 3.5 and 4.7 show that the quadrupolar modulation (4.7) to the z-independent basic field is stabilising. This contrasts with the result where the modulation of a dipolar axial dependence destabilised the system.

The real and imaginary parts of the solution are represented in Figures 4.9 and 4.10. Meridional sections (see Section 4.3.1 for an explanation of the normalisation procedure used) as contour plots show the most unstable, $m = 4$, mode at $\Lambda'_c = 0.6216$.

The nonlinear effect of V_G on every mode considered was to destabilise the system. A profile for the geostrophic flow corresponding to the most unstable mode may be found in Figure 4.11 and compared with the z-independent result. The effect of the geostrophic flow on the most unstable mode from the z-independent case gave a supercritical bifurcation. The most unstable mode for the quadrupole field was subcritical due to V_G. One can clearly see that V_G corresponding to the quadrupole

field (b) possesses a strong amount of negative in the vicinity of $s = 0.9$ whilst (a) does not. This is consistent with the findings of FLMO who suggest negative outward gradient in the shear flow leads to subcriticality.

We compare (3.12) from Chapter 3 with the z-dependent, quadrupole field concentrating to the ICB at the end of Section 4.4.3.

4.4.2 The Effect of the Magnetic Wind

Along with the quadrupolar field we add the consistent, symmetric magnetic wind (4.11) into the stability analysis of the basic $\mathcal{Q}$-field. Here, $\mathbf{V}_M$ is implemented by setting $\mathbf{V}_0 = \mathbf{V}_M$ from (4.11) in the equations (3.11, 12, 13). The results are given in Table 4.8.

TABLE 4.8: Critical parameter values for the $\mathcal{Q}$-basic field with $\mathbf{V}_M$.

m	1	2	3	4
Λ_c'	1.818	0.9189	0.6513	0.6251
ω_c	−0.1393	−0.7138	−3.785	−9.786
Modes	$\mathcal{D}'$	$\mathcal{D}'$	$\mathcal{D}'$	$\mathcal{D}'$
Bifurcation	Sub	Sub	Sub	Sub

On comparing the results from this Section with the results of Section 4.4.1 there is very little difference indeed. We do not reproduce the eigenfunctions here as they are very similar to those already given in Figure 4.9 and 4.10 in the absence of $\mathbf{V}_M$. The critical energetic Elsasser numbers for the most unstable $m = 3$ modes are very similar at $\Lambda_c' = 0.6251$ including $\mathbf{V}_M$ to $\Lambda_c' = 0.6216$ without. All the solution symmetries remain the same and the nonlinear development of the geostrophic flow retains the same bifurcation sequence for each mode. The only difference between the cases with and without $\mathbf{V}_M$ is where the critical frequencies are concerned. It appears that the instability is carried along by the magnetic wind.

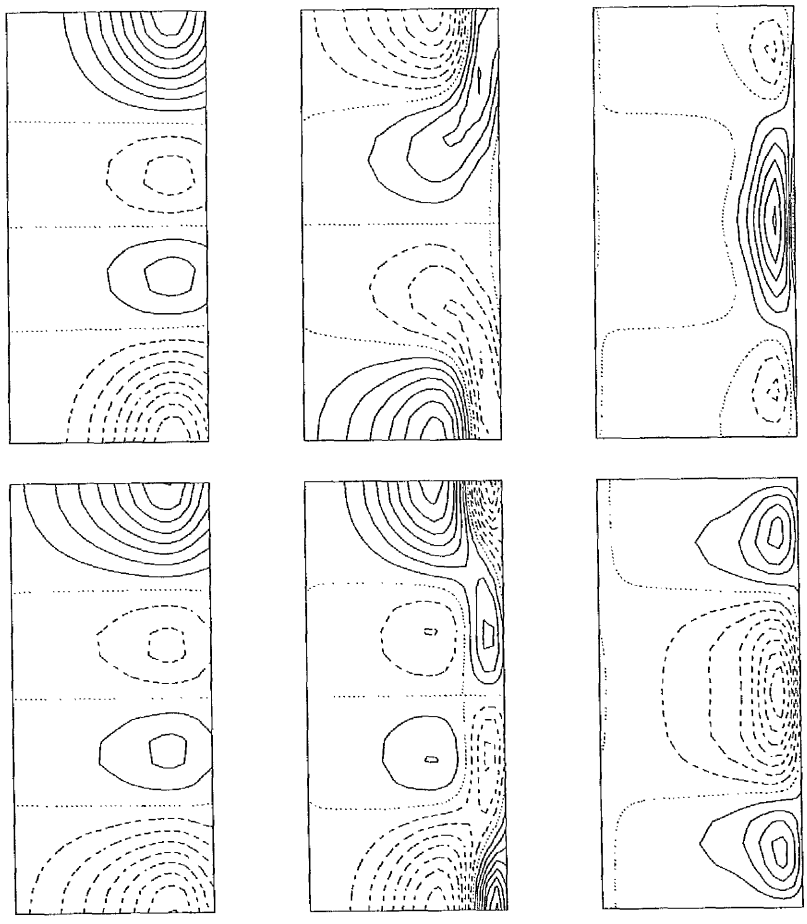

Figure 4.9: As Figure 4.2, the perturbed magnetic field $\mathbf{b}$ for the most unstable $m = 4$ mode under the quadrupole field configuration in Figure 4.1(ii). Top row: (i) b_s, (ii) b_ϕ and (iii) b_z. The corresponding imaginary parts are shown on the bottom row. All plots share the same contour interval.

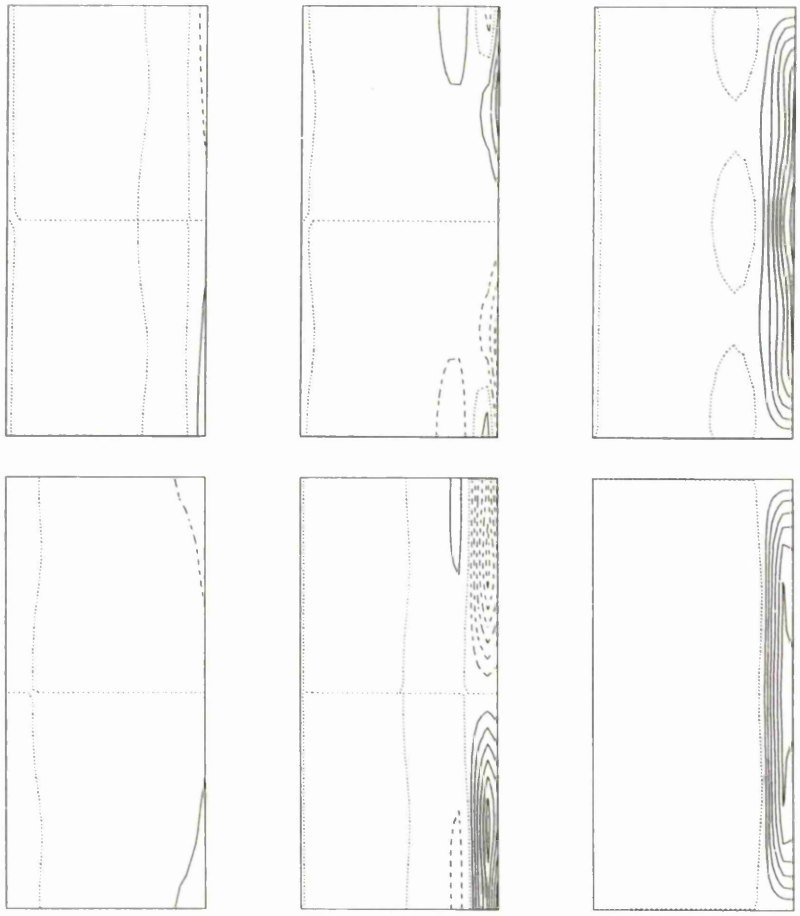

Figure 4.10: Similarly to Figure 4.9, the most unstable mode now showing the perturbed flow field $\mathbf{v}$ under the quadrupolar field configuration. Top row: (i) v_s, (ii) v_ϕ and (iii) v_z. The corresponding imaginary parts are shown on the bottom row. All plots share the same contour interval.

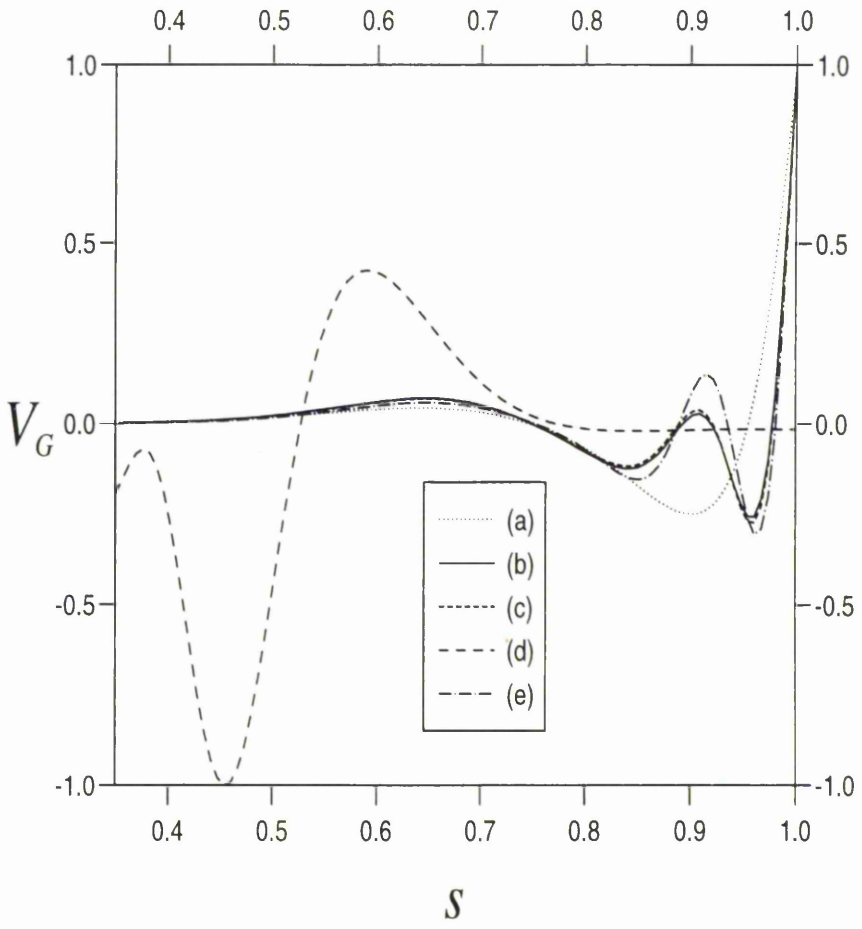

Figure 4.11: Profiles of the geostrophic flow at $\Lambda' = \Lambda'_c$ as in Figure 4.4 but where a quadrupolar z-dependence (4.7) is used in the basic state magnetic field.

4.4.3 The Effect of Field Concentration Towards the ICB

We now consider the stability of the quadrupole field concentrating to the ICB [see Figure 4.1(vi)]. In the absence of the magnetic wind, the stability results are tabulated in Table 4.9 below.

TABLE 4.9: Critical parameter values using F in (4.3).

m	1	≥ 2
Λ_c'	1.803	> 2.6
ω_c	-0.1026	–
Modes	$\mathcal{D}'$	–
Bifurcation	Sub	–

Field and flow solutions for the most unstable mode can be seen in Figures 4.12 and 4.13.

Immediately, and as with the similar dipolar basic field result, we see that all azimuthal modes are heavily damped for $m \geq 2$. Appealing to Section 4.3.3 this phenomenon can be explained by ohmic diffusion. Unlike the corresponding case of Section 4.3.3, the $m = 1$ mode has been stabilised in the new field configuration.

The most unstable mode has retained its nonlinear development due to the geostrophic flow. The two V_G profiles (see Figure 4.8) for the quadrupole field and for the quadrupole field concentrating to the ICB are entirely different. For instance, the maximum modulus of V_G is attained at a radius of $s \cong 0.46$ unlike in Section 4.4.1 where the maximum occurs at $s = 1$. It would appear that the geostrophic flow tends to concentrate where the basic imposed field is strongest.

Observe that the addition of this section's quadrupolar modulation to a previously z-independent basic field [i.e. in Chapter 3, field (3.12)] has stabilised the system as was the case for basic field concentration to the CMB.

4.4.4 Comparison with the Aspect Ratio $\zeta = 1$

For the quadrupolar fields considered thus far, we have considered only aspect ratios of $\zeta = \pi/2$. As in Section 4.3.4 we modify the aspect ratio to $\zeta = 1$ in order for a more realistic comparison with the similar but viscous work of HF3.

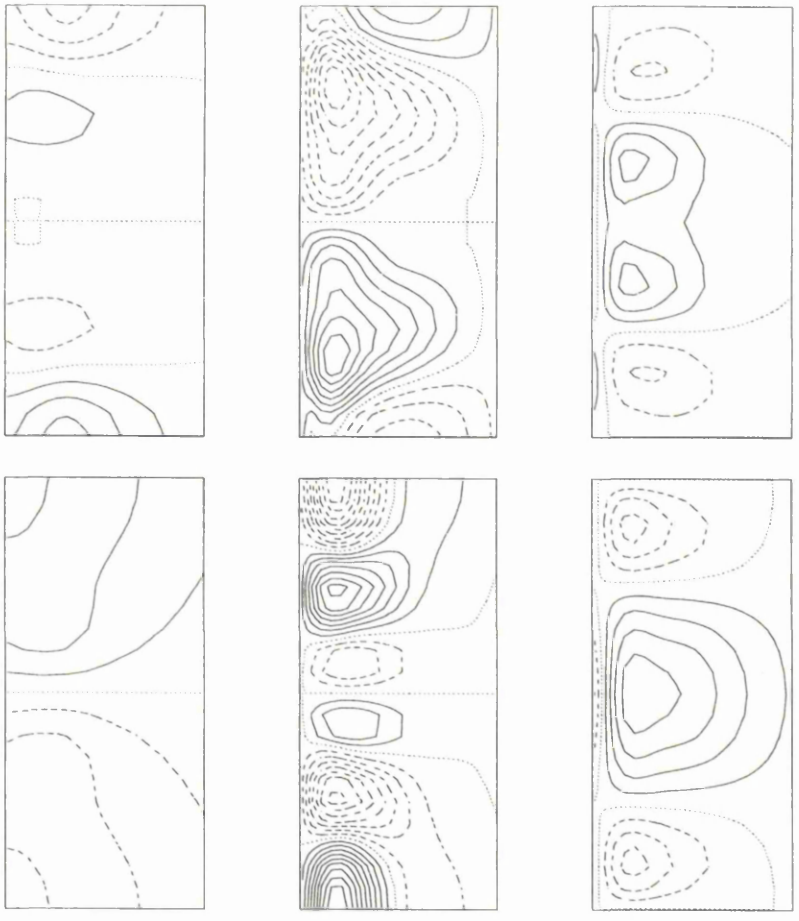

Figure 4.12: The perturbed field **b** is shown for the quadrupole field concentrating to the ICB: Top row, the real parts of (i) b_s, (ii) b_ϕ and (iii) b_z. The corresponding imaginary parts are shown in the bottom row. All plots share the same contour interval.

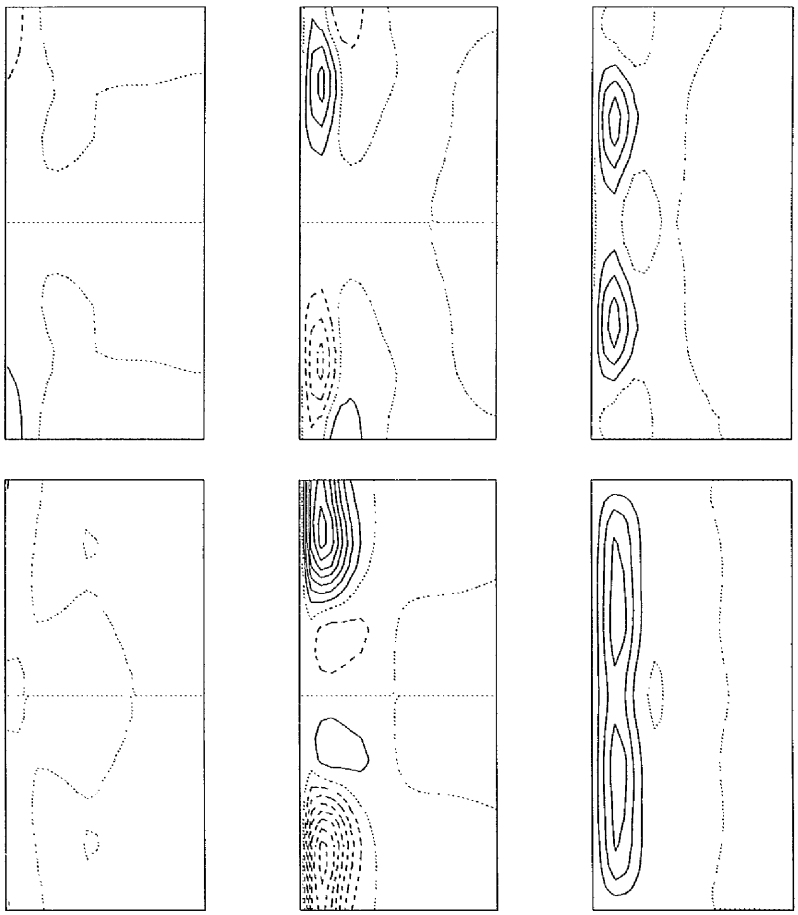

Figure 4.13: The perturbed flow field $\mathbf{v}$ is shown for the quadrupole field concentrating to the ICB: Top row, the real parts of (i) v_s, (ii) v_ϕ and (c) v_z. The corresponding imaginary parts are shown in the bottom row. All plots share the same contour interval.

Our basic state is the quadrupole field. The only difference between this section and Section 4.4.1 is that $\zeta = 1$. The results are tabulated in Table 4.10 along with the viscous parameter values which are reproduced courtesy of HF3 (italicised).

TABLE 4.10: Critical values for the aspect ratio 1 : 1. [HF3 italicised.]

m	1	2	3	4
Λ_c	17.73	10.10	7.984	7.878
	3.49	*2.06*	*3.02*	*6.80*
ω_c	−0.3820	−0.8397	−3.269	−8.699
	-0.29	*-0.28*	*0.25*	*1.04*
Modes	$\mathcal{D}'$	$\mathcal{D}'$	$\mathcal{D}'$	$\mathcal{D}'$
	Q'	Q'	Q'	Q'
Bifurcation	Sub	Sub	Sub	Sub
	Super	*Super*	*Super*	*Super*

On inspection of Table 4.10 we see what appears to be a qualitative difference between the viscous analyses at small Ekman number [$E = \mathrm{O}(10^{-4})$] and the magnetostrophic results. Like the dipole basic field results, we find the opposite solution symmetries for all our modes. This is consistent with the consistency condition (4.24). Had we been able to find the quadrupolar instability then the discrepancy between our results and those of HF3 may well have been resolved. As it is, in our model the most unstable mode is $m = 4$, whereas a viscous analysis shows $m = 2$ to be most unstable.

Let us now turn our attention to Table 4.7 and compare our magnetostrophic results across the aspect ratios. In changing ζ from $\pi/2$ to 1 there has only been a subtle change in the solution structure with the most unstable mode remaining the same. All the azimuthal modes have retained the same symmetry structure. For the most unstable mode, see Figures 4.7 and 4.8.

TABLE 4.11: Comparison of Λ_c' between aspect ratios.

Aspect Ratio ζ	$m=1$	$m=2$	$m=3$	$m=4$
1	2.660	1.515	1.198	1.182
$\pi/2$	1.761	0.9101	0.6447	0.6216

Changing the aspect ratio has had a strong stabilising on all the azimuthal modes (ohmic diffusion "sees" more structure over the smaller half-height) and the frequency has changed very little. Similarly, Figure 4.11 shows that after changing ζ from $\pi/2$ to 1, there has been little change in V_G. The geostrophic structure is more or less the same with, perhaps, a little more pronounced oscillation near $s \cong 0.95$.

4.5 Discussion

The work done in this chapter analysed the linear and nonlinear stability of a variety of dipolar and quadrupolar basic state fields. The magnetostrophic approximation was employed insofar as viscous boundary layers were retained on the flat bounding plates at $z = \pm\zeta$. The viscous drag from these boundary layers is balanced by the magnetic torque over concentric circular cylinders leading to a determination of the geostrophic flow. We showed in the Chapter 3 that the geostrophic flow is the first nonlinear effect to act on an exponentially growing solution to the linear problem. For z-independent basic field configurations we discovered subcritical instabilities for certain cases of basic fields and aspect ratios. In the viscous analyses of HF1,2 at finite Ekman number, $E = 10^{-4}$, no subcritical instabilities were found.

In this work we showed that a new constraint on the basic state field and magnetic instability must be satisfied. The axial component of the curl of the linearised Lorentz force must vanish when integrated over the height of the annular container. This is satisfied by any s-dependent basic state and its associated instability but only by certain s- and z-dependent basic fields and their associated instabilities. For example, a quadrupolar instability must accompany a dipolar azimuthal basic field and a dipolar instability must accompany a quadrupolar basic field to be certain that the consistency condition (4.24) is satisfied. For the other combinations of basic field and instability, any results obtained may or may not be consistent with (4.24)

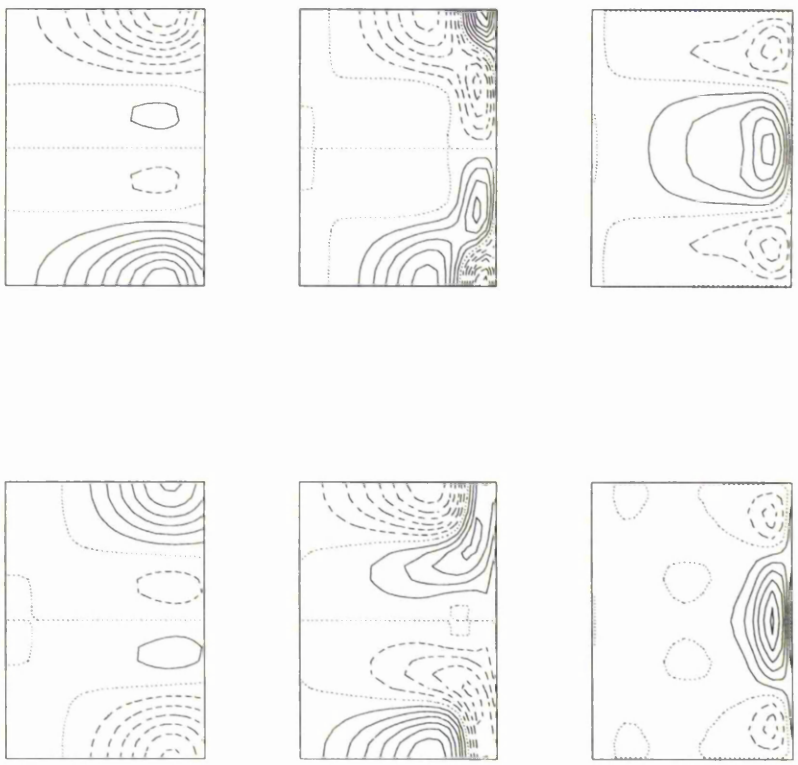

Figure 4.14: The perturbed field **b** for the most unstable mode of the quadrupole field with $F(s)$ taken from (4.2) and $G(z)$ taken from (4.7). Here $\zeta = 1$. Top row, the real parts of (i) b_s, (ii) b_ϕ and (iii) b_z. The corresponding imaginary parts are shown in the bottom row. All plots share the same contour interval.

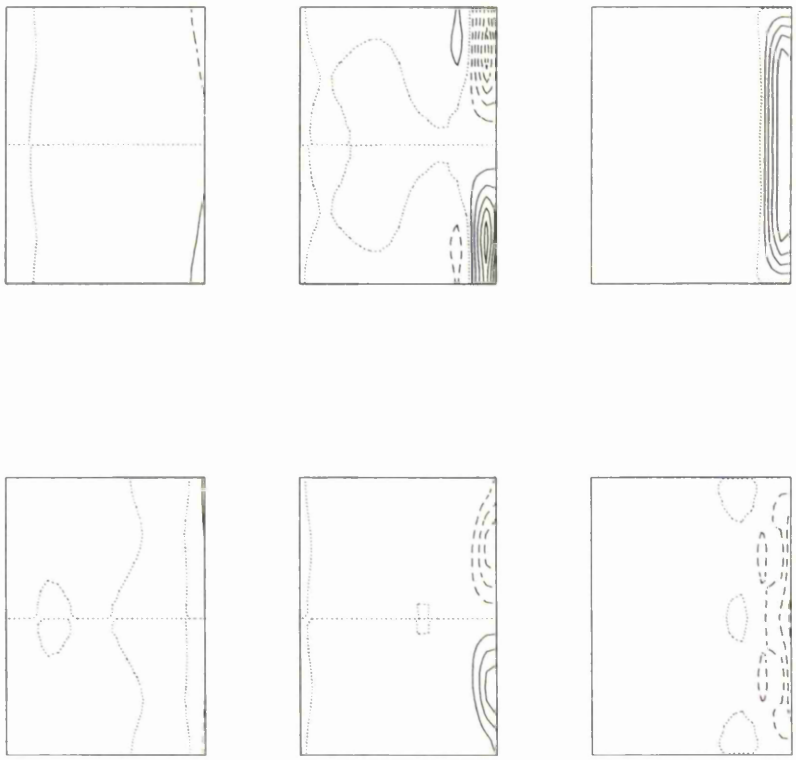

Figure 4.15: The perturbed flow field **v** for the most unstable mode of the quadrupole field with $F(s)$ taken from (4.2) and $G(z)$ taken from (4.7). Here $\zeta = 1$. Top row, the real parts of (i) v_s, (ii) v_ϕ and (iii) v_z. The imaginary parts are shown in the bottom row. All plots share the same contour interval.

and the restoration of some form of viscosity in the perturbation equations will be needed to resolve this problem.

In this work, we ask the question: do the magnetostrophic results of FLMO and Chapter 3 carry over to more geophysically realistic field configurations, and if so, how do the results compare with the corresponding viscous problem considered by HF3,4? To answer these questions, we used the energetic Elsasser number Λ' defined on a field's total magnetic energy [see (3.30)]. This allowed us to consistently compare the different basic fields of this work and the Chapter 3. The energetic Elsasser number Λ' is defined in.

Most of the computations carried out here ran on a Silicon Graphics R10000 Workstation. Although run times lasted, at most, half an hour, it usually took several runs to determine a single critical parameter value. Such values were found by starting with either arbitrary or "previous solution" initial conditions and time stepping long enough to establish growth or decay of the solution. Once the appropriate trend had been determined, the parameter values were varied and the process repeated. After two such computations were completed, a secant method could be applied in the remaining cycles to find the zeros Λ'_c of the growth rate of the magnetic energy $\sigma = \sigma(\Lambda')$.

The introduction of an axial dependence on to a z-independent basic field was found to have a destabilising effect for dipolar basic fields concentrating to the CMB and a stabilising effect for the dipole fields concentrating to the ICB and all quadrupolar basic fields. This result is intriguing in that the observed geomagnetic field exhibits a dipolar-type symmetry which can be more susceptible to magnetic instabilities than the quadrupole type. In each case of $\mathcal{D}$- and $\mathcal{Q}$-basic fields, given in sections 4.3.1 and 4.4.1, the most unstable mode was the $m = 4$ mode and its nonlinear bifurcation due to V_G was found to be subcritical.

Further to a stability analysis of just the basic dipolar or quadrupolar field symmetries, we introduced the ageostrophic magnetic wind into the problem, driven by the basic state field. The addition of $\mathbf{V}_M$ made no effect whatsoever except to mildly stabilise the instabilities and carry them along. For the most unstable mode, the solution structure with $\mathbf{V}_M$ was very similar to that without and the nonlinear development was unchanged.

A modification of $\zeta = \pi/2$ to 1 had an overall stabilising effect and the nonlinear bifurcation, due to V_G, of the most unstable mode remained unchanged under any basic field.

For stability analysis in the past, only certain forms of basic field have been considered. Specifically, those that concentrate field to the CMB. We have shown that $\mathcal{D}$- and $\mathcal{Q}$-fields concentrating to the ICB changes the most unstable mode. We have shown that the $m = 1$ instability becomes preferred as field concentrates more towards the ICB. This can be understood in terms of the amount of ohmic diffusion perceived by a mode as it approaches the axis of rotation. On comparison with the equivalent basic field concentrating to the CMB, fields concentrating to the ICB showed azimuthal modes becoming heavily damped by ohmic diffusion. The structure of these modes (apparently) increases by being compressed into a smaller region closer to the axis. What was surprising was that as the higher order modes were becoming stabilised, the $m = 1$ mode was *destabilised* under the $\mathcal{D}$-basic field.

One of the questions that we posed was as to whether the important qualitative difference between the viscous analysis of HF3 and the inviscid, magnetostrophic analysis of Chapter 3 or FLMO would carry over to more relevant field configurations. We must proceed cautiously at this point. We have neglected the effect of the induced mean poloidal field in the geostrophic flow where it can make an O(1) contribution. Future work will include this effect. The qualitative difference between our magnetostrophic results and the results of HF3 does still need resolution, however. Under the s- and z-dependent basic field configurations, only one instability parity could be examined (quadrupolar instabilities under a dipolar field or dipolar instabilities under a quadrupolar field). This problem is very serious in that it manifests itself in the *linear* regime. In order to find a resolution, some form of viscosity will need to be restored to the perturbation equations.

The non-axisymmetric geostrophic flow, which was implicitly calculated by HF3, has been neglected in our magnetostrophic analysis. In fact, the non-axisymmetric component of the geostrophic flow has *never* been included in a cylindrical, magnetostrophic analysis in the past. This fact alone may resolve the qualitative difference.

Although a cylindrical geometry initially seems more numerically tractable than the spherical geometry, we have found that it leads to hidden complications (in

both the linear and nonlinear regimes) that do not arise in the geophysically relevant spherical shell. The usefulness of cylindrical models in understanding the geodynamo is therefore at an end.

Chapter 5

Conclusions

In this thesis we have investigated three different problems. In Chapter 2 we formulated a linear hydromagnetic eigenvalue problem in the geometry of an infinite, cylindrical annulus. We focussed on purely s-dependent basic fields with no buoyancy forces to concentrate on purely magnetic instabilities. We explained two mechanisms that can lead to magnetic instability: the resistive instability and the ideal, or field gradient, instability. The former instability mechanism relies on magnetic diffusion for its existence and the latter works independently of diffusion and is driven by large gradients in the magnetic field. Much effort has been expended in the past in classifying magnetic instabilities as being of one or other class. However, we found that any mode classification is complicated due to the proximity of double and multiple eigenvalue points existing in the parameter space.

Jones (1987) examined and rigorously classified multiple eigenvalue points in a plane parallel (or Poiseuille) flow problem. He found that following an eigenmode around a closed path in the parameter space could lead to a change in eigenmode upon returning to the paths' starting point if that path enclosed a double eigenvalue point. We found that this phenomenon occurs in our simple magnetic stability problem. Furthermore, we found that tracking modes (and importantly, the most unstable modes) around closed loops in parameter space did not return the original eigenmode. In fact, we found numerous examples where resistive modes could be exchanged for ideal modes and vice versa. This means that any attempt at mode classification at geophysically relevant field strengths is not possible.

Chapters 3 and 4 examined the hydromagnetic stability of a variety of geophys-

ically relevant field profiles in a time stepping calculation. In Chapter 3 we verified and extended the magnetostrophic results of FLMO. There, in a finite cylindrical annular geometry with perfectly conducting top and bottom bounding plates and insulating cylindrical sidewalls, they used a linear and nonlinear eigenvalue method to examine the effects of a prescribed differential rotation and then of the nonlinear geostrophic flow on the onset and evolution of magnetic instability. Using their simple s-dependent basic fields and flows, we were able to verify that subcriticality can be achieved by choosing an appropriate differential rotation. FLMO found one case of subcriticality induced by the geostrophic flow. We found many examples where the geostrophic flow induced subcritical behaviour in the most unstable mode.

The important qualitative difference between the simple s-dependent work of Chapter 3 (and FLMO) and the viscous stability analysis of s-dependent basic states done by HF1,2 is that the presence of viscosity does not lead to subcriticality. In Chapter 4 we completed extensive modifications to our numerical code used in Chapter 3 in order to study the stability of basic fields depending on height as well as radius. We chose exactly the same field configurations as HF3,4 in our magnetostrophic analysis. Firstly, every calculation we executed found solutions that were (linearly) more stable and which exhibited the opposite parity to HF3. Secondly, and most importantly, subcritical behaviour was found for the most unstable mode in every example we looked at. In fact, in the twenty four examples investigated none exhibited supercritical behaviour. This has meant that no stable Ekman states could be found for the most unstable modes.

In Chapter 4 we discovered a new constraint that has to be satisfied in the cylindrical geometry in the linear regime. We showed that this consistency condition was always satisfied for s-dependent basic fields, but not always for s- and z-dependent basic states. The constraint is an important result in itself since, as we saw in the Introduction and Chapter 3, in the cylindrical geometry there was a *non-axisymmetric* component of the geostrophic flow. In the appropriate spherical geometry of the Earth, a non-axisymmetric component of the geostrophic flow is not permitted. This component, if included in our calculation, would have lead to a fully three dimensional problem by coupling the azimuthal modes. We decided that from a mathematical and geophysical viewpoint, little was to be gained by including

$V_G^s(s,\phi,t)\mathbf{1}_s + V_G^\phi(s,\phi,t)\mathbf{1}_\phi$ and consequently we set it to zero. It seems that the cylindrical geometry contains many hidden complications that do not carry over to the geophysically relevant spherical shell geometry and its usefulness as a tool in understanding the physics of the geodynamo may be at an end.

On comparison with the s-dependent work of Chapter 3, we found that in most cases the addition of a dipolar or quadrupolar modulation to a previously z-independent basic field was stabilising. The only exception to this result occurred when a dipolar modulation was given to the z-independent basic field (3.11) concentrating to the CMB.

It is perhaps not surprising that basic field morphology, such as field concentration to the inner core, should lead to variations in the onset and mode of instability. By introducing the "energetic Elsasser number" Λ' based on a field's total energy [see (3.30)] we were able to more realistically compare critical parameter values. Glatzmaier & Roberts (1995a,b) found in their dynamo calculations that much of the main magnetic field is strongest inside what is known as the "tangent cylinder" (an imaginary cylinder tangent to the Earth's inner core and parallel to the rotation axis). Upon examining the stability of basic fields which concentrate towards the ICB in our model, we found that magnetic instability is confined, by magnetic diffusion, to the lowest order azimuthal modes. Other effects, such as the inclusion of the ageostrophic magnetic wind (driven by the basic state) and variation in aspect ratio had little effect on magnetic instability (linear and nonlinear). In the end, the manifestation of instability is a trade-off between the effective amount of diffusion and the local energy density. We found instabilities present for geophysically relevant field strengths ($\Lambda \leq \mathrm{O}(10)$) and consequently, they must play an important role in the evolution of the main magnetic field.

More work is still needed to explain the qualitative difference between viscous and magnetostrophic results. The main difficulty with viscous calculations lies with the computationally small value of viscosity in the Earth's core. As computing power increases, it may now be possible to formulate a realistic viscous stability problem in a spherical geometry with no inner core. The absence of the inner core means that only one viscous boundary layer need be resolved and Ekman numbers of the order 10^{-8} may be approached. It still remains to be seen if this value will

lie in the correct asymptotic limit, but it might help begin to explain the qualitative difference. As regards other effects, it has not yet been ascertained whether or not restoring fluid inertia to the mean momentum equation (Jault, 1995) or incorporating thermal/compositional effects will lead to the same qualitative differences already observed in the magnetic stability problem. Certainly, subcritical behaviour has been discovered by Ogden (1997) who studied s-only or z-only dependent temperature profiles with a stable basic state field using the magnetostrophic approximation. A topic for future investigation would be to combine both unstable basic state fields and unstable temperature profiles in the more realistic spherical shell geometry.

References

Abramowitz, M. & Stegun, I.A., 1965. Handbook of Mathematical Functions. Dover, New York.

Acheson, D.J., 1972. On the hydromagnetic stability of a rotating fluid annulus. *J. Fluid Mech.* **52** 529–541.

Acheson, D.J., 1973. Hydromagnetic wavelike instabilities in a rapidly rotating stratified fluid. *J. Fluid Mech.* **61** 609-624.

Acheson, D.J., 1983. Local analysis of thermal and magnetic instabilities in a rapidly rotating fluid. *Geophys. & Astrophys. Fluid Dyn.* **27** 123-136.

Braginsky, S.I., 1963. Structure of the F layer and reasons for convection in the Earth's core. *Doklady Acad. NAUK SSSR* **149** 1311-1313 (English transl.: *Sov. Phys. Dokl.* **149** 8-10.)

Busse, F.H., 1970. Thermal instabilities in rapidly rotating systems. *J. Fluid Mech.* **44** 441-460.

Cowling, T.G., 1934. The magnetic field of sunspots. *Mon. Not. R. Astr. Soc.* **94** 39-48.

Fearn, D.R., 1979b. Thermal and magnetic instabilities in a rapidly rotating fluid sphere. *Geophys. Astrophys. Fluid Dyn.* **14** 103-126.

Fearn, D.R., 1983a. Boundary conditions for a rapidly rotating hydromagnetic system in a cylindrical container, Geophys. Astrophys. Fluid Dyn. **25** 65-75.

Fearn, D.R., 1983b. Hydromagnetic waves in a differentially rotating annulus I. A test of local stability analysis. *Geophys. Astrophys. Fluid Dyn.* **27** 137-162.

Fearn, D.R., 1984. Hydromagnetic waves in a differentially rotating annulus II. Resistive Instabilities. *Geophys. Astrophys. Fluid Dyn.* **30** 227-239.

Fearn, D.R., 1985. Hydromagnetic waves in a differentially rotating annulus III. The affect of an axial field. *Geophys. Astrophys. Fluid Dyn.* **33** 185-197.

Fearn, D.R., 1988 Hydromagnetic waves in a differentially rotating annulus IV. Insulating boundaries. *Geophys. Astrophys. Fluid Dyn.* **44** 55-75.

Fearn, D.R., 1990. Eigensolutions of boundary value problems using inverse iteration. *J. Comp. Appl. Math.* **34** 201-209.

Fearn, D.R., 1994. Nonlinear Planetary Dynamos, In: M.R.E. Proctor & A.D. Gilbert (Editors), *Lectures on Solar and Planetary Dynamos.* Cambridge University Press, pp. 219-244.

Fearn, D.R., 1997. The geodynamo, In: D. Crossley (Editor), *Earth's Deep Interior.* Gordon and Breach, London, pp. 79-114

Fearn, D.R., 1997. Hydromagnetic flow in planetary cores. *Rep. Prog. Phys.* Submitted.

Fearn, D.R. & Proctor, M.R.E., 1983a. Hydromagnetic waves in a differentially rotating sphere. *J. Fluid Mech.* **128** 1-20.

Fearn, D.R. & Proctor, M.R.E., 1983b. The stabilising role of differential rotation on hydromagnetic waves. *J. Fluid Mech.* **128** 21-36.

Fearn, D.R. & Proctor, M.R.E., 1987. Dynamically consistent magnetic fields produced by differential rotation. *J. Fluid Mech.* **178** 521-534.

Fearn, D.R. & Proctor, M.R.E. & Sellar, C.C., 1994. Nonlinear magnetoconvection in a rapidly rotating sphere and Taylors' constraint. *Geophys. Astrophys. Fluid Dynam.* **77** 111-132.

Fearn, D.R., Lamb, C.J., McLean, D.R. & Ogden, R.R., 1997. The influence of differential rotation on magnetic instability and nonlinear magnetic instability in the magnetostrophic limit. *Geophys. Astrophys. Fluid Dyn.* **86** 173-200.

Gilbert, W., 1600. De Magnete. Dover, New York. (1958). (English transl.: P. Fleury Mottelay, 1893.)

Glatzmaier, G.A. & Roberts, P.H., 1995a. A three-dimensional convective dynamo solution with rotating and finitely conducting inner core and mantle. *Phys. Earth Planet. Inter.* **91** 63-75.

Glatzmaier, G.A. & Roberts, P.H., 1995b. A three-dimensional self-consistent computer simulation of a geomagnetic field reversal. *Nature* **377** 203-209.

Glatzmaier, G.A. & Roberts, P.H., 1996. Rotation and magnetism of the Earth's inner core. *Science* **274** 1887-1891

Glatzmaier, G.A., & Roberts, P.H., 1997. Simulating the geodynamo. *Contemp. Phys.* **38** 269-288.

Gubbins, D. & Zhang, K., 1993. Symmetry properties of the dynamo equations for palaeomagnetism and geomagnetism. *Phys. Earth Planet. Inter.* **75** 225-241.

Hollerbach, R., 1994. Imposing a magnetic field across a nonaxisymmetric shear layer in a rotating spherical shell. *Phys. Fluids* **6** 2540-2544.

Hollerbach, R., 1996. On the theory of the Geodynamo. *Phys. Earth Planet. Inter.* **98** 163-185.

Hollerbach R, & Jones, C.A., 1993a. A geodynamo model incorporating a finitely conducting inner core. *Phys. Earth Planet. Inter.* **75** 317-327.

Hollerbach R, & Jones, C.A., 1993b. Influence of the Earth's inner core on geomagnetic fluctuations and reversals. *Nature* **365** 541-543.

Hollerbach R, & Jones, C.A., 1995. on the magnetically stabilising role of the Earth's inner core. *Phys. Earth Planet. Inter.* **87** 171-181.

Hollerbach R, & Proctor, M.R.E., 1993. Non-axisymmetric shear layers in a rotating spherical shell. In: M.R.E. Proctor, P.C. Matthews and A.M. Rucklidge (Editors), *Solar and Planetary Dynamos.* Cambridge University Press, 145-152.

Hollerbach R, Galloway, D.J., & Proctor, M.R.E., 1995. Numerical evidence of fast dynamo action in a spherical shell. *Phys. Rev. Lett.* **74** 3145-3148.

Hutcheson, K.A. & Fearn, D.R., 1995a. The nonlinear evolution of magnetic instabilities in a rapidly rotating annulus. *J. Fluid Mech.* **291** 343-368.

Hutcheson, K.A. & Fearn, D.R., 1995b. Nonlinear stability of the geomagnetic field. *Geophys. Res. Lett.* **22** 1637-1640.

Hutcheson, K.A. & Fearn, D.R., 1996. The stability of toroidal magnetic fields with equatorial symmetry: implications for the Earth's magnetic field. *Phys. Earth*

Planet. Inter. **97** 43-54.

Hutcheson, K.A. & Fearn, D.R., 1997. The stability of toroidal magnetic fields with equatorial symmetry: evolution of instabilities. *Phys. Earth Planet. Inter.* **99** 19-32.

Jault, D., 1995. Model Z by computation and Taylor's condition. *Geophys. Astrophys. Fluid Dyn.* **79** 99-124.

Jones, C.A., 1987. Multiple eigenvalues and mode classification in plane Poiseuille flow. *Q. Jl Mech. appl. Math.* **41** 364-382.

Kerswell, R.R., 1994. Tidal excitation of hydromagnetic-waves and their damping in the Earth. *J. Fluid Mech.* **274** 219-241.

Kerswell, R.R., 1996. Upper-bounds on the energy-dissipation in turbulent precession. *J. Fluid Mech.* **321** 335-370.

Kuang, W., & Bloxham, J., 1997. An Earth-like numerical dynamo model. *Nature* In press.

Kuang, W., & Bloxham, J., 1997. An Earth-like numerical dynamo model. Numerical modelling of magnetohydrodynamic convection in a rapidly rotating spherical shell: Weak and Strong field dynamo action. *J. Comp. Phys.* Submitted.

Larmor, J., 1919. How could a rotating body such as the Sun become a magnet? *Rep. Br. Assoc. Adv. Sci.* A 159-160.

Lister, R.L. & Buffett, B.A., 1995. The strength and efficiency of thermal and compositional convection in the geodynamo. Phys. Earth Planet. Inter. **91** 17-30.

Malkus, W.V.R. & Proctor, M.R.E., 1975. The macrodynamics of α-effect dynamos in rotating fluids. *J. Fluid Mech.* **67** 417-443.

McLean, D.R., & Fearn, D.R., 1996. The classification of magnetic instabilities. *Geophys. Astrophys. Fluid Dynam.* **82** 221-236.

Ogden, R.R., 1997. Thermal instabilities in a rapidly rotating system. Ph.D Thesis. Department of Mathematics, University of Glasgow.

Roberts, P.H. & Soward, A.M., 1992. Dynamo theory. *Ann. Rev. Fluid Mech.* **24** 459-512.

Secco, R.A. & Schloessin, H.H., 1989. The electrical-resistivity of solid and liquid Fe at pressures up to 7-G Pa. *J. Geophys. Res.* **94** 5887-5894.

Skinner, P.H. & Soward, A.M., 1988. Convection in a rotating magnetic system and Taylor's constraint. *Geophys. Astrophys. Fluid Dyn.* **44** 91-116.

Skinner, P.H. & Soward, A.M., 1990. Convection in a rotating magnetic system and Taylor's constraint: Part II, Numerical results. *Geophys. Astrophys. Fluid Dyn.* **60** 335-356.

Song, X. & Richards, P.G., 1996. Seismological evidence for differential rotation of the Earth's inner core. *Nature* **382** 221-224.

Soward, A.M., 1991. The Earth's dynamo. *Geophys. Astrophys. Fluid Dyn.* **62** 191-209.

Su, W., Dzeiwonski, A.M. & Jeanloz, R., 1996. Planet Within a Planet: Rotation of the Inner Core of Earth. *Science* **274** 1883-1887.

Taylor, J.B., 1963. The magnetohydrodynamics of a rotating fluid and the Earth's dynamo problem. *Proc. R. Soc. London* Ser. A, **274** 274-283.

Verhoogen, J., 1961. Energetics of the Earth. *Geophys. J. R. Astr. Soc.* 4 276-281

Whaler, K. & Holme, R., 1996. Catching the inner core in a spin. *Nature* **382** 205-206.

Zhang, K., 1995b. Spherical-shell rotating convection in the presence of a toroidal magnetic field. *Proc. R. Soc. Lond. A* **448** 245-268.

Zhang, K. & Fearn, D.R., 1994. Hydromagnetic waves in rapidly rotating spherical shells generated by magnetic toroidal decay modes. *Geophys. Astrophys. Fluid Dyn.* **77** 133-157.

Zhang, K. & Fearn, D.R., 1995. Hydromagnetic waves in rapidly rotating spherical shells generated by magnetic poloidal decay modes. *Geophys. Astrophys. Fluid Dyn.* **81** 193-209.

Appendix A

Boundary Conditions

In solving the nonlinear problem in chapters 3 and 4, we expanded the field and flow in terms of an axisymmetric basic state and a non-axisymmetric perturbation

$$\begin{aligned} \mathbf{B}(s,\phi,z,t) &= \mathbf{B}_0(s,z) + \mathbf{b}(s,\phi,z,t), \\ \mathbf{V}(s,\phi,z,t) &= \mathbf{V}_0(s,z) + \mathbf{v}(s,\phi,z,t). \end{aligned}$$

These were then substituted into the momentum and induction equations retaining the geostrophic flow V_G as the only nonlinearity.

Under the magnetostrophic approximation the governing equations drop from being tenth order in s to fourth order. This complicates the choice of boundary conditions along the curved annular sidewalls. Firstly, all normal components of the flow must vanish along the surfaces $s = s_{\rm ib}, 1$. Secondly, for the magnetic field, perfect electrical insulators inhabit the regions exterior to the annulus: $s < s_{\rm ib}$ and $s > 1$. Thirdly, along the insulating sidewalls there must be no normal current and the field interior to the annulus must match to an external potential field. This requires six conditions to be satisfied on $s = s_{\rm ib}, 1$ when the differential order in s is only 4. Fortunately, Fearn (1983a) has shown that the two no-normal-flow conditions on the sidewalls can be met with the addition of a viscous layer. This leaves us free to enforce no-normal-current flow and to match the interior field to an external potential field at $s = s_{\rm ib}, 1$.

On $z = \pm\zeta$, the boundary conditions are the no normal flow and perfect electrical conductor conditions:

$$\mathbf{n}\cdot\mathbf{v} = 0,\ \mathbf{n}\cdot\mathbf{b} = 0 \text{ and } \mathbf{n}\times\mathbf{e} = 0 \quad \text{on} \quad z = \pm\zeta. \tag{A.1}$$

Written here in its dimensional form, Ohm's law allows us to eliminate the pertubed electric field $\mathbf{e}^*$:

$$\mathbf{e}^* = \sigma^{-1}\mathbf{j}^* - \mathbf{v}^* \times \mathbf{B}_0^* = \eta\nabla^* \times \mathbf{b}^* - \mathbf{v}^* \times \mathbf{B}_0^*,$$

where σ is the electrical conductivity and $\mathbf{j}^*$ is the perturbed current density. From the boundary condition on the electric field, we then have

$$\frac{1}{s}\left(\frac{\partial b_z}{\partial \phi} - s\frac{\partial b_\phi}{\partial z}\right) + u_z B_0 = 0.$$

However, at either top or bottom boundary the normal component of flow must vanish. Therefore

$$\frac{\partial b_z}{\partial \phi} = s\frac{\partial b_\phi}{\partial z}.$$

For the boundary conditions on the perfectly conducting plates at $z = \pm\zeta$, a Galerkin technique is employed.

$$X(s,\phi,z,t) = \sum_{n=n_0}^{NZ} X_{s,n}(s,t)\cos\bar{n}(z+\zeta)e^{im\phi} + \text{CC}, \tag{A.2}$$

$$Y(s,\phi,z,t) = \sum_{n=n_0}^{NZ} Y_{z,n}(s,t)\sin\bar{n}(z+\zeta)e^{im\phi} + \text{CC} \tag{A.3}$$

where X represents any of v_s, v_ϕ, b_s or b_ϕ and Y represents either v_z or b_z. The variable $\bar{n} = n\pi/2\zeta$ where $0 \le n_0 \le n \le NZ$. In Chapter 3 we set $NZ = n_0 > 0$ in order to consider purely s-dependent basic states whereas in Chapter 4 $n_0 = 0$ and $NZ = 8$ with s- and z-dependent basic fields under examination.

Consider the regions exterior to the annular volume. The regions $0 \le s \le s_{\text{ib}}$ and $s \ge s_{\text{ib}}$ are solid insulators and there can be no flows or currents present. Therefore, from Maxwell's equations we find $\nabla \times \mathbf{b} = 0$ in $s < s_{\text{ib}}$ and $s > 1$. Consequently, the exterior magnetic field $\mathbf{b}^e$ may be described by a magnetostatic scalar potential field $U = U(s,\phi,z)$

$$\mathbf{b}^e = -\nabla U. \tag{A.4}$$

Using the divergence free condition, U must satisfy Laplace's equation $\nabla^2 U = 0$.

$$\frac{\partial^2 U}{\partial s^2} + \frac{1}{s}\frac{\partial U}{\partial s} + \frac{1}{s^2}\frac{\partial^2 U}{\partial \phi^2} + \frac{\partial^2 U}{\partial z^2} = 0. \tag{A.5}$$

Let

$$U(s,\phi,z) = \sum_{n=n_0}^{N_0} U_n(s)\cos\bar{n}(z+\zeta)e^{im\phi}. \tag{A.6}$$

Then (A.5) reduces to solving the $N_0 - n_0 + 1$ o.d.e's

$$[s^2D^2 + sD - (m^2 + \bar{n}^2 s^2)]U_n(s) = 0 \quad \text{for} \quad 0 \leq n_0 \leq n \leq N_0. \tag{A.7}$$

First of all, let us consider the case where $n = 0$ as it is a little different from the cases $n > 0$. Here (A.7) becomes

$$[s^2D^2 + sD - m^2]U_0 = 0. \tag{A.8}$$

Thus, seeking solutions of the form $U_0(s) \propto s^\gamma$ yields the condition

$$\gamma(\gamma - 1) + \gamma - m^2 = 0 \quad \Leftrightarrow \quad \gamma = \pm m\,.$$

Hence the general solution of (A.8) must be

$$U_0(s) = As^m + Bs^{-m}\,.$$

Now, for $s \in (0, s_{\text{ib}})$ the solution must remain finite in the limit $s \to 0$ and so $U_0(s) = As^m$ $(B \equiv 0)$. The potential U_0 is related to the field via

$$b^e_{s,0} = -DU_0$$

and so $b^e_{s,0} = -Ams^{m-1}$ which leads to $sb^e_{s,0}(= -Ams^m) = -mU_0$. Differentiating and eliminating U_0 leads to the boundary condition on the zeroth axial mode. An exactly similar analysis on the region $s > 1$ gives the match condition on the surface $s = 1$. The conditions are

$$sDb_{s,0} + (1 - m)b_{s,0} = 0 \quad \text{on } s = s_{\text{ib}}, \tag{A.9}$$

$$sDb_{s,0} + (1 + m)b_{s,0} = 0 \quad \text{on } s = 1. \tag{A.10}$$

For $n > 0$ the o.d.e's (A.7) have solutions

$$U_n(s) = A_n I_m(\bar{n}s) + C_n I_m(\bar{n}s) \tag{A.11}$$

where A_n and C_n are constants and I_m and K_m are modified Bessel functions. In the region $0 \leq s \leq s_{\text{ib}}$ we require $C_n = 0$ and in $s \geq s_{\text{ib}}$ we need $A_n = 0$ to ensure a physical solution.

On either annular surface we require that the interior magnetic field $\mathbf{b}$ match to the external potential field $\mathbf{b}^e$. From (A.4) we have,

$$b_s = -\frac{\partial U}{\partial s}, \quad b_\phi = -\frac{1}{s}\frac{\partial U}{\partial \phi} \quad \text{and} \quad b_z = -\frac{\partial U}{\partial z}. \tag{A.12}$$

Using (A.6) we have for $n_0 \leq n \leq N_0$

$$b_{s,n}(s,t) = -DU_n(s), \quad b_{\phi,n}(s,t) = -imU_n(s) \quad \text{and} \quad b_{z,n}(s,t) = \bar{n}U_n(s). \quad \text{(A.13)}$$

Using the identity

$$\mathcal{L}'_m(\bar{n}s) = \mathcal{L}_{m+1}(\bar{n}s) + \frac{m}{s}\mathcal{L}_m(\bar{n}s) \quad \text{(A.14)}$$

(see Abramowitz and Stegun, 1965, Ch.9, p376) where $\mathcal{L}$ stands for either of I_m or $e^{im\pi}K_m$ (or any linear combination) then it is easy to see that the match condition following from (A.14) becomes

$$b_{s,n}(s,t) = \gamma_n b_{z,n}(s,t) \quad \text{for} \quad 1 \leq n_0 \leq n \leq N_0. \quad \text{(A.15)}$$

where

$$\gamma_n = \begin{cases} -\left[\dfrac{I_{m+1}(\bar{n}s_{\text{ib}})}{I_m(\bar{n}s_{\text{ib}})} + \dfrac{m}{\bar{n}s_{\text{ib}}}\right] & \text{if } s = s_{\text{ib}}, \\ \\ \left[\dfrac{K_{m+1}(\bar{n})}{K_m(\bar{n})} - \dfrac{m}{\bar{n}s_{\text{ib}}}\right] & \text{if } s = 1 \end{cases} \quad \text{(A.16)}$$

where $\bar{n} = n\pi/2\zeta$, $n_0 \leq n \leq N_0$.

For the condition that there be no normal current flow across either boundary, $j_s = (\nabla \times \mathbf{b})_s = 0$ requires that

$$\frac{1}{s}\frac{\partial b_z}{\partial \phi} - \frac{\partial b_\phi}{\partial z} = 0 \quad \text{on} \quad s = s_{\text{ib}}, 1. \quad \text{(A.17)}$$

Using $\nabla \cdot \mathbf{b} = 0$ to obtain an expression for b_ϕ in terms of b_s and b_z we substitute this back into (A.17) and obtain

$$s^2 D b_{s,n} + s b_{s,n} + [\bar{n}^2 s^2 + m^2] b_{z,n}/\bar{n} = 0 \quad \text{on} \quad s = s_{\text{ib}}, 1 \quad \text{for} \quad 1 \leq n_0 \leq n \leq N_0. \quad \text{(A.18)}$$

Appendix B

Perturbation Equations

The equations governing the evolution of nonaxisymmetric magnetic field and flow perturbations $\mathbf{b}$ and $\mathbf{u}$ to an axisymmetric basic state $\mathbf{B}_0 = \hat{B}(s,z)\mathbf{1}_\phi$ and $\mathbf{V}_0 = \hat{V}(s,z)\mathbf{1}_\phi$ are

$$\mathbf{1}_z \times \mathbf{v} = -\nabla\pi + (\nabla \times \mathbf{B}_0) \times \mathbf{b} + (\nabla \times \mathbf{b}) \times \mathbf{B}_0,$$

$$\frac{\partial \mathbf{b}}{\partial t} = \nabla \times (\mathbf{v} \times \mathbf{B}_0) + \nabla \times (\mathbf{V}_0 \times \mathbf{b}) + \Lambda^{-1}\nabla^2\mathbf{b}$$

where the basic state field is decomposed as $\hat{B} = sF(s)G(z)$. The term $\mathbf{V}_0 = \hat{V}(s,z)\mathbf{1}_\phi$ represents either a basic state flow, $\hat{V} = sF^\Omega(s)G^\Omega(z)$ or the geostrophic flow $\hat{V} = V_G(s)$ depending on whether the linear or nonlinear problem is being solved. The incompressibility and solenoidal equations are:

$$\nabla \cdot \mathbf{v} = 0, \ \nabla \cdot \mathbf{b} = 0.$$

In their component form, the perturbation equations are then:

- The s–momentum equation:

$$v_\phi = \frac{\partial \pi}{\partial s} + \frac{b_\phi}{s}\left(2\hat{B} + s\frac{\partial \hat{B}}{\partial s}\right) - \frac{\hat{B}}{s}\frac{\partial b_s}{\partial \phi} + \hat{B}\frac{\partial b_\phi}{\partial s}. \tag{B.1}$$

- The ϕ–momentum equation:

$$v_s = -\frac{1}{s}\frac{\partial \pi}{\partial \phi} + \frac{b_s}{s}\left(\hat{B} + s\frac{\partial \hat{B}}{\partial s}\right) + b_z\frac{\partial \hat{B}}{\partial z}. \tag{B.2}$$

- The z–momentum equation:

$$0 = \frac{\partial \pi}{\partial z} + b_\phi\frac{\partial \hat{B}}{\partial z} - \frac{\hat{B}}{s}\frac{\partial b_z}{\partial \phi} + \hat{B}\frac{\partial b_\phi}{\partial z}. \tag{B.3}$$

- The s–induction equation:

$$\frac{\partial b_s}{\partial t} = \frac{\hat{B}}{s}\frac{\partial v_s}{\partial \phi} - \frac{\hat{V}}{s}\frac{\partial b_s}{\partial \phi} + \frac{1}{\Lambda}\left(\frac{1}{s}\frac{\partial b_s}{\partial s} + \frac{\partial^2 b_s}{\partial s^2} + \frac{1}{s^2}\frac{\partial^2 b_s}{\partial \phi^2} + \frac{\partial^2 b_s}{\partial z^2} - \frac{b_s}{s^2} - \frac{2}{s^2}\frac{\partial b_\phi}{\partial \phi}\right). \tag{B.4}$$

- The ϕ–induction equation:

$$\begin{aligned}\frac{\partial b_\phi}{\partial t} &= -\frac{\partial \hat{B}}{\partial s}v_s - \hat{B}\frac{\partial v_s}{\partial s} - \frac{\partial \hat{B}}{\partial z}v_z - \hat{B}\frac{\partial v_z}{\partial z} + \frac{\partial}{\partial s}(\hat{V}b_s) + \frac{\partial}{\partial z}(\hat{V}b_z) \\ &\quad + \frac{1}{\Lambda}\left(\frac{1}{s}\frac{\partial b_\phi}{\partial s} + \frac{\partial^2 b_\phi}{\partial s^2} + \frac{1}{s^2}\frac{\partial^2 b_\phi}{\partial \phi^2} + \frac{\partial^2 b_\phi}{\partial z^2} - \frac{b_\phi}{s^2} + \frac{2}{s^2}\frac{\partial b_s}{\partial \phi}\right).\end{aligned} \tag{B.5}$$

- The z–induction equation:

$$\frac{\partial b_z}{\partial t} = \frac{\hat{B}}{s}\frac{\partial v_z}{\partial \phi} - \frac{\hat{V}}{s}\frac{\partial b_z}{\partial \phi} + \frac{1}{\Lambda}\left(\frac{1}{s}\frac{\partial b_z}{\partial s} + \frac{\partial^2 b_z}{\partial s^2} + \frac{1}{s^2}\frac{\partial^2 b_z}{\partial \phi^2} + \frac{\partial^2 b_z}{\partial z^2}\right). \tag{B.6}$$

- The incompressibility and solenoidal conditions:

$$\frac{v_s}{s} + \frac{\partial v_s}{\partial s} + \frac{1}{s}\frac{\partial v_\phi}{\partial \phi} + \frac{\partial v_z}{\partial z} = 0, \tag{B.7}$$

$$\frac{b_s}{s} + \frac{\partial b_s}{\partial s} + \frac{1}{s}\frac{\partial b_\phi}{\partial \phi} + \frac{\partial b_z}{\partial z} = 0. \tag{B.8}$$

Firstly, we take the linearised perturbation equations (B.1)–(B.8) and eliminate the (perturbed) variables π, v_ϕ and b_ϕ. More precisely, π is eliminated by differentiating the ϕ–induction equation, (B.2), w.r.t. s and z and then differentiating (B.1) and (B.3) by ϕ and subtracting. In the resulting two equations, any reference to v_ϕ or b_ϕ is eliminated on using the incompressibility and solenoidal conditions, respectively. In the same manner, we take (B.4) and (B.5) and eliminate any reference to v_ϕ or b_ϕ. The ϕ-induction equation is ignored, the justification being that we have eight governing equations (three scalar momentum equations, three scalar magnetic induction equations and one solenoidal equation) and only seven unknowns ($\pi, v_s, v_\phi, v_z, b_s, b_\phi$ and b_z). Our system of equations is thus linearly dependent. We therefore choose to ignore the ϕ induction equation in favour of the solenoidal equation (B.8).

On elimination of π, v_ϕ and b_ϕ we have the following equations:

$$\begin{aligned}s\frac{\partial v_z}{\partial z} &= \left[\frac{2\hat{B}}{s} - \frac{\partial \hat{B}}{\partial s} - s\frac{\partial^2 \hat{B}}{\partial s^2}\right]b_s - \left[\frac{\partial \hat{B}}{\partial z} + s\frac{\partial^2 \hat{B}}{\partial s \partial z}\right]b_z + \left[3\hat{B} + s\frac{\partial \hat{B}}{\partial s}\right]\frac{\partial b_z}{\partial z} \\ &\quad + 3\hat{B}\frac{\partial b_s}{\partial s} - s\frac{\partial \hat{B}}{\partial z}\frac{\partial b_z}{\partial s} + s\hat{B}\frac{\partial^2 b_s}{\partial s^2} + s\hat{B}\frac{\partial^2 b_z}{\partial s \partial z} + \frac{\hat{B}}{s}\frac{\partial^2 b_s}{\partial \phi^2}\end{aligned} \tag{B.9}$$

$$s\frac{\partial v_s}{\partial z} = s\frac{\partial^2 \hat{B}}{\partial s \partial z} b_s + s\frac{\partial^2 \hat{B}}{\partial z^2} b_z - s\frac{\partial \hat{B}}{\partial z}\frac{\partial b_s}{\partial s} + s\frac{\partial \hat{B}}{\partial s}\frac{\partial b_s}{\partial z} - \frac{\hat{B}}{s}\frac{\partial^2 b_z}{\partial \phi^2} - s\hat{B}\frac{\partial^2 b_s}{\partial s \partial z} - s\hat{B}\frac{\partial^2 b_z}{\partial z^2} \tag{B.10}$$

$$\frac{\partial b_s}{\partial t} = \frac{\hat{B}}{s}\frac{\partial v_s}{\partial \phi} - \frac{\hat{V}}{s}\frac{\partial b_s}{\partial \phi} + \frac{1}{\Lambda}\left(\frac{3}{s}\frac{\partial b_s}{\partial s} + \frac{\partial^2 b_s}{\partial s^2} + \frac{1}{s^2}\frac{\partial^2 b_s}{\partial \phi^2} + \frac{\partial^2 b_s}{\partial z^2} + \frac{b_s}{s^2} + \frac{2}{s}\frac{\partial b_z}{\partial z}\right), \tag{B.11}$$

$$\frac{\partial b_z}{\partial t} = \frac{\hat{B}}{s}\frac{\partial v_z}{\partial \phi} - \frac{\hat{V}}{s}\frac{\partial b_z}{\partial \phi} + \frac{1}{\Lambda}\left(\frac{1}{s}\frac{\partial b_z}{\partial s} + \frac{\partial^2 b_z}{\partial s^2} + \frac{1}{s^2}\frac{\partial^2 b_z}{\partial \phi^2} + \frac{\partial^2 b_z}{\partial z^2}\right). \tag{B.12}$$

By making substitutions of the form $w(s,\phi,z,t) = \hat{w}(s,z,t)e^{im\phi}$ for v_s, v_z, b_s and b_z we eliminate the ϕ-dependence from (B.9)-(B.12). Dropping the hats, the results are:

$$\frac{\partial v_z}{\partial z} = \left[\frac{\hat{B}}{s^2}(2-m^2) - \frac{1}{s}\frac{\partial \hat{B}}{\partial s} - \frac{\partial^2 \hat{B}}{\partial s^2}\right] b_s - \left[\frac{1}{s}\frac{\partial \hat{B}}{\partial z} + \frac{\partial^2 \hat{B}}{\partial s \partial z}\right] b_z + \left[\frac{3}{s}\hat{B} + \frac{\partial \hat{B}}{\partial s}\right]\frac{\partial b_z}{\partial z} + \frac{3\hat{B}}{s}\frac{\partial b_s}{\partial s} - \frac{\partial \hat{B}}{\partial z}\frac{\partial b_z}{\partial s} + \hat{B}\frac{\partial^2 b_s}{\partial s^2} + \hat{B}\frac{\partial^2 b_z}{\partial s \partial z} \tag{B.13}$$

$$\frac{\partial v_s}{\partial z} = \frac{\partial^2 \hat{B}}{\partial s \partial z} b_s + \left[\frac{m^2 \hat{B}}{s^2} + \frac{\partial^2 \hat{B}}{\partial z^2}\right] b_z - \frac{\partial \hat{B}}{\partial z}\frac{\partial b_s}{\partial s} + \frac{\partial \hat{B}}{\partial s}\frac{\partial b_s}{\partial z} - \hat{B}\frac{\partial^2 b_s}{\partial s \partial z} - \hat{B}\frac{\partial^2 b_z}{\partial z^2} \tag{B.14}$$

$$\frac{\partial b_s}{\partial t} = im\frac{\hat{B}}{s}v_s - im\frac{\hat{V}}{s}b_s + \frac{1}{\Lambda}\left(\frac{3}{s}\frac{\partial b_s}{\partial s} + \frac{\partial^2 b_s}{\partial s^2} + \frac{1}{s^2}(1-m^2)b_s + \frac{\partial^2 b_s}{\partial z^2} + \frac{2}{s}\frac{\partial b_z}{\partial z}\right), \tag{B.15}$$

$$\frac{\partial b_z}{\partial t} = im\frac{\hat{B}}{s}v_z - im\frac{\hat{V}}{s}b_z + \frac{1}{\Lambda}\left(\frac{1}{s}\frac{\partial b_z}{\partial s} + \frac{\partial^2 b_z}{\partial s^2} - \frac{m^2}{s^2}b_z + \frac{\partial^2 b_z}{\partial z^2}\right). \tag{B.16}$$

The form we choose for the s– and z–dependent basic state field $\mathbf{B}_0 = \hat{B}(s,z)\mathbf{1}_\phi$ is $\hat{B}(s,z) = sF(s)G(z)$ and for the flow $\hat{V}(s,z) = sF^\Omega(s)G^\Omega(z)$ for real valued functions F, F^Ω and G, G^Ω. Note that in the case $\hat{V} = V_G$ then $G^\Omega \equiv 1$. Results that are required involving the derivatives of $\hat{B}$ are:

$$\frac{\partial \hat{B}}{\partial s} = G(z)[F(s) + sD_sF(s)], \tag{B.17}$$

$$\frac{\partial \hat{B}}{\partial z} = sF(s)\,D_zG(z), \tag{B.18}$$

$$\frac{\partial^2 \hat{B}}{\partial s^2} = G(z)[2D_s F(s) + sD_s^2 F(s)], \tag{B.19}$$

$$\frac{\partial^2 \hat{B}}{\partial s \partial z} = F(s)\, D_z G(z) + sD_s F(s)\, D_z G(z), \tag{B.20}$$

$$\frac{\partial^2 \hat{B}}{\partial z^2} = sF(s)\, D_z^2 G(z). \tag{B.21}$$

where D_s and D_z represent $\mathrm{d}/\mathrm{d}s$ and $\mathrm{d}/\mathrm{d}z$, respectively. The momentum equations (B.15) and (B.16) can then be written in the following forms

$$\begin{aligned}\frac{\partial v_z}{\partial z} = {} & \mathcal{L}_1(s)G(z)b_s + \mathcal{L}_2(s)D_z G(z)b_z \\ & + \mathcal{L}_3(s)G(z)\frac{\partial b_z}{\partial z} + \mathcal{L}_4(s)G(z)\frac{\partial b_s}{\partial s} + \mathcal{L}_5(s)D_z G(z)\frac{\partial b_z}{\partial s} \\ & + (-\mathcal{L}_5)(s)G(z)\frac{\partial^2 b_s}{\partial s^2} + (-\mathcal{L}_5)(s)G(z)\frac{\partial^2 b_z}{\partial s \partial z}\end{aligned} \tag{B.22}$$

where, for simplicities sake, we have written

$$\begin{aligned}\mathcal{L}_1(s) &\equiv -\frac{1}{s}[s^2 D_s^2 F(s) + 3sD_s F(s) + (m^2 - 1)F(s)], \\ \mathcal{L}_2(s) &\equiv -[2F(s) + sD_s F(s)], \\ \mathcal{L}_3(s) &\equiv 4F(s) + sD_s F(s), \\ \mathcal{L}_4(s) &\equiv 3F(s), \quad \mathcal{L}_5(s) \equiv -sF(s).\end{aligned}$$

The 2nd (diagnostic) momentum equation is

$$\begin{aligned}\frac{\partial v_s}{\partial z} = {} & \mathcal{L}_6(s)D_z G(z)b_s + \mathcal{L}_7(s)[m^2 G(z) + s^2 D_z^2 G(z)]b_z \\ & + \mathcal{L}_5 D_z G(z)\frac{\partial b_s}{\partial s} + \mathcal{L}_6 G(s)\frac{\partial b_s}{\partial z} \\ & + \mathcal{L}_5 G(z)\frac{\partial^2 b_s}{\partial s \partial z} + \mathcal{L}_5 G(z)\frac{\partial^2 b_z}{\partial z^2}.\end{aligned} \tag{B.23}$$

where

$$\mathcal{L}_6(s) \equiv D_s[sF(s)], \quad \mathcal{L}_7(s) \equiv F(s)/s.$$

The basic state field and basic state flow (or geostrophic flow) appear once each in both the induction equations. In the first term on the right hand side of (B.15) and (B.16), these terms become, respectively

$$imF(s)G(z)v_s \quad \text{and} \quad imF(s)G(z)v_z. \tag{B.24}$$

Similarly, also, where the basic state flow $\mathbf{V}_0$ is concerned:

$$-imF^{\Omega}(s)G^{\Omega}(z)b_s \quad \text{and} \quad -imF^{\Omega}(s)G^{\Omega}(z)b_z. \tag{B.25}$$

In order to obtain the governing equations in a computationally tractable form, it was necessary to compute some useful integrals.

$$\int_{-\zeta}^{\zeta} \cos\frac{n\pi}{2\zeta}(z+\zeta)\cos\frac{m\pi}{2\zeta}(z+\zeta)\,\mathrm{d}z = \begin{cases} 2\zeta & \text{if } m=n=0 \\ \zeta\delta_{mn} & \text{if } m,n>0 \end{cases} \tag{B.26}$$

$$\int_{-\zeta}^{\zeta} \sin\frac{n\pi}{2\zeta}(z+\zeta)\sin\frac{m\pi}{2\zeta}(z+\zeta)\,\mathrm{d}z = \begin{cases} 0 & \text{if } m=n=0 \\ \zeta\delta_{mn} & \text{if } m,n>0 \end{cases} \tag{B.27}$$

Also, define the integral quantities A_{mn}, C_{mn}, E_{mn}, H_{mn} and K_{mn} by

$$\begin{aligned}
A_{mn} &= \int_{-\zeta}^{\zeta} G(z)\cos\bar{m}(z+\zeta)\cos\bar{n}(z+\zeta)\mathrm{d}z, \\
C_{mn} &= \int_{-\zeta}^{\zeta} D_z G(z)\cos\bar{m}(z+\zeta)\sin\bar{n}(z+\zeta)\mathrm{d}z, \\
E_{mn} &= \int_{-\zeta}^{\zeta} D_z G(z)\sin\bar{m}(z+\zeta)\cos\bar{n}(z+\zeta)\mathrm{d}z, \\
H_{mn} &= \int_{-\zeta}^{\zeta} G(z)\sin\bar{m}(z+\zeta)\sin\bar{n}(z+\zeta)\mathrm{d}z, \\
K_{mn} &= \int_{-\zeta}^{\zeta} D_z^2 G(z)\sin\bar{m}(z+\zeta)\sin\bar{n}(z+\zeta)\mathrm{d}z, \\
A^{\Omega}_{mn} &= \int_{-\zeta}^{\zeta} G^{\Omega}(z)\cos\bar{m}(z+\zeta)\cos\bar{n}(z+\zeta)\mathrm{d}z, \\
H^{\Omega}_{mn} &= \int_{-\zeta}^{\zeta} G^{\Omega}(z)\sin\bar{m}(z+\zeta)\sin\bar{n}(z+\zeta)\mathrm{d}z.
\end{aligned}$$

for $0 \le n_0 \le m, n \le NZ$.

We obtain the final form for the perturbation equations (prior to their fourth order finite difference discretization) by multiplying (B.22) and (B.15) by $\cos\bar{r}(z+\zeta)$ and then integrating between $z=-\zeta$ and ζ. Similarly, (B.23) and (B.16) are multiplied by $\sin\bar{r}(z+\zeta)$ and integrated in z.

For (B.22):

$$\begin{aligned}
\zeta\bar{r}u_{z,r}(s,t) = \sum_{n=n_0}^{NZ} &\left[\mathcal{L}_1 b_{s,n} + \mathcal{L}_3(\bar{n}b_{z,n}) + \mathcal{L}_4 D_s b_{s,n}\right. \\
&\left. +(-\mathcal{L}_5)D_s^2 b_{s,n} + (-\mathcal{L}_5)(\bar{n}D_s b_{z,n})\right] A_{rn} \\
&+\left[\mathcal{L}_2 b_{z,n} + \mathcal{L}_5 D_z b_{z,n}\right] C_{rn}
\end{aligned} \tag{B.28}$$

The 2nd (diagnostic) momentum equation (B.23) becomes:

$$-\zeta\bar{r}u_{s,r}(s,t) = \sum_{n=n_0}^{NZ} (\mathcal{L}_6 b_{s,n} + \mathcal{L}_5 D_s b_{s,n}) E_{rn}$$

$$
\begin{aligned}
&+[\mathcal{L}_7 m^2 b_{z,n} - \mathcal{L}_6 \bar{n} b_{s,n} \\
&\quad -\mathcal{L}_5 \bar{n} D_s b_{s,n} - \mathcal{L}_5)\bar{n}^2 b_{z,n}]H_{rn} \\
&\quad -\mathcal{L}_5 b_{z,n} K_{rn}
\end{aligned}
\tag{B.29}
$$

The induction equations are quickly obtained. For (B.15):

$$
\begin{aligned}
\frac{\partial b_{s,r}}{\partial t}(s,t) &= \frac{im}{\zeta} \sum_{n=n_0}^{NZ} (F u_{s,n} A_{rn} - F^{\Omega} b_{s,n} A^{\Omega}_{rn}) \\
&\quad + \frac{1}{\Lambda} \left[\frac{3}{s} D_s b_{s,r} + D_s^2 b_{s,r} \right. \\
&\quad \left. + \left(\frac{1}{s^2}(1-m^2) - \bar{r}^2 \right) b_{s,r} + \frac{2\bar{r}}{s} b_{z,r} \right]
\end{aligned}
\tag{B.30}
$$

For (B.16):

$$
\begin{aligned}
\frac{\partial b_{z,r}}{\partial t}(s,t) &= \frac{im}{\zeta} \sum_{n=n_0}^{NZ} (F u_{z,n} H_{rn} - F^{\Omega} b_{z,n} H^{\Omega}_{rn}) \\
&\quad + \frac{1}{\Lambda} \left[\frac{1}{s} D_s b_{z,r} + D_s^2 b_{z,r} \right. \\
&\quad \left. - \frac{m^2}{s^2} b_{z,r} - \bar{r}^2 b_{z,r} \right].
\end{aligned}
\tag{B.31}
$$

Appendix C

Determination of V_G for the Interaction of Several Axial Modes

Given the form for the geostrophic flow as in Chapter 1, eq. (1.17)

$$V_G = \frac{(2E)^{-1/2}}{2\pi s} \int_{C(s)} [(\nabla \times \mathbf{B}) \times \mathbf{B}]_\phi \, \mathrm{d}S$$

we derive the component form for the geostrophic flow (4.19) that is used in the nonlinear time-stepping code in Chapter 4 [with the form (3.25) of Chapter 3 as a special case]. Let us make the decompositions for the perturbed magnetic field $\tilde{\mathbf{b}} = E^{1/4}\mathbf{b} = E^{1/4}(b_s, b_\phi, b_z)$

$$\mathbf{B} = \mathbf{B}_0 + \tilde{\mathbf{b}} = B_0(s,z)\mathbf{1}_\phi + E^{1/4}\mathbf{b}$$

where E is the Ekman number defined in the Chapter 1, equation (1.9). Since the azimuthal basic state $\mathbf{B}_0$ makes no contribution to V_G we may write

$$V_G = 2^{-1/2} \int_{-\zeta}^{\zeta} \langle (\nabla \times \mathbf{b}) \times \mathbf{b} \rangle_\phi \, \mathrm{d}z \, .$$

The azimuthal average of a vector function $\mathbf{f} = \mathbf{f}(s, \phi, z, t)$ is defined as

$$\langle \, \mathbf{f} \, \rangle \equiv (2\pi)^{-1} \int_0^{2\pi} \mathbf{f} \, \mathrm{d}\phi \, .$$

As in (4.12) and (4.13), let the components of $\mathbf{b}$ have expansions

$$\begin{aligned}
b_s(s,\phi,z,t) &= 2\sum_{n=0}^{NZ} [b_{s,n}(s,t)e^{im\phi} + b^*_{s,n}(s,t)e^{-im\phi}] \cos \bar{n}(z+\zeta) \\
b_\phi(s,\phi,z,t) &= 2\sum_{n=0}^{NZ} [b_{\phi,n}(s,t)e^{im\phi} + b^*_{\phi,n}(s,t)e^{-im\phi}] \cos \bar{n}(z+\zeta) \\
b_z(s,\phi,z,t) &= 2\sum_{n=1}^{NZ} [b_{z,n}(s,t)e^{im\phi} + b^*_{z,n}(s,t)e^{-im\phi}] \sin \bar{n}(z+\zeta)
\end{aligned}$$

where the superscript $*$ represents the complex conjugate, m is the azimuthal wave number, ζ is the annular half-height, $\bar{n} = n\pi/2\zeta$ and NZ is the axial mode truncation.

Observe that

$$\langle(\nabla \times \mathbf{b}) \times \mathbf{b}\rangle_\phi = \left\langle \frac{b_s b_\phi}{s} \right\rangle + \left\langle b_s \frac{\partial b_\phi}{\partial s} \right\rangle - \left\langle \frac{b_s}{s}\frac{\partial b_s}{\partial \phi} \right\rangle - \left\langle \frac{b_z}{s}\frac{\partial b_z}{\partial \phi} \right\rangle + \left\langle b_z \frac{\partial b_\phi}{\partial z} \right\rangle .$$

Consider

$$\begin{aligned} b_s b_\phi &= \sum_{r,n=0}^{NZ} (b_{s,r} b_{\phi,n} e^{2im\phi} + b_{s,r} b^*_{\phi,n} + b^*_{s,r} b_{\phi,n} + b^*_{s,r} b^*_{\phi,n} e^{-2im\phi}) \\ &\qquad \times \cos \bar{r}(z+\zeta) \cos \bar{n}(z+\zeta). \end{aligned}$$

Averaging over ϕ then gives

$$\langle b_s b_\phi \rangle = \sum_{r,n=0}^{NZ} (b_{s,r} b^*_{\phi,n} + b^*_{s,r} b_{\phi,n}) \cos \bar{r}(z+\zeta) \cos \bar{n}(z+\zeta).$$

For the term $b_s \partial_s b_\phi$ we have

$$\begin{aligned} b_s \frac{\partial b_\phi}{\partial s} &= \sum_{r,n=0}^{NZ} (b_{s,r} D b_{\phi,n} e^{2im\phi} + b_{s,r} D b^*_{\phi,n} + b^*_{s,r} D b_{\phi,n} + b^*_{s,r} d b^*_{\phi,n} e^{-2im\phi}) \\ &\qquad \times \cos \bar{r}(z+\zeta) \cos \bar{n}(z+\zeta) \end{aligned}$$

On taking the azimuthal average

$$\left\langle b_s \frac{\partial b_\phi}{\partial s} \right\rangle = \sum_{r,n=0}^{NZ} (b_{s,r} D b^*_{\phi,n} + b^*_{s,r} D b_{\phi,n}) \cos \bar{r}(z+\zeta) \cos \bar{n}(z+\zeta)$$

For the term $b_z \partial_z b_\phi$ we have:

$$\begin{aligned} b_z \frac{\partial b_\phi}{\partial z} &= -\sum_{r,n=0}^{NZ} \bar{n}(b_{z,r} b_{\phi,n} e^{2im\phi} + b_{z,r} b^*_{\phi,n} + b^*_{z,r} b_{\phi,n} + b^*_{z,r} b^*_{\phi,n} e^{-2im\phi}) \\ &\qquad \times \sin \bar{r}(z+\zeta) \sin \bar{n}(z+\zeta) \end{aligned}$$

in which case

$$\left\langle b_z \frac{\partial b_\phi}{\partial z} \right\rangle = -\sum_{r,n=0}^{NZ} \bar{n}(b_{z,r} b^*_{\phi,n} + b^*_{z,r} b_{\phi,n}) \sin \bar{r}(z+\zeta) \sin \bar{n}(z+\zeta)$$

For the terms $b_s \partial_\phi b_s$ and $b_z \partial_\phi b_z$ we have

$$b_s \frac{\partial b_s}{\partial \phi} = \frac{1}{2}\frac{\partial}{\partial \phi}\left(b_s^2\right), \quad b_z \frac{\partial b_z}{\partial \phi} = \frac{1}{2}\frac{\partial}{\partial \phi}\left(b_z^2\right),$$

and in both cases the azimuthal average yields:

$$\left\langle b_s \frac{\partial b_s}{\partial \phi} \right\rangle = \left\langle b_z \frac{\partial b_z}{\partial \phi} \right\rangle = 0.$$

Thus, the geostrophic flow V_G takes the form

$$\begin{aligned}
V_G(s) &= 2^{-1/2} \int_{-\zeta}^{\zeta} \langle (\nabla \times \mathbf{b}) \times \mathbf{b} \rangle_\phi \, \mathrm{d}z \\
&= 2^{-1/2} \int_{-\zeta}^{\zeta} \left\langle \frac{b_s b_\phi}{s} \right\rangle + \left\langle b_s \frac{\partial b_\phi}{\partial s} \right\rangle + \left\langle b_z \frac{\partial b_\phi}{\partial z} \right\rangle \mathrm{d}z \\
&= \frac{2^{-1/2}}{s} \sum_{n=0}^{NZ} \alpha_n [b_{s,n} b^*_{\phi,n} + b^*_{s,n} b_{\phi,n}] \\
&\quad + 2^{-1/2} \sum_{n=0}^{NZ} \alpha_n [b_{s,n} D b^*_{\phi,n} + b^*_{s,n} D b_{\phi,n}] \\
&\quad - 2^{-1/2} \sum_{n=1}^{NZ} \alpha_n \bar{n} [b_{z,n} b^*_{\phi,n} + b^*_{z,n} b_{\phi,n}] \\
&= 2^{1/2} \Re \sum_{n=0}^{NZ} \alpha_n \left[\frac{b_{s,n}}{s} + b_{s,n} D - \bar{n} b_{z,n} \right] b^*_{\phi,n}.
\end{aligned}$$

where

$$\alpha_n = \begin{cases} 2\zeta & \text{if } n = 0 \\ \zeta & \text{if } n > 0 \end{cases}.$$

For the simpler case in Chapter 3 involving only one axial mode, the above expression for V_G should be modified by removing the summation symbol. The dummy variable $\bar{n}$ must now be prescribed and represents the axial wavenumber (scaled by $\pi/2\zeta$).

Appendix D

The Induced Mean Poloidal Field

Cowling's theorem (1934) shows that a purely axisymmetric flow cannot sustain a purely axisymmetric field. This means that the full geodynamo problem is necessarily three dimensional. Let us decompose the magnetic and flow fields into their respective axisymmetric and non-axisymmetric parts

$$\mathbf{B}(s,\phi,z,t) = \bar{\mathbf{B}}(s,z,t) + \tilde{\mathbf{b}}(s,\phi,z,t) \tag{D.1}$$

$$\mathbf{V}(s,\phi,z,t) = \bar{\mathbf{V}}(s,z,t) + \tilde{\mathbf{v}}(s,\phi,z,t) \tag{D.2}$$

$$\text{with } \langle\tilde{\mathbf{b}}\rangle = \langle\tilde{\mathbf{v}}\rangle = 0 \tag{D.3}$$

and where $\langle\cdot\rangle$ is the azimuthal average defined in Appendix C. The hydrodynamic dynamo equations (1.2, 1.3, 1.4, 1.5) can then be separated into a coupled set of axisymmetric and non-axisymmetric equations [see Fearn (1994)]. In the linear regime, it is possible to consider each part in isolation if one prescribes an appropriate electromotive force (axisymmetric equations) or mean basic state $\bar{\mathbf{B}}$, $\bar{\mathbf{V}}$ (non-axisymmetric equations).

We consider the evolution of non-axisymmetric instabilities $\tilde{\mathbf{b}}$ and $\tilde{\mathbf{v}}$ under a mean basic field in the Ekman regime [i.e. $\tilde{\mathbf{b}}$, $\tilde{\mathbf{v}} = \mathrm{O}(E^{1/4})$, see Chapter 1]. The imposed mean basic state is

$$B_0(s,z)\mathbf{1}_\phi = sF(s)G(z)\mathbf{1}_\phi. \tag{D.4}$$

Taking $B_0 = \mathrm{O}(1)$ will, in general, result in a mean poloidal field $\mathbf{B}_M$ of $\mathrm{O}(E^{1/2})$ through the action of the ϕ-component of the electromotive force. The mean part

of the magnetic field is then

$$\bar{\mathbf{B}} = B_0(s,z)\mathbf{1}_\phi + \mathbf{B}_M = B_0(s,z)\mathbf{1}_\phi + \nabla\times(A\mathbf{1}_\phi) \tag{D.5}$$

where we have written the induced poloidal field $\mathbf{B}_M$ in terms of the poloidal scalar A. The evolution of A is described by

$$\frac{\partial A}{\partial t} + \left(\frac{1}{s^2} - \nabla^2\right) A = \langle \tilde{\mathbf{v}}\times\tilde{\mathbf{b}}\rangle_\phi \tag{D.6}$$

[see Fearn (1994)]. Consequently $A = \mathrm{O}(E^{1/2})$ and may be neglected in the linear problem. Whilst A is $\mathrm{O}(E^{1/4})$ smaller than the amplitude of the instabilities $[|\tilde{\mathbf{b}}|, |\tilde{\mathbf{v}}| = \mathrm{O}(E^{1/4})]$, the induced poloidal field cannot, in general, be neglected in calculating the geostrophic flow.

$$\begin{aligned} V_G &= (2E)^{-1/2}\int_{-\zeta}^{\zeta}\langle(\nabla\times\mathbf{B})\times\mathbf{B}\rangle_\phi\,\mathrm{d}z \\ &= (2E)^{-1/2}\left\{\int_{-\zeta}^{\zeta}\left[(\nabla\times\bar{\mathbf{B}})\times\bar{\mathbf{B}}\right]_\phi\,\mathrm{d}z + \int_{-\zeta}^{\zeta}\langle(\nabla\times\tilde{\mathbf{b}})\times\tilde{\mathbf{b}}\rangle_\phi\,\mathrm{d}z\right\} \end{aligned} \tag{D.7}$$

In our instability calculations we sought instabilities $\tilde{\mathbf{b}}$ and $\tilde{\mathbf{v}}$ in the Ekman regime. This means that the second term on the right side of (D.7) contributes at $\mathrm{O}(1)$ to the geostrophic flow. Fearn (1994) has shown that the integrand in the first term on the right side of (D.7) may be written as

$$\left[(\nabla\times\bar{\mathbf{B}})\times\bar{\mathbf{B}}\right]_\phi = -\frac{\partial A}{\partial z}\frac{1}{s}\frac{\partial}{\partial s}(sB_0) - \frac{\partial B_0}{\partial z}\frac{1}{s}\frac{\partial}{\partial s}(sA)\,. \tag{D.8}$$

upon using (D.5). Since $A = \mathrm{O}(E^{1/2})$ then the mean poloidal field must also, in general, make an $\mathrm{O}(1)$ contribution to V_G.

Firstly, observe that if B_0 is z-independent as in Chapter 3, then

$$\int_{-\zeta}^{\zeta}\frac{\partial A}{\partial z}\frac{1}{s}\frac{\partial}{\partial s}(sB_0) + \frac{\partial B_0}{\partial z}\frac{1}{s}\frac{\partial}{\partial s}(sA)\,\mathrm{d}z = \left[\frac{A}{s}\frac{\partial}{\partial s}(sB_0)\right]_{-\zeta}^{\zeta} = 0$$

upon applying the boundary conditions $A = 0$ on $z = \pm\zeta$. This result is independent of the form for F. However, if B_0 is also z-dependent then the calculation is more involved depending on the specific choice of $G(z)$.

Firstly, we must find the form of the expansion for A. From (D.6)

$$\begin{aligned} \left(\frac{\partial}{\partial t} + \frac{1}{s^2} - \nabla^2\right) A &= \langle\tilde{\mathbf{v}}\times\tilde{\mathbf{b}}\rangle_\phi \\ &= \langle\tilde{v}_z\tilde{b}_s\rangle - \langle\tilde{v}_s\tilde{b}_z\rangle \\ &= \sum_{r,n=0}^{\infty} f_{rn}(s)\sin\bar{r}(z+\zeta)\cos\bar{n}(z+\zeta) \end{aligned}$$

where $f_{rn}(s) = \tilde{v}_{z,r}\tilde{b}^*_{s,n} + \tilde{v}^*_{z,r}\tilde{b}_{s,n} - \tilde{v}_{s,n}\tilde{b}^*_{z,r} - \tilde{v}^*_{s,n}\tilde{b}_{z,r}$. Thus

$$\left(\frac{\partial}{\partial t} + \frac{1}{s^2} - \frac{\partial^2}{\partial s^2} - \frac{1}{s}\frac{\partial}{\partial s} - \frac{\partial^2}{\partial z^2}\right) A$$
$$= \frac{1}{2}\sum_{r,n=0}^{\infty} f_{rn}(s)\Big[\sin(\bar{r}+\bar{n})(z+\zeta) + \sin(\bar{r}-\bar{n})(z+\zeta)\Big]. \qquad \text{(D.9)}$$

Seeking solutions of the form

$$A = \sum_{k=1}^{\infty} A_k \sin\bar{k}(z+\zeta) \qquad \text{(D.10)}$$

satisfies the boundary conditions on the poloidal field and leads to a consistent determination of A through solving

$$\left(\frac{\partial}{\partial t} + \frac{1}{s^2} - \frac{\partial^2}{\partial s^2} - \frac{1}{s}\frac{\partial}{\partial s} + \bar{k}^2\right) A_k$$
$$= \frac{1}{2}\sum_{r,n=0}^{\infty} f_{rn}\{\delta_{k-n,r} + \gamma_{k,n,r}\} \qquad \text{(D.11)}$$

for all $k \geq 1$ and where $\delta_{k-n,r}$ is the Kronecker delta symbol and

$$\gamma_{k,n,r} = \begin{cases} 1 & \text{if } \bar{r} \neq \bar{n} - \bar{k} \text{ and } \bar{r} \neq \bar{n} + \bar{k} \\ -1 & \text{if } \bar{r} = \bar{n} - \bar{k} \text{ and } \bar{r} \neq \bar{n} + \bar{k} \\ 0 & \text{if } \bar{r} \neq \bar{n} - \bar{k} \text{ and } \bar{r} = \bar{n} + \bar{k} \end{cases}$$

The contribution to $(2E)^{1/2}V_G$ induced from the mean poloidal field is of the form

$$\int_{-\zeta}^{\zeta}\left[(\nabla\times\bar{\mathbf{B}})\times\bar{\mathbf{B}}\right]_{\phi} \mathrm{d}z = -\int_{-\zeta}^{\zeta}\frac{\partial A}{\partial z}\frac{1}{s}\frac{\partial}{\partial s}(sB_0) + \frac{\partial B_0}{\partial z}\frac{1}{s}\frac{\partial}{\partial s}(sA)\,\mathrm{d}z$$
$$= \left[\frac{A}{s}\frac{\partial}{\partial s}(s^2FG)\right]_{-\zeta}^{\zeta} + \int_{-\zeta}^{\zeta}\frac{A}{s}\frac{\partial}{\partial s}(s^2F)G' - FG'\frac{\partial}{\partial s}(sA)\,\mathrm{d}z$$

and let us take $G(z) = \cos\bar{l}(z+\zeta)$ (where, respectively, $\bar{l} = \pi/2\zeta$ or π/ζ corresponds to the dipolar or quadrupolar basic states of Chapter 4) and write $A = A_k(s)\sin\bar{k}(z+\zeta)$. Then, continuing from (D.12) we have

$$-\bar{l}\int_{-\zeta}^{\zeta}\left[\frac{A_k}{s}\frac{\partial}{\partial s}(s^2F) - F\frac{\partial}{\partial s}(sA_k)\right]\sin\bar{k}(z+\zeta)\sin\bar{l}(z+\zeta)\,\mathrm{d}z$$
$$= \bar{l}\left[\frac{A_k}{s}\frac{\partial}{\partial s}(s^2F) - F\frac{\partial}{\partial s}(sA_k)\right]\int_{-\zeta}^{\zeta}\Big[\cos(\bar{k}+\bar{l})(z+\zeta) - \cos(\bar{k}-\bar{l})(z+\zeta)\Big]\,\mathrm{d}z. \qquad \text{(D.12)}$$

Provided $\bar{k} \neq \bar{l}$ then (D.12) will vanish. When $\bar{l} = \pi/2\zeta$ (which represents the dipolar basic state example) then the solution parity for a dipole(quadrupole) require that

the odd(even) modes be selected for $\tilde{\mathbf{b}}$ and the even(odd) modes be selected for $\tilde{\mathbf{v}}$ in the solution expansions (4.12) and (4.13). Therefore, when $\bar{k} = \bar{l}$ (D.12) becomes

$$-\pi l \left[\frac{A_l}{s} \frac{\partial}{\partial s}(s^2 F) - F \frac{\partial}{\partial s}(s A_l) \right] \tag{D.13}$$

where $l = 1$. The case for the quadrupole basic field runs parallel to the above and the contribution to the geostrophic flow is obtained in that case by replacing l by 2.

In the spirit of enforcing a differential rotation with the geostrophic structure computed from the linear eigenfunction at $\Lambda = \Lambda_c$ [see Chapter 3, eq. (3.32)] we sketch how the contribution from the mean field may also be included as in the differential rotation.

The steady state version of equation (D.11)

$$\left(\frac{1}{s^2} - \frac{\partial^2}{\partial s^2} - \frac{1}{s}\frac{\partial}{\partial s} + \bar{k}^2 \right) A_k = \frac{1}{2} \sum_{r,n=0}^{\infty} f_{rn} \{ \delta_{k-n,r} + \gamma_{k,n,r} \} \tag{D.14}$$

is then solved with the linear eigenfunctions $\tilde{\mathbf{b}}$ and $\tilde{\mathbf{v}}$ substituted into f_{rn}. In our calculation, this just requires us to solve (D.14) for the values $k = 1$ in the case of the dipolar field and $k = 2$ in the case of the quadrupolar field. Once the A_k has been obtained it can be substituted into (D.13) to obtain the mean poloidal field contribution to V_G. This would then be added to the non-axisymmetric contribution to the geostrophic flow and the sum would be scaled by the magnetic Reynolds' number ready to be input as a differential rotation.